Reusable Upper Stage

Stability and Control during Reentry and Descent

F. Bentla

Delft University of Technology

Delft University of Technology

Challenge the future

Reusable Upper Stage

Stability and Control during Reentry and Descent

by

F. Bentla

to obtain the degree of Master of Science
at the Delft University of Technology,

Thesis supervisor: Dr. Ir. E. Mooij

Cover art background courtesy of NASA, made during STS-107 showing the Atlantic Ocean. Available at http://earthobservatory.nasa.gov/IOTD/view.php?id=80340
Upper stage modeled and rendered with Blender. Reentry effects added with Gimp.

TU Delft

Acknowledgments

I would like to begin my acknowledgments with my supervisor Dr. Erwin Mooij for giving me so many ideas on how to improve my work, and patiently following my progress with interest.

Many thanks also go to my wife who kindly accepted my obsession with spaceflight and patiently listened to me ramble on about exciting findings and challenges I encountered during this project.

And last but certainly not least I am incredibly grateful for my parents for never wavering in their utmost support throughout my entire life, despite never really understanding why their son is more interested in spaceships than learning something sensible like physician or lawyer. I would not have the same opportunities without them.

Preface

Ever since I was a child I wanted to travel to space, explore other planets, and discover strange new places. Variations of this sentence are very common in many introductions to science fiction books, application letters for space related jobs, prefaces of master thesis reports, and many other places.

This desire expressed by so many people around the world shows that I am not the only one. The infinite expanse of space with all its wonders easily captures peoples imagination and inspires us to dream about humanities future among the stars.

So the question for me was and still is how do I get to travel to space? Becoming an Astronaut of course is the obvious answer but when faced with reality one quickly realizes how low the chances of becoming an astronaut really are. Worldwide only 12 people launched to the International Space Station in 2015 and many of them are veteran astronauts. Given the total human population of the Earth that is an insignificant amount and these astronauts are just going into a low Earth orbit, not even close to any planet or even the Moon.

I eventually realized that if I ever want to go to space all others who dream about it as well must be able to go. I say this not because of empathy but because it is literally the only realistic way. My chance to go to space increases when the chance for the rest of humanity does.

So what is it that keeps everyone on Earth? It is not their health, not a lack of motivation, not some physical barrier preventing spaceflight, and no man-made laws. It is simply the cost of access to space. Tickets are being sold but nobody can afford them except for the extremely wealthy.

What is cost and why is going into space so expansive? Costs are often associated with money or resources but with costs we ultimately measure labor time, a portion of a humans live. Most of the useful things that cost something does so because people have spend time making it, even resources, which have to be extracted from the ground through labor. To buy resources or a product one also has to spend roughly the same amount of labor time.

The same is true for a launch into space. Currently a lot of labor hours have to be spend to enable it by producing the resources and parts, assemble them into sub-component, put the sub-component together to make a rocket and finally inspect, test, and operate the launcher. The labor hours spend per launch is huge and all of it is shot into space once. Then all those labor hours have to be spend again for the next launch.

To buy a ticket to space requires a person to spend about the same amount of labor hours as it took to build the launch vehicle, which is currently on the order of several lifetimes.

So the goal is to reduce labor hours per launch to much less then a lifetime, but how? Maybe by reducing the labor hours to produce a rocket. This sounds promising at first. However, there is a minimum on how much labor you need to extract resources and build a rocket. Since capitalism in general strives for minimum labor hours (aka costs) chances are there is not much room for improvements in many industries. There may be some inefficiencies in the space industry due to uneconomic rocket acquisition practices of space agencies but improvements there are also limited.

Assuming that the cost for building a rocket can no longer be further reduced, a more promising and much more exciting solution is to get more launches out of one rocket. The benefit is not just in the reuse. Labor hours spend on improving the efficiency of an expandable rocket can usually only improve it by a fraction of what it can already do, say instead of one unit of payload a rocket can now put one and a half units of payload into orbit if it is improved by impressive 50%.

However, labor spend on introducing reusability instantly at least doubles the performance of that launcher, which can now launch twice or more. Now working towards improvements, especially in terms of reliability and durability, could instantly add 2 or 3 more launches to the life of the rocket for the same effort. Later when a rocket routinely flies hundreds of times a small amount of labor put into improving a certain part or assembly, for example, could add one additional launch to the vehicles life and all others of the same type, which would have taken a huge amount of labor to accomplish previously with expandable rockets.

Now if the cost for the launch is shared between multiple spacefarers on the same flight the cost per launch for a single person could be just a few labor hours, an amount everyone can afford to work and spend on a trip to space.

Of course in reality it is not that easy and adding reusability could reduce a rocket's performance. A loss, which must be recaptured over the course of multiple launches. Also just maintaining and operating an available rocket is not labor free. The ground handling must also be efficiently designed in terms of required labor for the launch system to be practical. In general a reusable launcher must at first be at least more economical than expandable launcher to establish themselves successfully.

But the general idea I just outlined shows how much potential there is in reusing a launch vehicle. In fact this idea is not new and is used on all kind of transportation systems today already.

So the plan is simple, spend labor hours on making launch vehicle reusability possible. Once that is achieved it should get progressively easier to add more launches to the life of a launch vehicle with improvements until they too last for decades and hundreds of flights, just like airplanes, trains, and ships.

Then simply buy a ticket and launch to space.

F. Bentla
Trier, November 2016

Contents

List of Symbols

Variables

Symbol	Unit	Description
α	rad	Angle of attack
β	rad	Side-slip angle
γ	rad	Flight-path angle
γ	–	Heat capacity ratio
δ	rad	Latitude angle
θ	rad	Pitch angle
μ	$\mathrm{m^3/s^2}$	Gravitational parameter of the Earth
ρ	$\mathrm{kg/m^3}$	Local atmospheric density
σ	rad	Bank angle
τ	rad	Longitude angle
ϕ	rad	Roll angle
χ	rad	Heading angle
ψ	rad	Yaw angle
ω	rad/s	Angular rate
$\mathbf{a}$	$\mathrm{m/s^2}$	Acceleration vector
C	–	Aerodynamic coefficient
D	N	Drag force
$\mathbf{e}$	–	Euler axis
F	N	Force magnitude
$\mathbf{F}$	N	Force vector
g	$\mathrm{m/s^2}$	Gravitational acceleration
G	$\mathrm{m^3kg^{-1}s^{-2}}$	Universal gravitational constant
h	m	Altitude
H	m	Geopotential altitude
I	Ns	Impulse
J_n	–	Spherical harmonic of n
$\mathbf{J}$	$\mathrm{kg/m^2}$	Inertia tensor
$\mathbf{K}$	–	Gain matrix
l	m	Length
L	N	Lift force
m	kg	Mass
M	–	Mach number
$\mathbf{M}$	Nm	Moment vector
p	rad/s	Roll rate
P	Pa	Local atmospheric pressure
P_n,P_m	–	Legendre polynomials
q	rad/s	Pitch rate
q	$\mathrm{W/m^2}$	Heat flux
$\bar{q}$	Pa	Dynamic pressure
$\mathbf{q}$	–	Attitude quaternion
Q	$\mathrm{J/m^2}$	Total heat
r	rad/s	Yaw rate
$\mathbf{r}$	m	Position vector relative to the center of the Earth
R	J/K	Gas constant of air
S	N	Side force
S	$\mathrm{m^2}$	Surface area

t	s	Elapsed time
T	K	Temperature
U	J/kg	Gravitational potential
V	m/s	Velocity
$\mathbf{V}$	m/s	Velocity vector
x	m	X-coordinate
y	m	Y-coordinate
z	m	Z-coordinate
Z	m	Geometric altitude

Subscripts

Symbol	Meaning
0	Initial condition/sea level
∞	Free stream condition
$aero$	Aerodynamics
$Apollo$	Related to the Apollo CM
aw	Wall adiabatic
cb	Central body
cm	Center of mass
cyl	Cylinder
D	Drag
e	Error
f	Final
$flap$	Aerodynamic surfaces/flap
$grav$	Gravitation
i	i-th element
j	j-th element
L	Lift
max	Maximum value
min	Minimum value
M	Pitch moment component
n	n-th element
N	Normal
N	Yaw moment component
$prop$	Propellant
P	Pressure
ref	Reference parameter/dimension
s	Stagnation point
sp	Specific
sph	Sphere
S	Side
$Stage$	Related to the reusable upper stage
$trans$	Transition
T	Target
w	Wall

Reference frames

Symbol	Meaning
A	Vehicle-carried aerodynamic frame
B	Vehicle-carried body fixed frame
I	Earth-centered inertial frame
R	Earth-centered Earth-fixed frame
T	Vehicle-carried trajectory frame
V	Vehicle-carried vertical frame

List of Abbreviations

Abbreviations	Meaning
AOCS	Attitude and Orbit Control System
AJ	Aerojet
CAD	Computer Aided Design
CEV	Crew Exploration Vehicle
CFD	Computational Fluid Dynamics
CM	Command Module
COM	Center of Mass
COP	Center of Pressure
COPV	Composite Overwrapped Pressure Vessel
CSM	Command and Service Module
DC	Delta Clipper
ESA	European Space Agency
ESC	Éstage Supérior Cryotechnique
FORTRAN	Formula Translator
GEO	Geostationary Earth Orbit
GTO	Geostationary Transfer Orbit
IMU	Inertial Measurement Unit
ISS	International Space Station
LEO	Low Earth Orbit
LQR	Linear Quadratic Regulator
NAOO	National Oceanic and Atmospheric Administration
NASA	National Aeronautics and Space Administration
ORBCOMM	Orbial Communication Corporation
OV	Orbital Vehicle
PDF	Probability Density Function
PICA	Phenolic-Impregnated Carbon Ablator
PID	Proportional-Integral-Derivative
RAAN	Right Ascension of the Ascending Node
RCS	Reaction Control System
RP	Rocket Propellant Refined Petroleum
SSTO	Single Stage To Orbit
STS	Space Transportation System
TT	Terrestrial Time
Tudat	TU Delft Astrodynamics Toolbox
TPS	Thermal Protection System
TU	Technische Universiteit
US	United States
VTOL	Vertical Takeoff and Landing

1

Introduction

Ever since mankind has conquered every corner of the Earth many pioneers claimed space as the new frontier. The exploration and exploitation of space offers the potential for virtually infinite resources and fundamental knowledge about the origin and ultimate fate of the universe. Furthermore, expansion and colonization of space ensures mankind's long-term survival in the cosmos by spreading the population out over many worlds and thereby reducing the risk for one cosmic catastrophe to instantly wipe out humanity.

Space transportation systems available today enable humans to reach out into the solar system with robotic spacecraft and even send a few men to Earth's natural satellite, the Moon. These efforts greatly expanded mankind's body of knowledge about the universe and produced inventions that improved the standard of living for everyone on Earth.

The high cost for access to space, however, severely limits the full utility of space travel (Hertzfeld et al., 2005). To extract rare-Earth materials from asteroids, for example, and return it to Earth takes little energy compared to sending payloads up Earth's gravity well. However, to do so efficiently requires sizable facilities and infrastructure launched from Earth as investment ahead of the extraction. The business case for such a venture would only close if the investment is sufficiently low to compete with mining on Earth. Hence to expand the reach of humanity into space requires cheap and frequent access to space.

The current methods used to launch payloads into space is to use expandable multistage rockets with the payload on top and propel the stack into orbit. The individual rocket stages are jettisoned after burnout and discarded (Ambrosius, 2009). This mode of operation is unusual compared to other transportation architectures, such as airplanes, trains, or automobiles, which relay on reusability over multiple missions to be cost effective.

While the argument can be made that the cost of rockets can be reduced by proper design, material selection, cost effective manufacturing, and payload maximization this approach is ultimately limited by the minimum amount of material and manpower to produce a vehicle (Morgan et al., 1989; Schnitt, 1998). Reusability can use the same principle and furthermore has the potential to drastically reduce the cost per mission by spreading the production costs out over many missions. It however comes with its own challenges, such as the need for an efficient ground handling to avoid excessive maintenance costs.

In recent years the idea of a fully reusable launch vehicle has seen renewed interest as methods to vertically land a rocket has been refined[1][2][3]. A two-stage vehicle has replaced single-stage-to-orbit concepts as the popular approach to a fully reusable launch vehicle bringing with it the benefits of a multistage rocket. In addition to the performance gain a multistage reusable rocket can be developed in modules, making one stage reusable first and then moving on to the next stage, which reduces financial and development risks by offering a working intermediate solution.

The development of a fully reusable first stage is currently pursued by companies such as SpaceX and Blue Origin with several successful landings already under their belts. The first stage is a logical

---

[1] `http://www.astronautix.com/d/dc-x.html`

[2] `http://www.theverge.com/2016/8/14/12467632/spacex-falcon-9-jcsat-16-drone-ship-landing-success`

[3] `http://www.theverge.com/2016/10/5/13173962/blue-origin-new-shepard-rocket-launch-escape-system-test`

choice as it does not only travel the slowest and lowest, but also represents the largest and therefore most expensive part of the rocket. After separation the first stage flies in a suborbital trajectory and is either redirected back to the launch site by its main engines or guided towards a sea platform for a propulsive landing (Bezos et al., 2014).

Recent progress made by SpaceX in their effort to make the fist stage reusable leaves the second stage as the next step in their path towards a fully reusable two-stage orbital rocket. In addition to the same flight environment as the first stage the second stage has to perform a reentry from orbit and descent through the atmosphere at hypersonic velocity. SpaceX has proposed a concept for a reusable second stage, which exhibits many similarities to their expandable upper stage currently in service with the notable addition of a heat shield at the top of the vehicle, a thrust cone shroud, and an extendable nozzle for the engine[4].

Reentries from orbit or even interplanetary trajectories have been performed numerous times typically with capsule shaped spacecraft designed for aerodynamic stability and control. The concept presented by SpaceX reenters with the payload interface side protected by a heat shield and facing into the incoming airflow. This has the advantage of leveraging the structural reinforcement already in place for the ascent, where the vehicle has to cope with stresses primarily along its longitudinal axis. The engines and other sensitive equipment installed in the thrust cone are protected in the wake of the vehicle. However, this configuration poses a critical question on which the feasibility of this reusable second stage concept depends.

”Is it possible to stabilize and control a conventionally-shaped reusable upper stage during reentry and descent?”

Answering this question requires a careful analysis of the static and dynamic stability of the vehicle as well as its controlability during reentry given the vehicle’s properties and the rapid changes in its environment during descent. Stability in terms of aerodynamics is here defined as the property of a body to deflect the incoming airflow such that the body is held at a certain attitude. The controlability of a vehicle can be quantified with the required control effort and efficiency to achieve a certain vehicle state. In terms relevant to a reentry vehicle this means the required propellant as well as variables such as settling time, overshoot, and overall effectiveness to reach a desired target using a realistic control authority. To determine these aspects a baseline vehicle and control system needs to be designed and simulated as it enters Earth’s atmosphere at hypersonic velocities.

The goal of this thesis is to present results, which help to answer the research question and assess the feasibility of controlled reentries from orbit of reusable cylindrical upper stages similar to the concept presented by SpaceX. This report first highlights the models and methods used to create and validate a simulator capable of predicting the motion of a reentry vehicle. Then a reusable upper stage model is used to study its aerodynamics and motion during reentry and descent.

Chapter 2 first gives an overview of relevant developments in the past and present in the field of reusable launch vehicles, upper stages, and reentry vehicles. The chapter concludes by presenting the reference vehicle used as baseline for the reentry simulation.

In Chapter 3 the theoretical background and mathematical models used to represent the baseline vehicle and its environment during reentry are discussed.

This is followed up by Chapter 4, which describes the methods used to achieve guidance and control for the vehicle in the simulation.

In Chapter 5 the numerical and computational aspects of the simulation are presented. The elements and architecture of the simulator itself are presented and illustrated using block diagrams. This chapter ends with presenting the verification of each element of the simulation and system tests of the reentry simulator and the guidance and control algorithm.

In Chapter 6 results from reentry simulations of the upper stage are presented starting with the aerodynamic stability of the vehicle. This is then followed by reentry simulations from a nominal LEO mission and a return from a geostationary transfer orbit. The output of the reentry simulations include general parameters describing the trajectory as well as flight loads, propellant consumption and a dispersion analysis.

Finally Chapter 7 summarizes the findings presented in Chapter 6 and relates them back to the

---

[4] `http://www.space.com/13140-spacex-private-reusable-rocket-elon-musk.html`

research question. On the basis of the obtained results an attempt at answering the research question is made. With the answers and the experience gained through this work recommendations are expressed as the final part of this report. These recommendations shall help any future work towards analyzing and realizing such a vehicle.

2

Mission Heritage

The idea of a rapidly reusable and consequently affordable launch vehicle is regarded as the holy grail of spaceflight. The prohibitively high cost of launching payload and passengers into space today can be almost entirely attributed to the cost for the construction and testing of a new launch vehicle, which is only used once. Up till now this is unique to orbital rockets in comparison to other modes of transportation, such as cars, naval ships, or airplanes. The rockets of today have therefore more in common with ammunition than a conventional transportation system.

The origin of today's launch vehicles are ballistic missiles intended for destruction of themselves and their target (Angelo, 2006). For this purpose maximizing the payload was the most important paradigm followed by making it as cheap to produce as possible. An idea for lowering access to space still discussed today by those who regards reusable launcher as impractical is to indeed treat launch vehicles like expendable ammunition. The intent is to reduce the number of parts to a minimum, by, for example, using a blow-down feed system instead of turbopumps, thereby reducing production and operation cost (Morgan et al., 1989; Schnitt, 1998). However, the achievable decrease in complexity and cost of the rocket is paid for by a decrease in efficiency, which can diminish the benefits of the total cost reduction. Nevertheless early studies showed competitive cost figures for such a concept compared to traditional state-of-the-art launch vehicle but development was discontinued[1].

A reusable launch vehicle, on the other hand, would be more expensive to produce, but the costs would be spread over several flights with the cost of each flight being only a fraction of the total vehicle price. This approach also comes with risks, namely the rigors of flying to space may prove too severe to allow for a practical or affordable reuse of the launch vehicle. The Space Shuttle is often cited as a famous example of how just the refurbishment costs have surpassed the cost of building and launching an expendable launch vehicle with similar payload capacity (Pielke, 2008).

Until recently the Space Shuttle has remained the only operational partly-reusable launch vehicle, but experimental vehicles, such as the DC-X, have demonstrated that the development and operation of a low-cost reusable rocket is nevertheless potentially possible if designed with efficient ground handling and sufficient durability in mind.

Currently, there are several partly reusable launch vehicle under development with the Falcon 9 being the first entering operation since the Space Shuttle. The return of its first stage is an important first step in opening space to a wider variety of users. But to truly achieve affordable access to space for the majority of a nations population a fully reusable launch vehicle is required. The cost of a Boeing 737-800, a common passenger aircraft, is comparable to the projected cost of the Falcon Heavy, which could launch a fully fueled Boeing 737 along with passenger and luggage into orbit[2] [3]. This demonstrates how much potential there is in fully reusable launch vehicle if the same kind of utility can be achieved as common in the airline industry.

In this chapter existing material on this topic is discussed, starting with Section 2.1, where efforts to develop reusable launch vehicle and their conclusions are briefly summarized. In Section 2.2 three existing expendable upper stages are discussed to understand their missions and characteristics. In

---

[1] `http://www.astronautix.com/s/seadragon.html`

[2] `http://www.boeing.com/company/about-bca/`

[3] `http://www.spacex.com/about/capabilities`

Section 2.3 a few examples of reentry vehicles are discussed and important aspects highlighted. In Section 2.4 two reusable upper stages are presented, which are both part of a reusable two-stage launch system. Based on the concept from SpaceX three reference vehicles are then presented in Section 2.5 with one configuration being an unaltered version of the Falcon 9 1.0 upper stage with a heat shield. The other two sport modifications, which are expected to improve the aerodynamic stability of the upper stage.

2.1. Reusable Launch Vehicle

Launch vehicles of today are descendants of ballistic missiles with the first one being the V-2 developed in Germany during the second World War. The technology was matured to become the carrier for nuclear bombs as a results of the arms race during the cold war between the Soviet Union and the United States. Maximizing the payload and assuring access to space was the prime objective, since the retrieval of the rocket after delivering the bomb to the enemy wasn't expected. To launch spacecraft both the Soviet Union and United States simply used these ballistic missiles and converted them to launch vehicles (Bullard, 1965; Chertok, 2005). But with the birth of dedicated orbital launch vehicle, civilian spaceflight, and the realities of limited budgets affordability was added as an prime objective for launch vehicle design. This objective became even more important with the entry of private launch service providers into the space transportation market.

Reusability has always been a possible solution to achieving that objective. Expendable launch vehicle have routinely demonstrated the capability to deliver payload to orbit. The missing capability required for achieving reusability for launch vehicle is the ability to return to the launch site in tact at the end of the mission. Several concepts are proposed to achieve this feet, which can be broadly categorized into two types, space planes and ballistic launch vehicle.

2.1.1. Spaceplanes

Given the operational advantages of having wings for the glide inside the atmosphere, namely steering towards a landing site, and performing a soft and precise landing on a runway, designing a launch vehicle as a rocket powered airplane instead of a missile is one of the earliest ideas towards reusability (Koelle et al., 2007). Conventional missiles are limited in ways to influencing their trajectory to a significant degree after their propellant is depleted and require final deceleration devices for a soft landing. Wings producing lift would enable the launcher to reenter the atmosphere and glide back to a runway for recovery without the need for propellant or parachutes.

One of the earliest winged spaceplane is the Silbervogel designed by Eugen Sänger to fly on a suborbital trajectory around the world non-stop (Koelle et al., 2007). It could do that with just an initial powered ascent followed by a number of skipping entries and a long glide. This design later evolved into the Sänger II two stage launch vehicle with both stages winged for an airplane-like return to the launch site. However, this concept was dropped due to the wings having a significant negative impact on the payload and a too low flight rate to justify the large development costs (Paschen, 1993).

The only realized partly-reusable launch vehicle capable of reaching orbit other than the Falcon 9 is the Space Shuttle. A vehicle consisting of a winged orbiter, an expendable external tank jettisoned after launch, and two reusable solid rocket boosters, which parachute into the Atlantic for recovery. Several designs have been initially proposed and tested for the Shuttle. Most notably the delta-winged Shuttle concept had to compete with lifting body vehicle designs. The benefits of having a lifting body is a reduction in structural mass as the body is used for both lift creation and as fuel tank (Jenkins et al., 2003). However, cross-range requirements from the US air force settled the choice in favor of the delta-wing configuration[4].

An interesting aspect of the Shuttle is the fact that its unconventional shape for a reentry vehicle made it aerodynamically unstable. It used a body flap hinged below the engines in the back for stabilization. This, however, requires a robust understanding of the vehicle's flight characteristics at every flight regime. This need was demonstrated by the first Space Shuttle mission STS-1. The aerodynamic pitch moment was higher than predicted by theoretical models and required a flap deflection within $5°$ of its maximum deflection to keep the vehicle at the desired angle of attack during reentry[5]. A sketch of the Orbiter is shown in Figure 2.1 with the body flap below its main engines.

---

[4] `http://history.nasa.gov/SP-4221/contents.htm`

[5] `http://www.jsc.nasa.gov/news/columbia/anomaly/STS1.pdf`

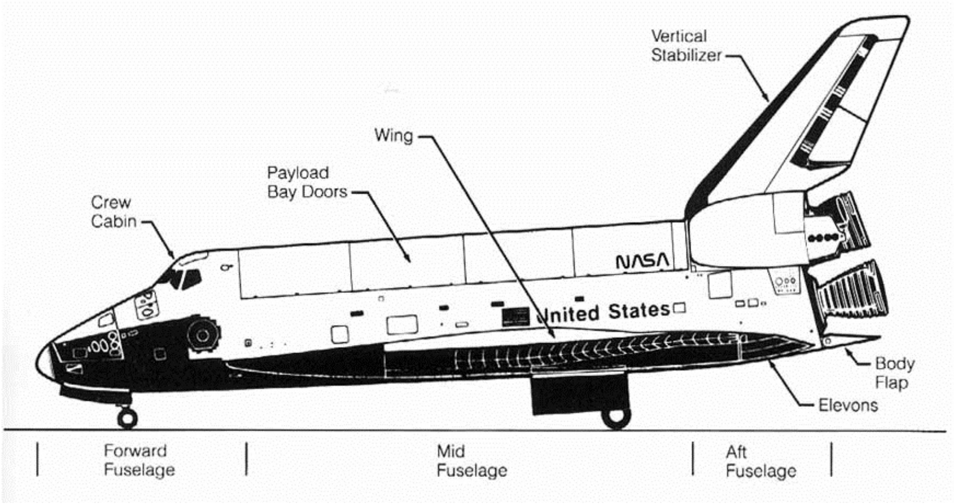

Figure 2.1: Drawing of the Space Shuttle orbiter. Image credit: NASA.

The Shuttle was expected to reduce the cost of launching payloads to space by amortizing the development and maintenance cost over flights occurring at a rate of around once per week. However, this flight calender never materialized due to the complexity of the Space Transportation Systems. Especially the maintenance of the thermal protection system and the main engines proved to be extremely labor intensive (O'Leary, 1973). This was primarily due to technological limitation and design decisions made during the design and development of the Shuttle. For example, the thermal protection system consisted of brittle ceramic tiles with each specifically designed for a unique spot on the outside of the vehicle. The material of the tiles did not ablate during reentry and is therefore better suited as heat shield for a reusable spaceplane compared to an ablative heat shield. However, a lot of tiles were found damaged after the Shuttle landed and had to be frequently replaced due to their fragility (Cooper and Holloway, 1981).

The Space Shuttle main engines use a hydrogen/oxygen-staged combustion cycle and are capable of producing a relatively high thrust at very high specific impulse. This is achieved by using complex high-pressure turbo-machinery, which subjected some parts to very high stresses and wear (VanHooser and Bradley, 2011). This led to the decision to take apart the engines after every flight, check the components for damage, replace worn elements, and put it back together again after every flight (Korkegi et al., 1983). This was a very time consuming process.

The lessons from the Shuttle program were applied to following projects, such as the Venture Star and the Delta Clipper. The Venture Star employed more robust metallic tiles as thermal protection system and used a lifting body to minimize the mass penalty of aerodynamic surfaces on the empty mass fraction of the vehicle. This and the use of a rocket engine with aerospike nozzle made it potentially capable of putting a significant amount of payload into orbit without jettisoning any parts (Reed, 1997). The Venture Star project was cancelled shortly before a first sub-scale prototype called X-33 was completed.

In conclusion space planes are often considered as the solution to the fully-reusable launch vehicle problem. However, these wings add significant structural mass to the vehicle, which significantly reduce the structural mass fraction of the vehicle and therefore its capacity to reach orbit with a significant payload.

2.1.2. Ballistic Launch Vehicle

Returning a vehicle by means other than wings have been considered early in the history of spaceflight as well. Especially ideas that would not burden the vehicle with as much structural mass as wings promise to be a practical path reusability.

The first large-scale effort made to recover a rocket for reuse was during the Mercury program for the Redstone rocket. Parachutes were intended to slow the descent of the rocket for a soft splashdown in the Atlantic after separation. Component and system tests have been performed, but funding was cut before the recovery system could be flight tested (Miller et al., 1964). This concept has been later successfully realized for the Space Shuttle solid rocket boosters and flight tested on several Falcon rockets. The benefit of this recovery system is its relative simplicity as the only required equipment is a parachute system and corresponding control mechanisms.

However, the uncontrolled descent and contact with the ocean water is not always acceptable and depends on the design of the rocket. The Shuttle solid rocket booster is essentially a hollow steel casing after burnout with relatively thick walls to handle the pressure during the burn. This type of rocket is well suited for such a recovery methods. Liquid rockets have relatively thin aluminum tanks, which are susceptible to the stresses of reentry and splashdown. The delicate parts in the turbo machinery do not tolerate corrosive salt water well over an extended period of time and would require extensive refurbishment (Novak et al., 2002).

The Falcon 1 and Falcon 9 first stage were equipped with parachutes on early flights, but all recovery attempts failed due to excessive aerodynamic stresses exerted on the thin-walled tank structure during descent[6].

The unsuccessful attempts to recover large liquid rocket booster on a suborbital trajectory with parachutes as well as the payload hit suffered by winged vehicle lead to the consideration of propulsive descents and landings. The principle was first demonstrated by the various lunar lander designed to touch down softly under rocket thrust with the Apollo Lunar Module being the most famous example (Gatland, 1976).

One of the first vehicle used to test this concept on Earth as return method for launch vehicle is the DC-X, a vertical takeoff and landing (VTOL) rocket intended as a sub-scale test vehicle for the single-stage-to-orbit Delta Clipper. On top of testing this approach to returning a vehicle back to the launch site the test program also included many lessons learned from the Space Shuttle program mentioned earlier. This has resulted in a comparatively cheap development and operations cost for the DC-X with an unprecedented launch crew of only three and a total project team of 100 people[7]. The vehicle proved the concept of vertical takeoff and landing of a rocket on Earth before it was canceled first by the Air Force and then finally by NASA in favor of the Venture Star project.

In contrast to conventional rocket design philosophy, which is to make the body cylindrical, the DC-X had a rectangular cross section with rounded corners. This outer mold line was used to improve the low lift and therefore crossrange capability of the vehicle during reentry. A shortcoming also observed by ESA with their FESTIP Concept 3, a VTOL rocket concept similar to the DC-X but with a cylindrical body. The uncertainties surrounding this design compared to space plane concepts lead to the discontinuation of FESTIP-3 in the early concept phase (Dujarric, 1999).

The successful flights of the DC-X inspired many private companies, such as Blue Origin and Masten Aerospace to develop their own vehicle based on propulsive landings. These efforts have resulted in the successful development of partly and fully reusable launch vehicle currently entering flight testing. One of these vehicles is the New Shepard, a sub-orbital launch vehicle intended to boost microgravity experiments and space tourists above the Karman line in a suborbital trajectory. The capsule on top of the rocket containing the payload separates from the booster and lands with parachutes. The propulsion module uses its rocket engine to decelerate and touch down on a landing pad near the launch site. The propulsion module is shown in Figure 2.2(a) shortly after landing from its third test flight.

The previously-mentioned Falcon 9 rocket is a two stage orbital launch vehicle with the first stage capable of returning to the launch site or landing on a seaborne landing platform. The second stage is currently expended after every flight, but SpaceX voiced the intention of making entire Falcon 9 reusable. The Falcon 9 first stage is shown in Figure 2.2(b) as it stands on the landing pad after launching the ORBCOMM-2 satellite into orbit.

A prevailing idea for reusable launch vehicle is to make it also a single-stage-to-orbit (SSTO) launcher. A launcher that does not need to jettison any elements to reach orbit has advantages in terms of ground operations and recovery. Removing the stacking of rocket stages on the ground results in a faster and more streamlined processing of vehicles for relaunch. Also, since all elements of the vehicle stay connected, recovery is limited to just one element instead of several, all of which have to be tracked, controlled, and returned separately. This comes at the cost of not using staging, which increases the final velocity of any given payload for the same structural mass fraction. The success of the Falcon 9 vehicle in becoming the first commercial launch vehicle with a reusable first stage il-

---

[6] `https://www.nasaspaceflight.com/2009/01/musk-ambition-spacex-aim-for-fully-reusable-falcon-9/`

[7] `http://www.ae.utexas.edu/courses/ase333t/past_projects/03fall/delta_clipper/DeltaClipperPaper.pdf`

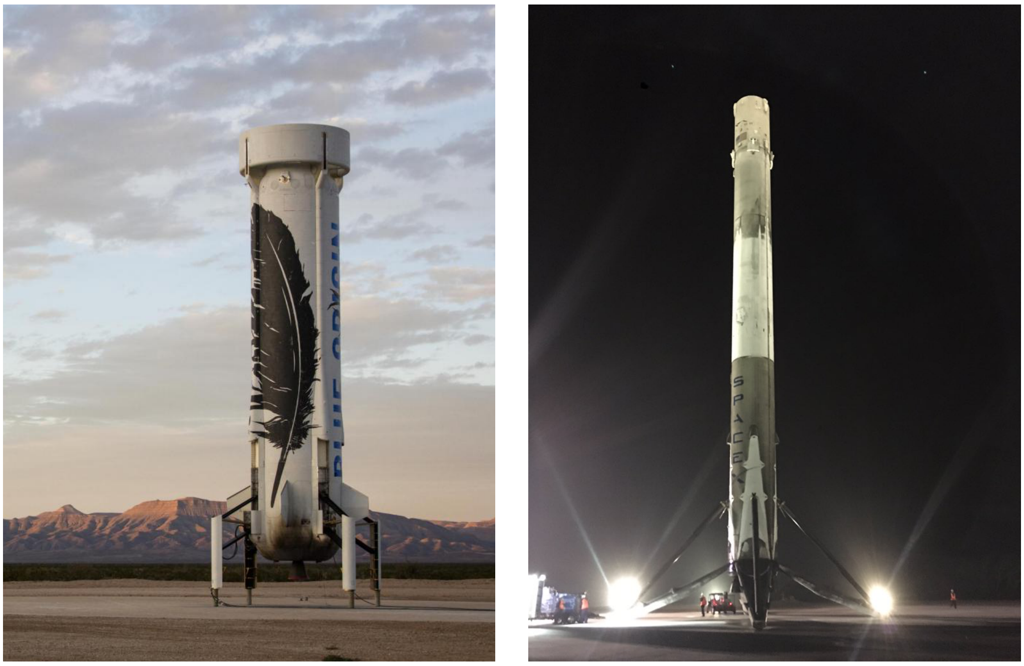

(a) New Shepard propulsion module. Image credit: Blue Origin

(b) Falcon 9 first stage. Image credit: Elon Musk

Figure 2.2: Blue Origin's New Shepard propulsion module and SpaceX's Falcon 9 first stage shortly after landing.

lustrates that point well. It is capable of placing a competitive amount of payload into diverse orbits despite the fuel and devices required for return and landing, while single-stage-to-orbit launch vehicle have to battle with diminishing payload mass fractions (Ambrosius, 2009).

2.2. Existing Launch Vehicle Upper Stages

The goal of this section is to analyze the mission and characteristics of three different types of existing expendable upper stages. This is to ensure that the model of the reusable upper stage used in this study is representative for a typical upper stage and can in theory perform the same mission.

After stage separation at a certain altitude and velocity a upper stage is tasked with increasing the velocity of the stack sufficiently to inject a payload into a desired orbit. For precise control over the orbit injection and payload deployment attitude an upper stage is often equipped with attitude control and ullage thrusters in addition to the main engine and thrust vector control systems. The Centaur, Ariane 5 ESC-A, and Falcon 9 second stage are such examples of currently operational upper stages. They also illustrate some of the variety among this type of vehicles.

2.2.1. Centaur-5

The Centaur upper stage is one of the earliest rocket stages developed as a universal upper stage and the first to use liquid hydrogen and liquid oxygen as propellant. It is powered by one or two RL-10 expander cycle rocket engines, which have a specific impulse of 450 s. With such a high efficiency it enabled numerous interplanetary missions over the decades starting with the Surveyor landers in the early 60s up to the recent Jupiter-bound Juno spacecraft[8] (Rudman and Austad, 2002).

In the time period since its development the Centaur has undergone several modifications and improvement to enhance performance and enable the integration into different launch vehicle such as the Atlas series of launchers or the Titan III. An image of the latest generation of the Centaur in the dual-engine configuration as second stage for the Atlas V is shown in Figure 2.3(a). Its dimensions and some performance characteristics of the vehicle are given in Table 2.1 (Wilkins, 2010).

Ground launched rockets and rocket stages have to balance specific impulse with thrust to maximize

---

[8] `https://www.nasa.gov/mission_pages/juno/multimedia/pia14381.html`

Centaur	
Length	12.68 m
Diameter	3.05 m
Empty mass	2247 – 2462 kg
Propellant mass	20830 kg
RL-10 thrust	99.2 kN (Vacuum)
I_{sp}	450 s
Burn time	700 s
Total impulse	9195.4 kNs

Table 2.1: Dimensions and characteristics of the Centaur stage (Wilkins, 2010).

final velocity while minimizing gravity losses. Rocket stages that are already in orbit benefit the most from a high specific impulse and thrust becomes less important. This gives the Centaur with its high energy propellant combination an edge for missions to higher orbits and interplanetary trajectories over upper stages such as the Falcon 9 second stage, which uses heavier and less energetic propellants. However, for heavy payloads and a slow ascent more thrust is beneficial to reduce gravity losses by minimize the time climbing to orbit (Ambrosius, 2009).

2.2.2. Ariane 5 ESC-A

While the Centaur stage is a generalized vehicle and part of many different launch systems the ESC-A stage is specifically designed as a cryogenic upper-stage for the Ariane 5. The Ariane 5 launch vehicle consists of a liquid hydrogen/liquid oxygen powered central core flanked by two solid rocket boosters. While the solid rocket boosters provide the initial thrust to push the rocket out of Earth's gravity well the core produces the majority of the impulse to reach orbit (Perez, 2011).

The first upper stage on the Ariane 5 was mainly used for final orbit insertion. It was powered by a less potent storable hypergolic propellant combination to reliably ignite the upper stage multiple times in space. With a specific impulse of 324 s the overall impulse was relatively low and the launch system relied on the core for most of the change in velocity.

As satellites destined for the geostationary orbits grew in size and number a more capable upper stage was required. ESC-A was developed as an upper stage option for geostationary satellites and interplanetary spacecraft. Similar to the Centaur upper stage it leverages the same advantage of a liquid oxygen and liquid hydrogen propellant combination in terms of efficiency to achieve a high terminal velocity (Perez, 2011). The ESC-A upper stage is shown in Figure 2.3(b) as it is raised for stacking on the Ariane 5. Dimension and performance data of the ESC-A are given in Table 2.2.

Note here how the ratio between the length and the diameter contrasts with the length and diameters of the Centaur upper stage. While a rocket is generally designed to be as thin as possible to reduce the air drag during ascent this is less critical for an upper stage, since they are often ignited outside the atmosphere. Instead keeping the diameter of the vehicle constant over its length becomes the main concern, since changes in the diameter of the entire rocket stack create shockwaves during ascent and thereby add additional drag. Therefore to remain in-line with the Ariane 5 core the ESC-A has the same diameter of 5.4 m. For a desired tank volume this results in a given tank length. Overall the ESC-A is relatively short but wide compared to the Centaur's slim but long shape. The diameter of Centaur is inherited from the diameter of the Atlas II on which it was first used as high energy upper stage (Rudman and Austad, 2002).

2.2.3. Falcon 9 Second Stage

The Falcon 9 is a two-stage launch vehicle, which uses a liquid oxygen and RP-1 combination as propellant. The same engine type, tank construction, and propellant combination is used across both stages to increase commonality in the manufacturing and ground handling, which eliminates the cost of a separate production line and ground infrastructure for a different type of propellant. The second stage is for the mostly a shorter version of the first stage with the same diameter of 3.66 m and therefore uses most of the same tooling and ground handling equipment. The second stage is powered by a derivative of the Merlin 1D engine also used on the first stage but modified for use in vacuum and increased redundancy (SpaceX, 2015). The Falcon 9 launch vehicle pays for the cost savings through common-

Ariane 5 ESC-A	
Length	4.711 m
Diameter	5.4 m
Empty mass	4540 kg
Propellant mass	14.9 t
HM-7B thrust	67 kN (Vacuum)
I_{sp}	446 s
Burn time	945 s
Total impulse	6519.1 kNs

Table 2.2: Dimensions and characteristics of the Ariane 5 ESC-A stage (Perez, 2011).

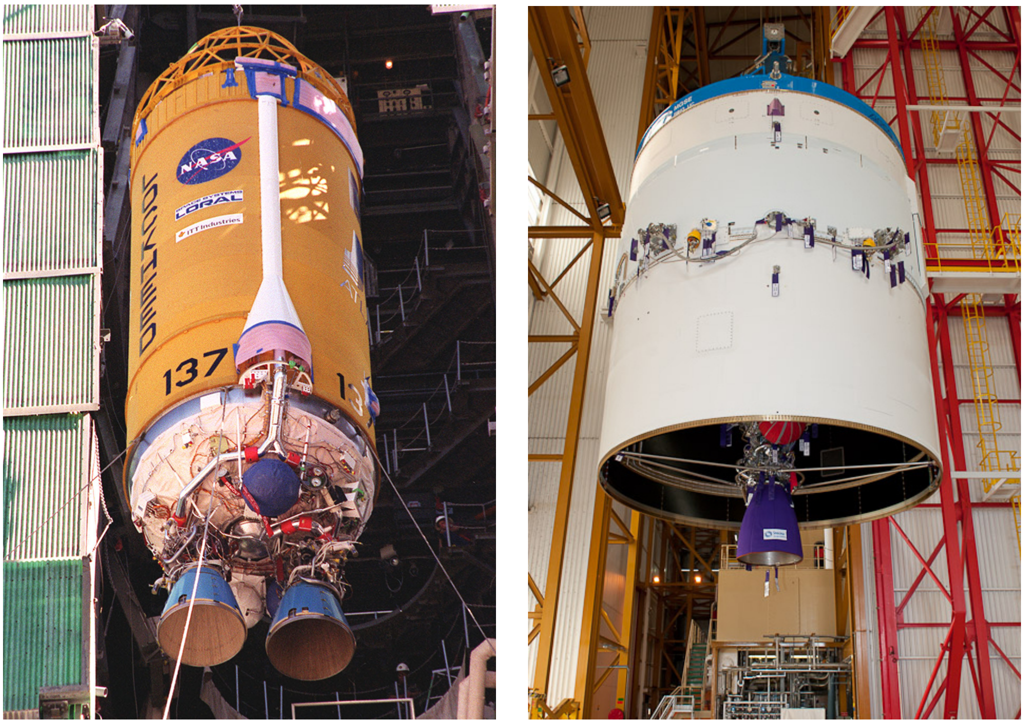

(a) Centaur. Image credit: ULA (b) Ariane 5 ESC-A. Image credit: Arianespace

Figure 2.3: The Centaur and ESC-A cryogenic upper stages.

ality by the hit in performance especially for missions to geostationary orbits and higher compared to using the more efficient liquid hydrogen for the upper stage. However, for missions to low Earth orbit this disadvantage is somewhat made up for by the higher thrust, which as mentioned earlier minimizes the burn duration and therefore gravity losses. A rendition of the second stage with the payload still attached is shown in Figure 2.4.

Contrary to the Centaur and the ESC-A very little data on the dimensions of the Falcon 9 and especially its upper stage is publicly available. Available numbers are summarized in Table 2.3 (SpaceX, 2015; Website, 2016). These refer to the latest variant of the Falcon 9 second stage, which changed significantly from the first version. Since its first launch the Merlin engines have undergone several upgrades in thrust and specific impulse, which enabled the stretching of the first and second stage. From the given visuals of the different versions of the Falcon 9 upper stage the vehicle is estimated to have a diameter to length figure between the Centaur and the ESC-A with the first version having a ratio closer to the ESC-A and the latest version similar to the Centaur.

The mass of the Faclon 9 second stage alone has not been published yet. Some unofficial estimates for the dry mass of the vehicle range from 3900 tons to 4500 tons (Blau, 2016; Kyle, 2015).

In Table 2.4 the orbit insertion accuracy of the Falcon 9 is shown. This means that the orbit the upper stage reaches for any given mission is dispersed by the specified amount around the target.

Figure 2.4: Rendition of the Falcon 9 second stage after engine cutoff still attached to the payload. Image credit: SpaceX

Falcon 9 Second Stage	
Diameter	3.66 m
Merlin Vacuum thrust	934 kN (Vacuum)
I_{sp}	348 s
Burn time	397 s

Table 2.3: Available dimensions and characteristics of the Falcon 9 second stage (SpaceX, 2015; Website, 2016).

Due to, for example, the effect of state estimation errors, random engine shutdown transients or thrust vector misalignment from the expected direction.

These uncertainties define the final orbit and therefore indirectly the initial condition for reentry of a reusable upper stage. At least one maneuver is required to deorbit the vehicle again and may be used to adjust the trajectory to a certain extent. That and additional maneuvers can be used if necessary to set up the reentry given sufficient time. However, for a quick turn around a return to the launch site is desirable within a short amount of time and may limit the time available for orbital corrections.

Modern orbit determination techniques refine the position estimate over time and converge more or less quickly on a solution, which depends on the quality of the measurement data and the orbit model. The position is usually measured indirectly through ranging from the ground. This may not always be possible, since not all orbits can be covered by ground stations or are too expensive to establish. Using GPS for ranging is a promising inexpensive alternative to determine the vehicles orbit globally and with reasonably high accuracy (Schutz et al., 2004). However, the limited time in orbit may still be to short to allow for an accurate orbit determination.

To account for these uncertainties the initial state of the vehicle is randomized in the dispersion analysis according to the orbit insertion accuracy provided in Table 2.4.

Variable	LEO	GTO
Perigee	± 10 km 3σ	± 10 km 3σ
Apogee	± 15 km 3σ	± 500 km 3σ
Inclination	± 0.1 deg 3σ	± 0.1 deg 3σ
RAAN	± 0.1 deg 3σ	± 0.1 deg 3σ
Argument of Perigee	N/A	± 0.3 deg 3σ

Table 2.4: Orbit insertion accuracy as published by SpaceX (SpaceX, 2015).

(a) Apollo Command Module. Image credit: NASA.

(b) Soyuz Descent Module. Image credit: Roscosmos.

Figure 2.5: The Apollo and Soyuz reentry capsules.

2.3. Reentry vehicle

The ability to safely and reliably bring a vehicle with its cargo back to Earth is a critical requirement to enable the manned exploration of space. Several manned reentry vehicle were developed and have successfully returned astronauts back to Earth (Chertok, 2005). A secondary field in which reentry vehicle play an important role is in scientific and military reconnaissance. While telecommunication made the need to recover spy imagery obsolete reentry is still a necessity for scientific landing probes to planets or moons with a sufficiently thick atmosphere such as Mars, Venus, or Titan (Knocke et al., 2004; Lebreton et al., 2005; Leverington, 2001). In this section the Apollo Command Module, the Soyuz Descent Module and the EXPERT reentry demonstrator are presented. They are used as examples to highlight the characteristics of reentry vehicles.

2.3.1. Apollo Command Module

The Apollo spacecraft was designed to take three astronauts to the Moon and return them safely back to the Earth. It consists of the Command Module (CM), which contains the pressurized cabin for the crew and is capable of reentry from lunar return trajectories, and the Service Module (SM), which contained the propulsion subsystem, power subsystem and most of the fluids required for the journey to the moon and back (Brooks et al., 1979). A picture showing the Apollo CM after splashdown in the Pacific is shown in Figure 2.5(a).

The Apollo CM thermal protection system consists of a spherical ablative heat shield facing the incoming airstream with a conical metallic shell covering the backside of the structure. This shape allowed for a stable vehicle capable of relatively high angles of attack without subjecting the side walls to the incoming airflow. Flying at an angle of attack and thereby producing lift was necessary to reduce the otherwise excessive G-loads on the astronauts during a fully ballistic reentry from the Moon. This comes at the cost of interior volume for a given base diameter compared to a more cylindrical body such as the Soyuz.

2.3.2. Soyuz Descent Module

The Soyuz spacecraft is a direct descendant of the Vostok spacecraft and is designed to ferry three people into low Earth orbit and back. The spacecraft consists of three modules, the Instrumentation and Service Module, which performs similar functions to the Apollo SM, the Descent Module, which is the launch and reentry capsule, and the Orbital Module, which provides space for the crew and experiments in orbit (Wachtel, 1982). A derivative of the Soyuz spacecraft was also intended as a Lunar ferry just like the Apollo spacecraft but got canceled together with the Soviet Moon program (Casey, 2013; Harvey

Figure 2.6: EXPERT reentry vehicle demonstrator. Image credit: ESA.

and Zakutnyaya, 2011). The Soyuz Descent Module after touchdown in the desert of Kazakhstan is shown in Figure 2.5.

The design of the Soyuz Decent Module reflects the need for space to accommodate three astronauts in a 2.2 m diameter capsule through the use of a bell shaped outer mold line for the reentry vehicle[9]. In contrast the Apollo capsule is 3.9 m in diameter to adequately provide the crew with living space for the trip to the Moon while minimizing the exposure of the backside to the extreme heat of reentry. The shallow side wall angles of the Soyuz capsule mean that the walls are more exposed to the incoming airflow and therefore also require substantial thermal shielding compared to the Apollo capsule. This may also be the case for the cylindrical body of a reusable upper stage and suggest that it too requires some thermal protection on its side walls.

2.3.3. EXPERT

Another example of a reentry vehicle is the EXPERT reentry demonstrator shown in Figure 2.6. While it was never launched its design shares some characteristics with the reusable upper stage studied in this report. Most notably the shape of EXPERT is closest to the vehicle proposed by SpaceX out of the three reentry capsules presented here. It resembles a blunted cone body with shallow side wall angles making it relatively long. To improve stability four fixed aerodynamic flaps are added to the aft of the vehicle, a technique that is also implemented for one of the configuration of the reusable upper stage presented here. The flaps are fixed at a constant deflection angle and create a stabilizing moments pushing the nose of the vehicle into a stable attitude. The flaps are also used as experiments to study flow separation, reattachment, and interaction with the surface (Barrio et al., 2011; Massobrio et al., 2007). An image of an EXPERT test article is shown in Figure 2.6.

2.4. Reusable Upper Stage Concepts

Reusable upper stages have received relatively little attention compared to space planes or SSTOs, since such vehicle only become important once the first and often most expensive stage is reusable. However, recently some concept studies of reusable conventional upper stages have been published as part of entire reusable multistage launch systems. Most notably the Kister K1 and the Falcon 9 are two serious attempts at designing a two-stage launch system capable of landing their individual stages

---

[9] `http://wsn.spaceflight.esa.int/docs/Factsheets/35%20Soyuz%20LR.pdf`

back on Earth after delivering their payload into orbit. Their respective upper stages, the K1 Orbital Vehicle and the Falcon 9 second stage, are presented in this Section.

2.4.1. Kister K1 Orbital Vehicle

The Kister K1 is a fully reusable two-stage launch vehicle designed and under development by the company Kister Space Systems. A concept drawing of the second stage of the K1, called the Orbital Vehicle (OV), is shown in Figure 2.7(a). In this figure the design choices made for the K1 OV are apparent. To protect the vehicle from the heat of reentry a ceramic heat shield is used on the nose and parts of the conical section at the aft of the vehicle. The cylindrical body and the rest of the conical aft section is covered by insulation blankets. The main engine and AOCS thrusters are behind the conical aft and therefore shielded from the hypersonic airstream by the wake (Meyerson et al., 1999).

While the rational behind such a vehicle design has not been made public by Kister. However, the shape of the vehicle suggests that Kister traded off the diameter of the upper stage for the adapter, which pushed the center of pressure back behind the center of mass and therefore stabilizes the vehicle during reentry, similar to a Shuttlecock in Badminton. This improves the stability of the vehicle during reentry but sacrifices valuable cross-sectional area for large payloads and increases the drag of the vehicle. Key figures of the K1 Orbital Vehicle as published by Kister are summarized in Table 2.5.

Kister K1 Orbital Vehicle	
Length	18.6 m
Diameter(cylindrical section)	4.3 m
Mass(fully fueled)	131.8 t
AJ26-60 thrust	1760 kN (Vacuum)
$\mathrm{I_{sp}}$	331 s
Burn time	230 s

Table 2.5: Dimensions and characteristics of the Kister K1 Orbital Vehicle (Perez, 2011).

2.4.2. Reusable Falcon 9 Upper Stage

The leadership of SpaceX believes that a rapidly reusable launch vehicle is key to fulfilling the companies mission statement of drastically reducing the cost for access to space and opening up the solar system to human colonization. For that purpose SpaceX intended the Falcon 9 launch vehicle to eventually be fully reusable right from its inception[10]. At the November 2016 the propulsive descent and landing of the Falcon 9 first stage has been achieved multiple times and its reuse for an orbital launch is planned for the near future (de Selding, 2016).

Along with a reusable first stage SpaceX also intended to reuse the second stage of the Falcon 9 as well. Initial plans called for a reentry protected by a heat shield and final descent under parachutes but later revised the idea by using propulsive landing as the final deceleration method similar to the first stage (Dinardi et al., 2008). The development of a reusable second stage for the Falcon 9 was finally halted in favor of the next generation SpaceX rocket after the Falcon Heavy. A screenshot of the proposed reusable second stage as published in a SpaceX promotional video is shown in Figure 2.7(b)[11].

This vehicle shows several similarities to the K1 Orbital Vehicle, most notably the heat shield mounted at the nose of the vehicle with the main engine and other external sensitive equipment protected in the wake of the upper stage. The four struts protruding out of the stage around the thrust cone are the landing legs. The engine itself lies within the fuselage extended over the thrust cone. The engine is equipped with an extendable nozzle similar to the Vinci engine to reduce its length and retract the nozzle deeper into the wake during reentry (Pichon et al., 2005).

The most significant difference to the K1 OV is that the reusable Falcon 9 upper stage is entirely cylindrical and has no conical section in the aft for stabilization, thereby maintaining the same constant diameter as the first stage. This may either be due to a SpaceX internal realization that the second stage in its current configuration is already aerodynamically stable. Or it may simply indicate the early

---

[10] `http://www.spacex.com/about`

[11] The promotion video has since been taken down by SpaceX. The full video can still be viewed at `https://www.youtube.com/watch?v=OX2-qEC7P_I` as of 23.11.2016.

(a) K1 Orbital Vehicle. Image credit: Kister. (b) Falcon 9 2nd stage. Image credit: SpaceX.

Figure 2.7: Reusable upper stage concepts published by Kister and SpaceX.

stage of the development, where the case for the aerodynamic stability of such a reusable upper stage was not yet determined and the rendering shows just an artist impression.

2.5. Reference Vehicle

In principle any conventional upper stage could be used as baseline to model a reusable upper stage capable of controlled reentry and descent from orbit, with some vehicles more or less suitable for such a task. However, given that the Falcon 9 upper stage has been proposed as reusable upper stage by its manufacturer and concept art describing its mode of operation were presented, this makes it a good choice as reference vehicle to study its dynamics. The baseline reusable upper stage used in this work is therefore modeled after the Falcon 9 upper stage.

2.5.1. Dimensions

The Falcon 9 reusable upper stage shown in Figure 2.7 is in the reentry configuration. In this configuration the bell nozzle of the engine is retracted and the landing legs bend into the wake of the vehicle to protect them from the free stream. From the illustration it is noted that the location of the heat shield is in the front and the aft part of the stage's 'fuselage' is elongated. A technical drawing of the expendable Falcon 9 upper stage as used on the Falcon 9 1.0 is shown in Figure 2.8 for comparison (Dinardi et al., 2008).

Few technical details about the Falcon 9 launch vehicle have been published. The only dimensions confirmed by SpaceX is the radius of the vehicle of 3.66 m and a total length of the Falcon 9 1.0 of 54.9 m (SpaceX, 2009).

Assuming Figure 2.8 shows the second stage at the right scale and correct aspect ratio the known diameter of the vehicle can be used to approximate the other dimensions from the image and determine the relative position of elements such as the engine, bulkheads, spherical tanks, etc. Each significant

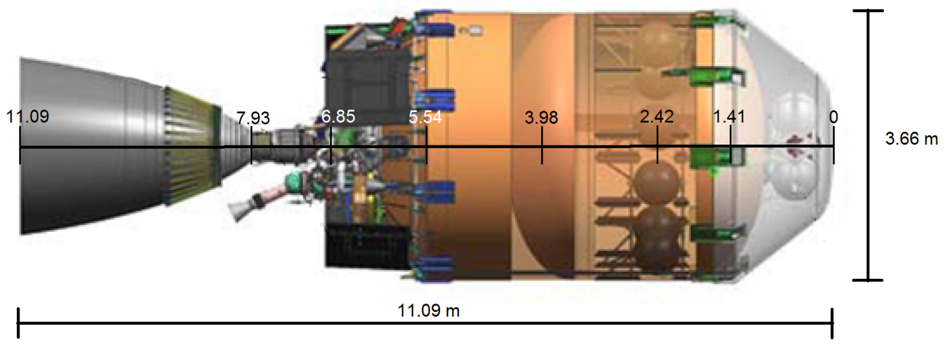

Figure 2.8: CAD drawing of the Falcon 9 (v1.0) upper stage (Dinardi et al., 2008). Dimension estimation and overlay done by the author.

Significant point	Location
Vehicle nose/Payload adapter	0.0 m
First bulkhead	1.41 m
Helium/RCS tanks	2.42 m
Second bulkhead	3.98 m
Third bulkhead/top of thrust structure	5.54 m
Bottom of thrust structure/top of engine	6.85 m
Bottom of engine/top of nozzle	7.93 m
Bottom of nozzle	11.09 m

Table 2.6: Significant points and locations from the nose of the vehicle shown in Figure 2.8.

spot has been marked in Figure 2.8 and is listed in Table 2.6. These numbers are used in Section 3.4 to estimate the mass properties of the upper stage.

2.5.2. Shape

In Section 2.4 details about the Falcon 9 second stage are presented. The reusable upper stage used in this study is based on that vehicle. To enable it to successfully perform a controlled reentry into Earth's atmosphere it must be adapted and requires additional elements, such as a heat shield, hull modifications, or aerodynamic surfaces, if necessary. In this section three different configuration of a reusable upper stage are presented, which ensure that at least one of them is stable and capable of performing the mission. These three configuration are further analyzed in the following chapters. First the shape of the heat shield front surface is constructed. The same heat shield shape is used in all three configurations. Then the modifications are presented, which define each configuration, namely the standard baseline vehicle, the stage with extended aft, and the stage with aerodynamic surfaces.

Heat shield surface The primary surface interacting and deflecting the hypersonic flow while protecting the vehicle from the heat and loads of reentry is the heat shield. The heat shield shape used for the upper stage consist of a hemispherical frontal section, which transitions into a torus. The torus connects the hemispherical frontal section to the main body of the vehicle. This shape has been used on many manned and unmanned spacecrafts including the Apollo CM, which returned Astronauts from the moon. As mentioned earlier about the Apollo capsule, such a shape has a stabilizing influence yet allows the vehicle to easily be trimmed to a desired angle of attack.

While the blunted cone is shown to be the most stable shape for a reentry vehicle a hemispherical shape more easily allows for a passive trim angle through modest shifts in the center of mass of the vehicle (Button et al., 2009). The blunted cone furthermore requires the center of mass to be inside the hemispherical or the conical section of the vehicle to be stable. If the center of mass is behind the conical section the configuration becomes unstable while a hemispherical heat shield with a large radius of curvature continues to exert a stabilizing effect. The contour of the Apollo vehicle is given in Figure 2.9.

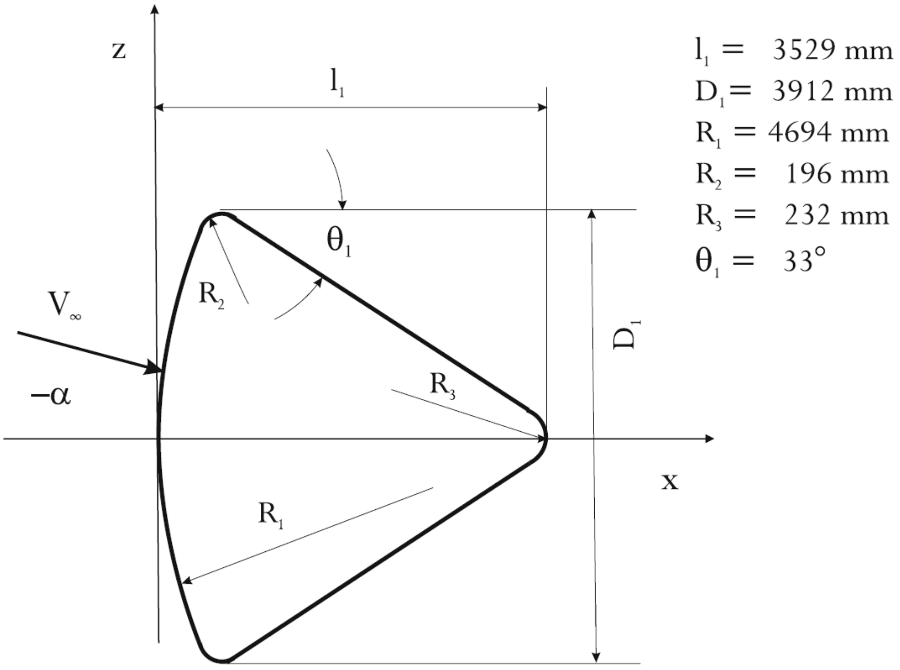

Figure 2.9: Contour of the Apollo reentry capsule with dimensions as given by Weiland (Weiland, 2014).

The influence of several main heat shield radii on the moment coefficients is analyzed in Appendix C. There it is found that with a more flat main heat shield surface the higher the stabilizing effect with diminishing gains at radii higher than 2.5 times the radius of the vehicle.

The radius of the toroidal section is modeled after the Apollo capsule by scaling it proportionally to the diameter of the vehicle. While it has a negligible effect on the stability it determines along with the angle of attack the heating experienced at the edge of the heat shield, which may even exceed the heat rate at the stagnation point due to complex flow phenomena (Dirkx, 2011).

To construct a smooth heat shield requires the calculation of the angle of transition from the hemispherical section to the toroidal section. The transition angle is the angle at which both the heat shield surface and toroidal surface have he same gradient. The center of the hemisphere that forms the front of the heat shield is used as reference point, which lies along the longitudinal axis of the vehicle. Using the hemispherical front radius R_1, the cylindrical radius of the vehicle $D_1/2$, and the radius of the edge torus R_2 the angle of transition θ_{trans} can be found with the following equation.

$$\theta_{trans} = \arcsin\left(\frac{\frac{D_1}{2} - R_t}{R_1 - R_2}\right) \tag{2.1}$$

Since the radius of the heat shield edge and the upper stage diameter is fixed, the transition angle is a function of main heat shield radius R_h only. Using the transition angle between the hemispherical front and the edge torus of the heat shield coordinates can be found for any point along the contour of the vehicle's heat shield and main body. The aerodynamic coefficient generator Missile DATCOM uses the coordinate vector **X**, which is a vector of points along the longitudinal axis of the vehicle, and **R**, which is a vector of radii corresponding to the points given in **X**, as input method for the geometry of the vehicle. Both can be calculated for the heat shield using Equation 2.2 and Equation 2.3 respectively as a function of θ.

$$X_i\,(\theta) = \begin{cases} R_1\,(1-\cos\theta) & \text{for} \quad 0 \leq \theta \leq \theta_{trans} \\ X\,(\theta_{trans}) + R_2 \sin\,(\pi-\theta) & \text{for} \quad \theta_{trans} > \theta \geq \pi \end{cases} \tag{2.2}$$

$$R_i\,(\theta) = \begin{cases} R_1 \sin\theta & \text{for} \quad 0 \leq \theta \leq \theta_{trans} \\ R\,(\theta_{trans}) + R_2\,(\cos\,(\pi-\theta) - \cos\,(\pi-\theta_{trans})) & \text{for} \quad \theta_{trans} > \theta \geq \pi \end{cases} \tag{2.3}$$

The contour of the vehicle and points used as input geometry to generate the aerodynamic coefficients are plotted in Figure 2.10. The final point at the end of the vehicle simply uses the radius at the last point of the heat shield and extends it by the length of the upper stage tank. The engine nozzle is left out of the contour vector used in Missile DATCOM due to limitations in the tool to account for shadowing. Since at hypersonic velocities the vehicle leaves an evacuated wake, the effect of leaving out the shadowed part of the vehicle should be small with only little contact between it and the surrounding airflow. To determine the magnitude of the effect of the nozzle on the aerodynamics of the vehicle for certain a more sophisticated analysis of the airflow around the entire vehicle is required, which takes shadowing and the complex airflow around the wake of the vehicle into account. To do this within the time frame of this study, however, was deemed impractical and is left for future research.

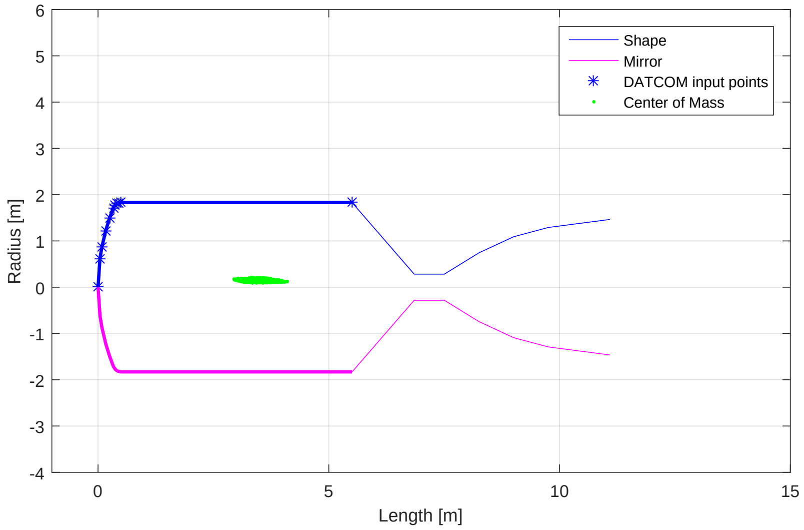

Figure 2.10: Contour of the reusable upper stage including input points used for Missile DATCOM.

The cloud of green dots is the result of a sensitivity analysis on the center of mass location in response to uncertainties in the mass of individual mass elements of the upper stage. Details on the sensitivity analysis are discussed in Section 3.4.

Configuration Since the aerodynamic stability of the upper stage shown in Figure 2.10 is not yet known, three variants of the upper stage are introduced to ensure at least one stable configuration can be found. First the Falcon 9 1.0 second stage as shown in Figure 2.8 modified with an appropriately shaped heat shield as plotted in Figure 2.10 is analyzed in terms of static stability. Then changes are introduced with the goal of improving the stability of the vehicle. The second vehicle studied has an extended aft fuselage and the final configuration is equipped with aerodynamic surfaces. The focus of this work is on the dynamics of the vehicle during reentry and hypersonic descent. Details related to the terminal deceleration and landing such as landing legs, propulsive descent, and touchdown are left for another study and are therefore not taken into consideration in the vehicle model.

- **Baseline**: The baseline configuration serves two purposes. First is to determine the stability of an minimally altered upper stage during reentry. Finding a working solution for such a case has benefits in terms of mass savings, development effort, and retaining the interface between the first and second stage. The second purpose for analyzing the baseline configuration is to determine the margins in the stability of the vehicle and how the instability develops as a function of the location of the center of mass.

  The baseline configuration uses the dimensions measured in Figure 2.8 and a heat shield as described in Subsection 2.5.2. The vehicle is controlled by banking the direction of the lift vector.

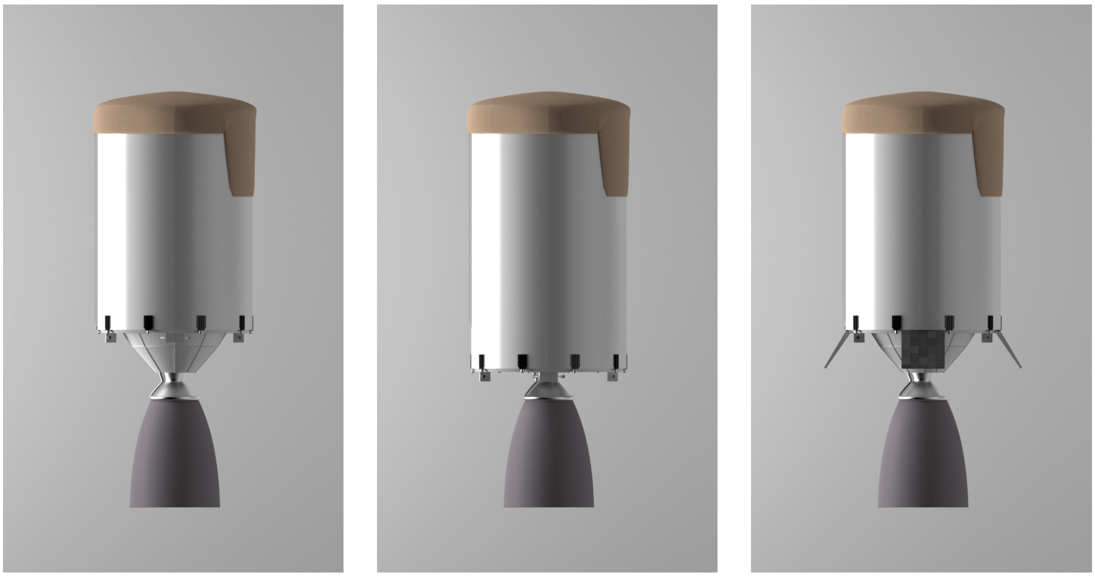

(a) Baseline configuration (b) Configuration with extended aft (c) Configuration with aerodynamic surfaces/flaps

Figure 2.11: Reusable upper stage variants studied in this work.

Lift is created by shifting the center of mass vertically such that the trim angle of attack becomes non-zero. A rendition of the baseline upper stage is shown in Figure 2.11(a).

- **Configuration with aft-skirt**: An aft skirt attached to the back end of the tank is expected to have a stabilizing effect on the upper stage as it increases the area facing the flow behind the center of mass. This strategy may also be under consideration by SpaceX, since the vehicle shown in their promotion video in Figure 2.7(b) also sports an extended fuselage reaching past the engine combustion chamber.

  While such an extension requires additional structural mass it only minimally compromises the interface between the first and second stage. This concept uses the same general shape as the baseline except for the extension at the back and is therefore constructed simply by moving the final contour point in Figure 2.10 further back. This configuration is shown in Figure 2.11(b).

- **Flapped configuration**: The third configuration has the same shape as the baseline but uses flaps to stabilize the vehicle. The flaps generate lift locally, which act at a distance from the center of mass and thereby generate a moment, which counteract the vehicle's unstable pitching moment.

  Similar to the previous two configurations a shift in the center of mass in the vehicles vertical axis introduces a passive trim angle of attack. An artist rendition of the configuration using aerodynamic surfaces is shown in Figure 2.11(c).

  This configuration uses the same aerodynamic coefficients as generated for the baseline. The additional forces and moments produced by the flaps are added in the equations of motion using Newtonian flow theory and are described in Section 3.3. The flaps maintain a fixed deflection angle relative to the vehicle's body throughout the entire flight and are remain passive.

2.6. Software Requirements

To answer the research question a reentry simulator is developed, which calculates the trajectory and dynamics of the reference vehicle. Given the resource constrains at such an early stage of the development of the reusable upper stage software simulation of the reentry is the most practical way at determining the flight characteristics. In this section the requirements for the aerodynamic coefficient generator and the reentry simulator are established, which ensures the tools functions as required. The software tool consists of the actual reentry simulator and the aerodynamic coefficients generator. The requirements for each part is listed separately.

2.6.1. Aerodynamic Coefficients Generator Requirements

The aerodynamic coefficients generator use the geometry of any reentry vehicle and produces the resulting aerodynamic coefficients as function of angle of attack, Mach number, and altitude. The focus of this projects is on the feasibility of a reusable upper stage in terms of stability and control during reentry and descent. Hence, determination and analysis of the aerodynamics of several vehicle configurations must be quick and straight forward to set-up, such that a range of different heat shield shapes and vehicle configurations can be evaluated. Set-up and execution time is therefore an important requirement for the aerodynamic coefficient generator in this project.

AC 1 The aerodynamic coefficients generator shall determine the aerodynamic coefficients of a ballistic reentry vehicle at all desired Mach numbers, altitudes, and angles of attack.

AC 2 The execution time of the aerodynamic coefficients generator shall be less then 60 s for one vehicle configuration.

AC 3 The aerodynamic coefficients generator shall have a quick and user friendly set-up process, such that the set-up time is less than 6 hours for a given vehicle configuration.

AC 4 The aerodynamic coefficients generator shall be capable of evaluating the aerodynamics of typical reentry vehicle and upper stage geometries.

AC 5 The average error in the aerodynamic coefficients calculated by the aerodynamic coefficients generator within the Mach number range relevant for reentry shall be less then 20%.

2.6.2. Reentry Simulator Requirements

The requirements for the reentry simulator are defined with the intent to verify that its output are an accurate representation of reentry trajectories and attitude dynamics. Furthermore, the large number of runs necessary for a meaningful dispersion analysis within a practical time frame requires a fast execution time per simulation. The requirements are therefore mainly based around these goals in addition to requirements addressing the utility of the tool, such as the import of the output files of the aerodynamic coefficients generator. The requirement for the reentry simulator are:

RS 1 The reentry simulator shall determine the trajectory of a reentry vehicle from entry interface to a desired terminal velocity.

RS 2 The position error in the output of the reentry dynamics simulator due to simplifications and numerical integration shall be less than 100 m within 300 s of flight time.

RS 3 The execution time of one simulation run shall not exceed 30 seconds.

RS 4 The reentry simulator shall generate an output file containing arrays of the state and condition of the vehicle and environment throughout the flight, such that the computed trajectory can be reconstructed, inspected, and analyzed.

RS 5 The reentry simulation tool shall include a guidance and control module capable of delivering the reentry vehicle to within 5 km of the designated target latitude and longitude when reaching the desired final velocity if the target is within range. If not it shall minimize the distance between the terminal point and the target.

RS 6 The reentry simulator shall be capable of importing the Missile DATCOM output file for006.dat and use the aerodynamic coefficients it contains in the simulation.

RS 7 The reentry simulator shall import an input file in which the initial conditions and properties of the vehicle and environment are specified.

3

Flight Dynamics

In Chapter 2 the shape and configurations of the reference upper stages are derived. To determine and analyze the flight of such a vehicle in space and through the atmosphere a set of equation of motion for its translation and rotation dynamics are derived. First the relevant reference frames and coordinates are described in Section 3.1. The re-entry environment and corresponding mathematical models are described in Section 3.2. In Section 3.3 the equations, methods, and tools used to determine the aerodynamics of the vehicle are discussed. The mass and mass distribution of the vehicle is derived in Section 3.4. Finally, in Section 3.5 the equations of motion are established, which are used in the simulation of the reentry of the upper stage.

3.1. Reference Frames and State Variables

The motion of any object in space can only be quantified relative to a agreed upon reference frame. Without a reference frame a velocity vector, for example, can take any arbitrary value depending on the location and motion of the observer. In this section all reference frames and coordinates systems relevant for modeling a re-entry are presented and described.

3.1.1. Reference Frame Definition

Reference frames are generally divided into two types, inertial and non-inertial reference frames. This is an important distinction, since inertial reference frames are themselves at rest or in linear motion and therefore exert no virtual force or moment on an object tracked with respect to that frame. Non-inertial reference frame on the other hand are accelerating or rotating reference frames, which can induce apparent forces and moments on bodies if that body is observed with respect to that frame. Equations of motion defined within non-inertial reference frames require additional terms to account for the acceleration of the frame. In the following paragraphs reference frames are described that are relevant for studying the motion of a reentry vehicle (Mulder et al., 2011).

Earth-centered inertial frame (I) The Earth-centered inertial reference frame is a pseudo-inertial reference frame due to the fact that is actually not truly inertial, because Earth is moving around the sun in an orbit and is therefore accelerating. However, the curvature of Earth's orbital path has a negligible influence on the motion of vehicle operating within a small fraction of Earth's orbital period. It can therefore be assumed inertial for those applications (Tapley et al., 2004).

One version of such a reference frame is the *J2000* reference frame. Its center is fixed to the center of Earth. its X-axis passes through the Earth's mean equator and points to the vernal equinox at $12:00$ Terrestrial Time (TT) on the 1^{st} of January 2000. The Z-axis is perpendicular to the X-axis and points through the geographic north pole. The Y-axis completes the coordinate frame in accordance with the right hand rule. A exact time is specified for this coordinate frame to remove any ambiguity caused by Earth's motion since then, such as, for example, the precession of Earth's spin axis. Such motion causes the parameters used to define the reference frame to not be valid anymore at any other time. However, the temporal discrepancies are very small and can be neglected for the purpose of reentry simulations (Mulder et al., 2011; Tapley et al., 2004).

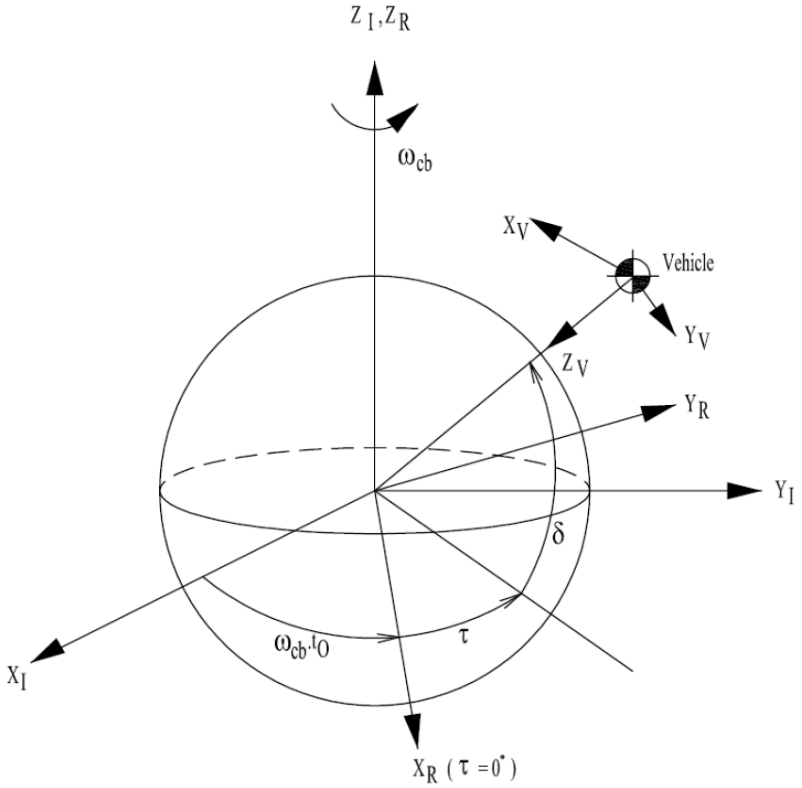

Figure 3.1: Relation between the Earth-centered inertial, Earth-centered fixed, and vehicle-carried vertical frame (Mooij, 2015).

Earth-centered fixed frame (R) The Earth-centered fixed reference frame ,also called rotating frame, differs from the inertial frame in the way that it is fixed to the Earth's surface and rotates with it. It is therefore not an inertial reference frame and has to be treated this way in the equations of motion. It's origin is fixed to the Earth's center of mass and its X-axis passes through the equator at the Greenwich meridian. The Z-axis points through the Earth's geographic north pole and the Y-axis completes the coordinate system also according to the right-hand rule (Tapley et al., 2004).

Vehicle-carried vertical frame (V) The vehicle carried vertical frame is a reference frame attached to the center of mass of the vehicle. This reference frame has the X-Y plane perpendicular to the local horizon and the Z-axis is pointing straight down towards the center of the Earth. The X-axis is pointing north and the y-axis is pointing east, again completing the right handed coordinate system (Mooij, 2015).

Figure 3.1 shows the relation between the Earth-centered inertial, Earth-centered fixed, and vehicle-carried vertical frame together with the corresponding transformation angles.

Vehicle-carried body-fixed frame (B) The vehicle-carried body reference frame is also attached to the vehicles center of mass but is rotation is also fixed to the body of the vehicle. This reference frame is used to define the orientation of the vehicle with respect to any other reference frame.

The X, Y, and Z-axis can be defined arbitrarily by the designer or user of the frame, since each vehicle and simulation can vary in form, function, or goal. Manufacturer often base their axis definition on flight direction, thrust direction, antenna pointing direction or other practical consideration (Mooij, 1994). For this study the body frame is centered at the center of mass of the vehicle. The X-axis passes through the center of the heat shield into the direction of flight. The Z-axis is aligned up and the Y-axis completes the right handed frame but, since the upper stage is rotationally symmetric, the definition of which side is up is arbitrary. Note that the definition of the body frame as used in the simulator is different from the frame used in Missile DATCOM, which has its furthest point at the front/tip of the

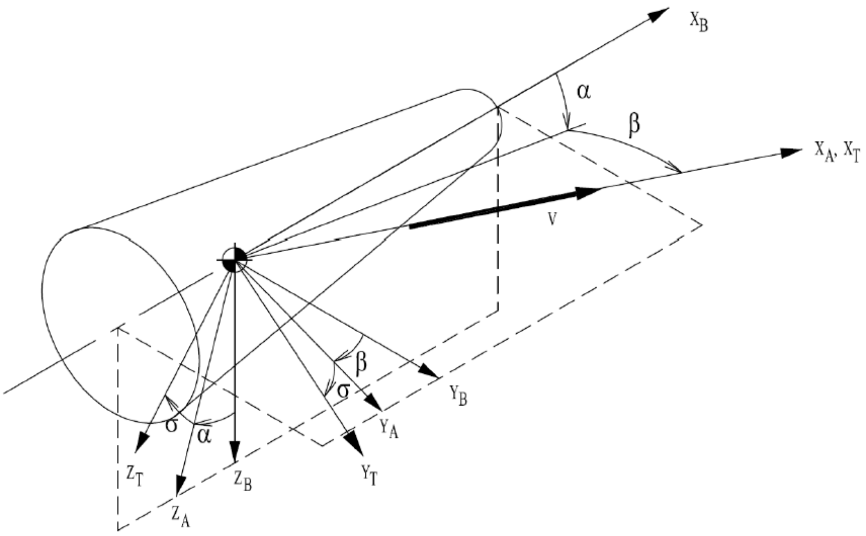

Figure 3.2: Relation between the Vehicle-carried body, aerodynamic, and trajectory frame (Mooij, 2015).

vehicle (Rosema et al., 2011). The same reference frame as used in Missile DATCOM is used in Figure 2.10 to define the location of each contour point.

Vehicle-carried aerodynamic frame (A) The aerodynamic forces acting on the vehicle are typically defined with respect to the aerodynamic frame with the origin fixed to the vehicle. The X-axis of this frame is pointing into the direction of the free stream velocity, the Y-axis passes though the X-Y plane of the body frame and the Z-axis is perpendicular to the X and Y-axis according to the right hand rule (Mooij, 1994).

Vehicle-carried trajectory frame (T) The vehicle-carried trajectory frame is a reference frame similar to the aerodynamic frame but with the notable difference that the Y-axis is always parallel to the local horizontal plane. The transformation from the trajectory frame to the aerodynamic frame can be done by adding the bank angle rotation to the trajectory frame (Mooij, 1994). The relation between the body frame, aerodynamic frame, and the trajectory frame is shown in Figure 3.2.

3.1.2. State Variables

The state of the vehicle in the context of flight dynamics can be described using a number of different sets of variables. In this report two types of coordinate systems are used to describe the position and translation of the vehicle, spherical and Cartesian coordinates. Keplerian elements are also commonly used to describe the translation dynamics of spacecraft but are typically used for trajectories outside of atmospheres and are not as useful for atmospheric flight (Wakker, 2010).

A different set of variables is required to define the orientation of the vehicle with respect to a reference frame. One obvious choice for this are euler angles, which quantify the angular distance of the vehicle with respect to a reference axis but come with a singularity in the kinematics. Alternatives to euler angles exist, such as quaternions, which offer a singularity free kinematics at the cost of a fourth variable. Other types of attitude state variables, such as Rodrigues parameters, attempt to reduce the number of elements in the attitude state back to three. However, Rodrigues parameters reintroduce a singularity at $180°$ instead of $90°$ for the euler angles, which is an improvement but can not provide the same robustness as quaternions. Overall given the benefits and the widespread use of quaternions in attitude dynamics and control system analysis, using them as attitude state variables is the most practical and robust option.

Cartesian Coordinates Cartesian coordinates consist of the X, Y, and Z components representing the three dimensions of space. Cartesian coordinates can be used in combination with any reference frame discussed previously to define the location and motion of a point within that frame. The conversion between reference frames is a matter of simple multiplication between the transformation matrix and any given Cartesian vector. In addition they are also intuitive to use. For example, at any point in time to find the velocity of an object relative to another object the inertial velocity vectors of both simply have to be subtracted (Polyanin and Manzhirov, 2007).

Cartesian coordinates are also very convenient to use as state variables for determining the forces acting on the vehicle. Both the equation for the gravitational and aerodynamic force vector yields them in Cartesian coordinates. Finally, one significant advantage of Cartesian coordinates is that they do not suffer from singularities, which makes them ideal as basis for numerical integration and manipulation. However, while numerically robust they are less intuitive to interpret.

The coordinates used as state variables in the simulation are defined within the Earth-centered inertial frame to eliminate the need to take apparent forces into account in the calculations. The position vector of the vehicle is represented by the variable **r** with its derivative $\dot{\mathbf{r}}$ being the velocity vector and the second derivative $\ddot{\mathbf{r}}$ representing the acceleration vector. The vector **r** consists of the components:

$$\mathbf{r}_I = \begin{pmatrix} x \\ y \\ z \end{pmatrix}_I \tag{3.1}$$

Spherical Coordinates While the Cartesian coordinates described in the previous paragraph is sufficient to define the state of the vehicle, different types of auxiliary coordinates are required to calculate the forces acting on the vehicle. For example, the angle of attack and side-slip angle are required to determine the correct set of aerodynamic coefficient for the current point in the trajectory, which in turn determines the aerodynamic forces acting on the vehicle. Furthermore, certain other coordinates are generally preferred over Cartesian coordinates for the interpretation of the results, since humans can, for example, more easily understand latitudes, longitudes, and altitudes than X, Y, and Z coordinates. They are therefore also useful in the visualization and discussion of the results.

One such alternative to Cartesian coordinates are spherical coordinates, where instead of X, Y, and Z coordinate the three dimensions are given in azimuth, which is the angle between the X-Z plane to the line of sight from the origin to the point, the elevation angle, which is the angle between the X-Y plane and that line, and the distance of the point from the origin (Stewart, 2008).

One example is the aforementioned geographic coordinates latitude δ, longitude τ and radius from Earth's center r. It is generally preferred over Cartesian coordinates for terrestrial applications, since it gives a more intuitive picture of a specific point on a sphere such as Earth.

These coordinates are defined in the rotating frame, since latitude and longitude positions are relative to a fixed point on the Earth's surface. Cartesian coordinates $\mathbf{r}_R$ of a point given in the rotating reference frame can be transformed into the spherical coordinates δ, τ, and r using (Mulder et al., 2011):.

$$\text{given} \quad \mathbf{r}_R = \begin{pmatrix} x \\ y \\ z \end{pmatrix}_R$$

$$\delta = \arcsin\left(\frac{r_z}{\sqrt{r_x^2 + r_y^2 + r_z^2}}\right) \tag{3.2}$$

$$\tau = \arctan\left(\frac{r_y}{r_x}\right) \tag{3.3}$$

$$r = \sqrt{x^2 + y^2 + z^2} \tag{3.4}$$

The range of δ and τ is defined per convention as[1]:

---

[1] Note that the longitude angle τ defined from $-\pi$ to π while the $\mathrm{arctan}()$-function in virtually all computer libraries works only within the range $-\frac{\pi}{2}$ to $\frac{\pi}{2}$. For cases were a range from $-\pi$ to π is required the $\mathrm{atan2}()$-function has to be used, which checks the sign of the numerator and denominator individually and selects the correct quadrant. This is also true for any of the following angles calculated using $\tan()$ while having limits defined as larger than from $-\frac{\pi}{2}$ to $\frac{\pi}{2}$.

$$-\pi \leq \tau < \pi$$
$$-\frac{\pi}{2} \leq \delta \leq \frac{\pi}{2}$$

Attitude State Variables The attitude of a spacecraft is quantified with a separate set of state variables. The most common type of variables used to describe the orientation of one reference frame with respect to any other reference frame are Euler angles.

A set of Euler angles consist of three angles, which specify the magnitude of three consecutive rotations of the initial frame around one of its three axis to arrive at the final frame. Each rotation after the rotation around the first axis has to be done in the current intermediate frame. This means there are 12 possible ways to perform reference frame transformations. Applying the same rotations in a different sequence results in different final frame. Hence it is important to stay consistent in the transformation sequence (Mulder et al., 2011).

One of the most common axis-rotation sequence in aerospace is the 3-2-1 sequence, which states that the rotation around the Z-axis is performed first, followed by a rotation around the Y-axis and, finally, a rotation around the X-axis (Mooij, 2015; Mulder et al., 2011). This sequence is also used in the simulation and throughout this document. More details on frame transformations are given in Subsection 3.1.3.

The attitude dynamics of the vehicle is defined with respect to the inertial frame. The Euler angles used as state variables for the vehicles attitude with respect to the inertial frame are called roll φ, pitch θ, and yaw ψ. They give an intuitive description of the attitude state of the vehicle but have a significant disadvantage when used for rigid-body attitude dynamics. The kinematic equation relating the three angular rates p, q, and r of the vehicle in the body frame to the attitude angle rates of the body frame with respect to the inertial frame $\dot{\varphi}$, $\dot{\theta}$, and $\dot{\psi}$ always contain points of singularity, interdependent of the sequence (Mulder et al., 2011).

In case of a 3-2-1 rotation sequence a singularity would occur at $90°$ pitch. In physical terms at a pitch of $90°$ both the roll and yaw axis would align and effectively define the same rotation leaving the system with only two degrees-of-freedom. This phenomena is called gimbal lock and is inevitable due to the fact that each subsequent rotation is performed in the intermediate frame.

An alternative way of representing orientation in space are quaternions. They do not suffer from singularities, since they are based on a different principle than Euler angles. Quaternions are based on the idea that any change in orientation can be achieved by a single rotation around one rotation axis vector. This so-called Euler axis is a unit vector and expressed as (Kuipers, 2002):

$$\mathbf{e} = \begin{pmatrix} e_x \\ e_y \\ e_z \end{pmatrix} \tag{3.5}$$

In addition to the Euler axis the magnitude of the rotation θ, also called the Euler angle, is required to completely describe any orientation. Using the Euler axis and Euler angle the quaternions for a given attitude can be calculated using (Kuipers, 2002):

$$\mathbf{q} = \begin{pmatrix} q_1 \\ q_2 \\ q_3 \\ q_4 \end{pmatrix} = \begin{pmatrix} e_x \sin\left(\frac{\theta}{2}\right) \\ e_y \sin\left(\frac{\theta}{2}\right) \\ e_z \sin\left(\frac{\theta}{2}\right) \\ \cos\left(\frac{\theta}{2}\right) \end{pmatrix} \tag{3.6}$$

The kinematic equation for the transformation of the angular rates of a vehicle in the body frame to the corresponding quaternion rates can be calculated the following equation (Kuipers, 2002).

$$\dot{\mathbf{q}} = \frac{1}{2} \begin{bmatrix} 0 & r & -q & p \\ -r & 0 & p & q \\ q & -p & 0 & r \\ -p & -q & -r & 0 \end{bmatrix} \begin{pmatrix} q_1 \\ q_2 \\ q_3 \\ q_4 \end{pmatrix} \tag{3.7}$$

Equation 3.7 shows that the singularities are eliminated at the cost of one extra element in the attitude state vector. Due to that advantage over Euler angles quaternions are used as the attitude state variable for the dynamics of the vehicle in the simulator.

In addition to quaternions different sets of Euler angles are used as auxiliary variables to, for example, calculate aerodynamic forces or express the output of the simulation with more intuitive variables. The aerodynamic coefficients C_L, C_D, and C_M required for the determination of the aerodynamic forces and moment acting on the vehicle are a function of angle of attack α, angle of side slip β, Mach number M, and Reynolds number Re. The angle of attack α and side slip β are Euler angles defining the vehicles orientation with respect to the aerodynamic frame.

To calculate α and β the elements of the transformation matrix given in Equation 3.8 can be used (Mulder et al., 2011), where γ is the flight-path angle, χ is the heading angle, and $\mathbf{T}_{Vb}$ is the transformation matrix from the body to the vertical frame. More on the derivation of transformation matrices is given in Subsection 3.1.3.

$$\mathbf{T}_{Xb} = \mathbf{T}_y(\gamma)\mathbf{T}_z(\chi)\mathbf{T}_{Vb} \tag{3.8}$$

The elements of that matrix are functions of the angle of attack, side-slip angle, and bank angle. The aerodynamic angles can be found using the following relations (Mulder et al., 2011).

$$\alpha = \arctan\left(\frac{\mathbf{T}_{Xb}(1,3)}{\mathbf{T}_{Xb}(1,1)}\right) \tag{3.9}$$

$$\beta = \arcsin\left(\mathbf{T}_{Xb}(1,2)\right) \tag{3.10}$$

The aerodynamic angles α and β are defined within the range:

$$-\pi \leq \alpha < \pi$$
$$-\frac{\pi}{2} \leq \beta \leq \frac{\pi}{2}$$

The bank angle quantifies the magnitude of the vehicle's rotation around the velocity vector and can also be calculated using the matrix given in Equation 3.8, as shown in the following equation (Mulder et al., 2011).

$$\sigma = -\arctan\left(\frac{\mathbf{T}_{Xb}(3,2)}{\mathbf{T}_{Xb}(2,2)}\right) \tag{3.11}$$

$$-\pi \leq \sigma < \pi$$

The bank angle is used to steer the vehicle by means of directing the lift force within the plane perpendicular to the velocity vector to a desired direction.

The flight-path angle γ and the heading angle χ mentioned earlier quantifies the angular separation of the velocity vector from the local horizon and the local north respectively. They are calculated using (Mulder et al., 2011):

$$\text{given} \quad \mathbf{V}_V = \begin{pmatrix} V_x \\ V_y \\ V_z \end{pmatrix}_V$$

$$\gamma = -\arcsin\left(\frac{V_z}{\sqrt{V_x^2 + V_y^2 + V_z^2}}\right) \tag{3.12}$$

$$\chi = \arctan\left(\frac{V_y}{V_x}\right) \tag{3.13}$$

The flight-path angle γ and the heading χ are defined with the range:

$$-\pi \leq \chi < \pi$$
$$-\frac{\pi}{2} \leq \gamma \leq \frac{\pi}{2}$$

3.1.3. Reference Frame Transformations

Given the reference frames introduced in 3.1 and the state and auxiliary coordinates in 3.1.2 it is now possible to transform any vector expressed in one reference frame to another reference frame. This can be done with the help of transformation matrices.

Simple transformation matrices are given in Equation 3.14, Equation, Equation 3.15, and Equation 3.16. They rotate any vector multiplied with them around the Z-axis by the angle θ_z, Y-axis by the angle θ_y, and X-axis by the angle θ_x respectively (Mulder et al., 2011).

$$\mathbf{T}_z = \begin{bmatrix} \cos\theta_z & \sin\theta_z & 0 \\ -\sin\theta_z & \cos\theta_z & 0 \\ 0 & 0 & 1 \end{bmatrix} \tag{3.14}$$

$$\mathbf{T}_y = \begin{bmatrix} \cos\theta_y & 0 & -\sin\theta_y \\ 0 & 1 & 0 \\ \sin\theta_y & 0 & \cos\theta_y \end{bmatrix} \tag{3.15}$$

$$\mathbf{T}_x = \begin{bmatrix} 1 & 0 & 0 \\ 0 & \cos\theta_x & \sin\theta_x \\ 0 & -\sin\theta_x & \cos\theta_x \end{bmatrix} \tag{3.16}$$

To be able to reorient a vector into any direction requires at least three consecutive rotations around the X-, Y-, or Z-axis using the matrices 3.14, 3.15, and 3.16. Any combination is allowed provided that a rotation around one axis is not performed twice. This offers 12 distinct rotation sequences in which a transformations can be performed. One rotation sequence must be chosen, since none of the 12 sequences are interchangeable and lead to different results (Mulder et al., 2011). The 3-2-1 sequence is a popular rotation sequence in the aerospace industry and the steps to obtain a matrix with that sequence are as follows.

To combine the three rotation matrices given in Equation 3.14-3.16 according to the 3-2-1 sequence they simply have to be matrix multiplied as shown in Equation 3.17 bearing in mind the correct sequence with the first rotation on the far right followed by each subsequent rotation on its left (Mulder et al., 2011).

$$\mathbf{T} = \mathbf{T}_x\mathbf{T}_y\mathbf{T}_z = \begin{bmatrix} 1 & 0 & 0 \\ 0 & \cos\theta_x & \sin\theta_x \\ 0 & -\sin\theta_x & \cos\theta_x \end{bmatrix} \begin{bmatrix} \cos\theta_y & 0 & -\sin\theta_y \\ 0 & 1 & 0 \\ \sin\theta_y & 0 & \cos\theta_y \end{bmatrix} \begin{bmatrix} \cos\theta_z & \sin\theta_z & 0 \\ -\sin\theta_z & \cos\theta_z & 0 \\ 0 & 0 & 1 \end{bmatrix} \tag{3.17}$$

This matrix can now be multiplied with any vector defined within the first frame to arrive at the representation of that vector in the second frame. To reverse that transformation the vector defined in the second frame has to be multiplied by the inverse of the transformation matrix. Since all transformation matrices are orthogonal an inversion can be achieved by simply transposing it (Mulder et al., 2011).

This method can be applied to transform vectors between the frames defined in 3.1 using the coordinates defined in 3.1.2 as input. In the following paragraphs all required transformation matrices are derived.

I-frame to R-frame As described earlier, the difference between the I-frame and R-frame is that the I-frame is fixed with respect to distant stars while the R-frame is fixed to the surface of the Earth. The Z-axis of both frames coincide and the R-frame rotates around it with respect to the I-frame.

The rate of rotation is defined by the rotation rate of the Earth ω_{cb} given in radians per second. Since the Earth rotates around its Z-axis continuously we get for the instantaneous transformation angle a value of $\omega_{cb}t$ with t being the time in seconds since the Greenwich meridian last crossed the vernal equinox. The transformation matrix from the I-frame to the R-frame is therefore given as (Mooij, 2015):

$$\mathbf{T}_{RI} = \begin{bmatrix} \cos\omega_{cb}t_0 & \sin\omega_{cb}t_0 & 0 \\ -\sin\omega_{cb}t_0 & \cos\omega_{cb}t_0 & 0 \\ 0 & 0 & 1 \end{bmatrix} \tag{3.18}$$

R-frame to V-frame The V-frame is characterized by the fact that its origin is vehicle-carried and its x-y plane is parallel to the surface of the Earth. The orientation of the V-frame with respect to the R-frame is therefore dependent on the location of the origin of the V-frame. Hence any transformation matrix requires the location of the vehicle, typically given in longitude τ and latitude δ, as input.

The transformation first revolves around the Z-axis by τ, and finally around the Y-axis of the intermediate frame by $\delta + 90°$. $90°$ are added to ensure the Z-axis rotates such that it points to the center of the Earth as per the definition of the V-frame given earlier. The transformation matrix from the R-frame to the V-frame is therefore (Mooij, 2015):

$$\mathbf{T}_{VR} = \begin{bmatrix} -\sin\delta & 0 & \cos\delta \\ 0 & 1 & 0 \\ -\cos\delta & 0 & -\sin\delta \end{bmatrix} \begin{bmatrix} \cos\tau & \sin\tau & 0 \\ -\sin\tau & \cos\tau & 0 \\ 0 & 0 & 1 \end{bmatrix} = \begin{bmatrix} -\sin\delta\cos\tau & -\sin\delta\sin\tau & \cos\delta \\ -\sin\tau & \cos\tau & 0 \\ -\cos\delta\cos\tau & -\cos\delta\sin\tau & -\sin\delta \end{bmatrix} \tag{3.19}$$

V-frame to T-frame The trajectory frame is aligned with the velocity vector of the vehicle and defined by the flight-path angle γ and heading angle χ, which define the vehicles orientation with respect to the local horizon. The transformation matrix can be derived as follows (Mooij, 2015).

$$\mathbf{T}_{TV} = \begin{bmatrix} \cos\gamma & 0 & \sin\gamma \\ 0 & 1 & 0 \\ -\sin\gamma & 0 & \cos\gamma \end{bmatrix} \begin{bmatrix} \cos\chi & \sin\chi & 0 \\ -\sin\chi & \cos\chi & 0 \\ 0 & 0 & 1 \end{bmatrix} = \begin{bmatrix} \cos\chi\cos\gamma & \sin\chi\cos\gamma & -\sin\gamma \\ -\sin\chi & \cos\chi & 0 \\ \cos\chi\sin\gamma & \sin\chi\sin\gamma & \cos\gamma \end{bmatrix} \tag{3.20}$$

T-frame to A-frame To transform a vector from the trajectory frame to the aerodynamic frame requires a single rotation around the X-axis by the bank angle σ as shown in the following matrix (Mooij, 2015).

$$\mathbf{T}_{AT} = \begin{bmatrix} 1 & 0 & 0 \\ 0 & \cos\sigma & \sin\sigma \\ 0 & -\sin\sigma & \cos\sigma \end{bmatrix} \tag{3.21}$$

A-frame to B-frame The transformation from the aerodynamic frame to the body frame requires the angle of attack α, and the side-slip angle β of the vehicle as input. They represent the orientation of the vehicle with respect to the incoming airflow vector and the transformation matrix is given as (Mooij, 2015):

$$\mathbf{T}_{BA} = \begin{bmatrix} \cos\beta & \sin\beta & 0 \\ -\sin\beta & \cos\beta & 0 \\ 0 & 0 & 1 \end{bmatrix} \begin{bmatrix} \cos\alpha & 0 & \sin\alpha \\ 0 & 1 & 0 \\ -\sin\alpha & 0 & \cos\alpha \end{bmatrix} = \begin{bmatrix} \cos\beta\cos\alpha & \sin\beta & \cos\beta\sin\alpha \\ -\sin\alpha\cos\alpha & \cos\beta & -\sin\beta\sin\alpha \\ -\sin\alpha & 0 & \cos\alpha \end{bmatrix} \tag{3.22}$$

B-frame to I-frame Finally, to transform a vector given in the body frame back to the inertial frame requires a transformation matrix with the attitude state variables as input. In this case quaternions are used as state variables, which do not use a sequence of rotations around each axis of the coordinate system as working principle. Hence the transformation matrix is derived differently as shown in the following expression (Kuipers, 2002; Mooij, 2015).

$$\mathbf{T}_{IB} = \begin{bmatrix} q_1^2 - q_2^2 - q_3^2 + q_4^2 & 2\left(q_1 q_2 - q_3 q_4\right) & 2\left(q_1 q_3 + q_2 q_4\right) \\ 2\left(q_1 q_2 + q_3 q_4\right) & -q_1^2 + q_2^2 - q_3^2 + q_4^2 & 2\left(q_2 q_3 - q_1 q_4\right) \\ 2\left(q_1 q_3 - q_2 q_4\right) & 2\left(q_2 q_3 + q_1 q_4\right) & -q_1^2 - q_2^2 + q_3^2 + q_4^2 \end{bmatrix} \tag{3.23}$$

3.2. Environment Model

In nature there is a large number of influences acting on the vehicle, such as the gravitational attraction from infinitely many celestial object, solar and cosmic radiation pressure, interactions with Earth's atmosphere, and the gravitational attraction of large lumps of mass inside Earth. However, in practice the effect of most of these phenomena are several magnitudes smaller than Earth gravitational attraction and are therefore neglected (Montenbruck and Gill, 2011). For reentry studies only the gravity and atmosphere of Earth have a significant influence on the result. In this section models for both are derived and discussed.

3.2.1. Gravitational Field Model

Outside the atmosphere the gravitational attraction of central body is the primary influence on the trajectory of a spacecraft. It is after the vehicle has re-entered the atmosphere and the dynamic pressure increases significantly when the aerodynamic forces surpass the gravitational pull. At altitudes relevant for re-entry studies Earth's gravitational attraction far surpasses the pull of any other celestial objects such as the Sun or Moon by several orders of magnitude, making their effects on the trajectory negligible (Montenbruck and Gill, 2011).

The central gravity field model, first derived by Newton, describes the gravitational force exerted by the point mass M on another point mass m and is can be calculated with:

$$\mathbf{F}_{grav,R} = \frac{GmM}{r^3}\mathbf{r} \tag{3.24}$$

Newton's law of gravitation assumes the mass M and m are concentrated in one point. However, the equation is also applicable to spherical shaped masses with uniform density provided that r remains larger than the radius of the sphere (Wakker, 2010).

Assuming Earth to be a perfect sphere and using the central field model given in Equation 3.24 is a good approximation and useful for preliminary analysis of spacecraft trajectories. However, it does not model the gravity field of the Earth entirely accurate. Due to Earth's irregular shape and inhomogeneous density distribution within it the actual gravity field of the Earth differs from the perfect central field model to a noticeable degree, depending on the application (Wakker, 2010).

Deviations from the central field model are described using so-called spherical harmonics, where each harmonic corresponds to a certain effect, which causes a disturbance from the central field model.

The most significant gravitational disturbance for low orbiting satellites and re-entry vehicles is the J_2 effect. This effect is caused by the fact that due to its rotation the Earth is flattened along the poles and bulges outwards around the equator. The total height difference between both locations is 20 km. This results in more mass being concentrated around the equator than at the poles, which effects the motion of satellites crossing the equator. The extra mass around the equator tends to accelerate any orbiting body towards it (Wertz et al., 2009).

For inclined orbits this results in an increase in inclination during approach of the equator, then a decrease in inclination when the equator has been passed. Overall the increase and decrease cancels out leaving the final inclination the same after each equator passage but the ascending and descending node shifts to the west at every passage of the equator (Wertz et al., 2009). For a re-entry vehicle this may result in a significant drift, especially in the exo-atmospheric portion of the flight compared to the pure central field model.

The disturbance acceleration caused by the J_2 is on the order of $10^{-5}\ \mathrm{km/s^2}$. The remaining J terms are orders of magnitude lover and have therefore a negligible effect on the motion of a re-entry vehicle given the short re-entry duration and the significantly larger forces due to the aerodynamics, and central gravity field (Montenbruck and Gill, 2011). The disturbance acceleration caused by the J_2 harmonic as function of the Cartesian position coordinates in the R-frame is given as:

$$\begin{pmatrix} a_x \\ a_y \\ a_z \end{pmatrix}_{J_2} = -\frac{3}{2}\mu J_2 \frac{R_E^2}{r^5} \begin{pmatrix} x\left(1-5\frac{z^2}{r^2}\right) \\ y\left(1-5\frac{z^2}{r^2}\right) \\ z\left(3-5\frac{z^2}{r^2}\right) \end{pmatrix} \tag{3.25}$$

Here r is the absolute distance of the vehicle from the center of the Earth, the variables x, y, and z are the Cartesian position vector of the vehicle in the R-frame.

The largest gravitational disturbance following the J_2 harmonic is the $J_{2,2}$ with an acceleration of the order of $10^{-7}\ \mathrm{km/s^2}$. Within a typical reentry time frame of $300 - 400$ s the change in velocity and position due to that disturbance is negligible. This simplification therefore does not violate the accuracy requirement for the simulation.

3.2.2. Atmosphere model

At sufficiently high velocities the aerodynamics forces become the most dominant influence on the trajectory of a vehicle, surpassing even the gravitational force. This fact is routinely demonstrated every day when large airplanes lift of from the ground with several thousand tons of cargo seemingly weightless as soon as they reach a certain speed.

This is especially true for re-entry vehicle, which usually experience aerodynamic accelerations multiple times higher than the gravitational pull of the Earth. Hence an good model Earth's atmosphere is a vital component of every good reentry simulator. However, given the chaotic variations in weather and temperature observed daily deriving an accurate model of the atmosphere is extremely difficult.

For this project two atmosphere models are used. For the reentry dynamics simulator the US 1976 Standard Atmosphere is used, which is a good approximation of an average atmosphere and included in the TU Delft Astrodynamics Toolbox (TUDAT). For the guidance algorithm the exponential atmosphere is used for faster calculation speed to quickly arrive at a guidance solution.

Exponential atmosphere The exponential atmosphere model is based on the assumption that the atmosphere has a constant temperature and is an ideal gas. Hence the pressure and density of the air at a certain altitude within this atmosphere model becomes a function of the mass of the ideal isothermal column of gas above the altitude of interest.

The benefits of this model are its quick calculation time, since it only consists of one analytic function no interpolation or look-up tables are required, which require much more computer resources. This makes it well suited for the computationally intensive guidance algorithm compared to any other semi-empirical atmosphere model.

Assuming the atmosphere is in hydrostatic equilibrium the derivative of the pressure with respect to altitude is given as (Mooij, 2015):

$$dp = \rho g dh \tag{3.26}$$

In this equation air pressure is a function of air density ρ and gravitational acceleration g, both of which are a function of altitude. Using Newtons equation for gravitational acceleration given in Equation 3.27, with μ being Earth's gravitational parameter and r being the distance from the center of the Earth, the gravitational acceleration at sea level and at 150 km altitude can be found to be $9.8203\ \mathrm{m/s^2}$ and $9.3737\ \mathrm{m/s^2}$ respectively.

$$g = \frac{\mu}{r^2} \tag{3.27}$$

This is a difference of less than 5% and, depending on the application, can be neglected for the sake of making g a constant g_0, which is equal to the gravitational acceleration at sea level (Mooij, 2015). This simplification, together with the assumption of an isothermal atmosphere allows for the derivation of an explicit equation for the density of the atmosphere as a function of altitude. The relationship between pressure and density in an ideal gas is governed by the following equations.

$$p = \rho RT \tag{3.28}$$

$$dp = d\rho RT \tag{3.29}$$

Equation 3.29 can be set equal to Equation 3.26 to eliminate the pressure variable and arrive at the expression:

$$d\rho RT = -\rho g_0 dh \tag{3.30}$$

This is then solved for the density terms as follows.

$$\frac{d\rho}{\rho} = -\frac{g_0}{RT} dh \tag{3.31}$$

Finally, integrating this equation yields:

$$ln\frac{\rho}{\rho_0} = -\frac{g_0}{RT} h \tag{3.32}$$

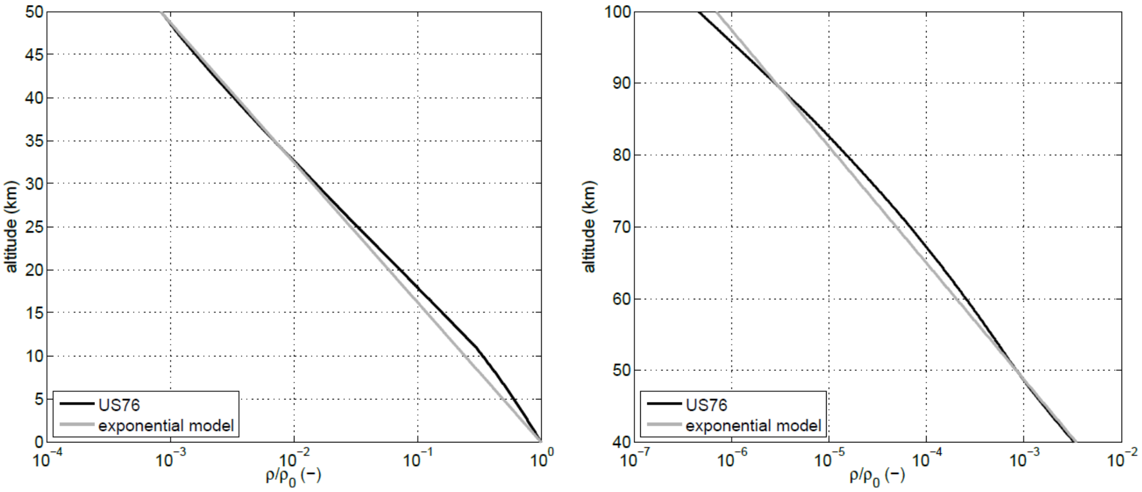

Figure 3.3: Difference in air density as a function of altitude on a logarithmic plot (Mooij, 2015).

By solving this equation for the density ρ one arrives at Equation 3.33 with ρ_0 being the reference density, usually set to the sea level average air pressure of $1.225\ \mathrm{kg/m^3}$, and H_s being the scale height with values that can range from $7,050$ km to $7,200$ Km and can be tuned to best match Earth's atmosphere. The temperature is usually set to 240 K (Mooij, 2015).

$$\rho = \rho_0^{-\frac{g_0 h}{RT}} = \rho_0^{-\frac{h}{H_s}} \tag{3.33}$$

The assumption of constant gravitational acceleration and air temperature introduces errors in favor of an explicit analytic expression for the density as a function of altitude. The air density with altitude given by the exponential atmosphere model is compared with the US 1976 standard atmosphere in Figure 3.3 (Mooij, 2015).

There the exponential atmosphere takes the form of a straight line as expected, since it is expressed as an exponential function while the more accurate US 1976 standard atmosphere is non-linear and deviates slightly from the line drawn by the exponential atmosphere. These deviations introduce significant errors in the simulation of the motion of a re-entry vehicle due to the sensitivity of uncontrolled atmospheric reentry to the air density.

While the slight deviations do produce errors in the guidance solutions, repeated execution of the guidance algorithm throughout the flight counteracts the discrepancy by appropriately changing the bank angle and steering against it (Lu, 2008). Due to that and the significant improvement in the execution time of the algorithm the exponential atmosphere model is used in the guidance algorithm.

US 1976 Standard Atmosphere The US 1976 standard atmosphere is a semi-empirical atmosphere model based on an empirically determined temperature profile of Earth's atmosphere as a function of altitude. The temperature profile is used to calculate more accurate values for density and pressure of the atmosphere as a function of altitude compared to the exponential atmosphere.

Seasonal and geographical temperature fluctuation introduce deviations from the static temperature profile at certain times and over specific regions around the globe, which makes this model loose some of its predictive capability for specific cases. Reference atmosphere models, such as the NRLMSISE-00 or COSPAR model, use extensive measurement data of the atmosphere to derive a model as function of altitude, location above Earth's surface, and time. This comes at the cost of a more computationally expensive model to use compared to the US Standard Atmosphere. Furthermore, given the early work on the upper stage, the exact mission date is undetermined. The temporal accuracy of the reference models is therefore only marginally useful at such an early stage of the vehicle's development. Averaging this model over time and position and making it a function of altitude only yields a standard atmosphere model similar to the US 1976 Standard Atmosphere. While the US 1976 Standard Atmosphere suffers from some inaccuracies at higher altitudes compared to newer models it yields a fairly accurate model of an average Earth atmosphere at mid-latitudes (Abby et al., 2010). This fact and the model's availability in TUDAT makes it the most practical choice. The temporal and spacial variations in the atmosphere are modeled by randomizing the output appropriately in the dispersion analysis.

The US 1976 model divides Earth's atmosphere into two sections, the first ranging from 0 km to 86 km and the second ranging from 86 km to 1000 km. The temperature profile for the lower part of the atmosphere is constructed out of a number of functions described in Table 3.1 (NOAA, 1976).

Subscript b [-]	**Geopotential Alt.** H_b [km]	**Temp.Gradient** $L_{M,b}$ [K/km]	**Form of T(h)** [-]	**Derived Temp.** $T_{M,b}$ [K]
0	0	-6.5	Linear	288.150
1	11	0.0	Linear	216.650
2	20	1.0	Linear	216.650
3	32	2.8	Linear	228.650
4	47	0.0	Linear	270.650
5	51	-2.8	Linear	270.650
6	71	-2.0	Linear	214.650
7	84.8520			186.946

Table 3.1: Linear function parameters of the US 1976 Standard Atmosphere for the altitude range of $0 - 86$ km (NOAA, 1976).

To compensate for the effect of the changing gravitational acceleration with altitude the geopotential altitude is introduced. The conversion between geometric altitude Z to geopotential altitude H is given as (NOAA, 1976):

$$Z = \frac{r_0 H}{\frac{g_0}{g_0'} r_0 - H} \tag{3.34}$$

Using the data in Table 3.1 a spline is created that can be used to calculate the temperature as a function of altitude. For the linear parts the following relation must be used.

$$T = T_b + L_{k,b}\,(H - H_b) \tag{3.35}$$

Furthermore the data given in Table 3.1 can be directly applied in Equation 3.36 and Equation 3.37 to calculate pressure and density at any given altitude for any layer in the atmosphere with a non-zero temperature gradient. Here the term M is the mean molecular weight of air and R^* is the universal gas constant (NOAA, 1976).

$$P = P_b \left[\frac{T_{M,b}}{T_b + L_b\,(H - H_b)}\right]^{\frac{g_0 M}{R^* L_b}} \tag{3.36}$$

$$\rho = \rho \left[\frac{T_b + L_b\,(H - H_b)}{T_{M,b}}\right]^{\left(-\frac{g_0 M}{R^* L_b}\right)-1} \tag{3.37}$$

For atmospheric layers with a zero temperature gradient the following two equations are to be used to determine the pressure and density respectively (NOAA, 1976).

$$P = P_b e^{\left[\frac{-g_0 M (H - H_b)}{R^* T_{M,b}}\right]} \tag{3.38}$$

$$\rho = \rho_b e^{\left[\frac{-g_0 M (H - H_b)}{R^* T_{M,b}}\right]} \tag{3.39}$$

For altitudes above 86 km and up to 1000 km a different set of functions are required. Given the more complex nature of the upper atmosphere an elliptical and an exponential function are introduced in addition to linear functions to produce a new temperature spline. The functions used to spline the temperature profile for the upper atmosphere are given in Table 3.2.

In this case geometric altitude is used as input variable again instead of the geopotential altitude. This is because the gradient in gravitational acceleration becomes negligible compared to the molecular dynamics of the air particles (NOAA, 1976).

Subscript b [-]	**Geometric Alt.** Z_b [km]	**Temp.Gradient** $L_{k,b}$ [K/km]	**Form of T(Z)** [-]	**Derived Temp.** T_b [K]
7	86	0.0	Linear	186.87
8	91		Eliptical	186.87
9	110	12.0	Linear	
10	120		Exponential	360.00
11	500			999.24
12	1000			1000.00

Table 3.2: Constants of the US 1976 Standard Atmosphere for the $86-1000$ km altitude range (NOAA, 1976).

Again for the linear sections of the temperature profile the temperature for any given altitude can be calculated with (NOAA, 1976):

$$T = T_b + L_{k,b}\,(Z - Z_b) \tag{3.40}$$

Layer 8, ranging from 91 km to 110 km, has an elliptical shape and the temperature there is therefore defined with Equation 3.41 where $T_c = 263.1905$ K, $A = -76.3232$ K and $a = -19.9429$ km. Those values are derived using the boundary conditions given by the values at the end of layer 8 and measured values of the beginning of layer 10 (NOAA, 1976).

$$T = T_c + A\left[1 - \left(\frac{Z - Z_b}{a}\right)^2\right]^{\frac{1}{2}} \tag{3.41}$$

Finally, the temperature for layer 10 is an exponential function of altitude and is defined in the following equation where $T_\infty = 1000$ K (NOAA, 1976).

$$T = T_\infty - (T_\infty - T_{10})\exp\left(-\lambda\xi\right) \tag{3.42}$$

The two coefficients λ and ξ are defined in as:

$$\lambda = \frac{L_{k,9}}{T_\infty - T_10} = 0.01875 \tag{3.43}$$

$$\xi = (Z - Z_{10})\,\frac{r_0 + Z_{10}}{r_0 + Z} \tag{3.44}$$

With these parameters substituted into Equation 3.42 the pressure at any altitude above 86 km can be calculated. Due to the low density and highly energetic particles the barometric equation does not hold anymore. For this case the pressure of the gas has to be calculated with the following equation on the basis of the total number density (NOAA, 1976).

$$P = \sum P_i = \sum n_i k T \tag{3.45}$$

Here the index i represents one type of molecule present in the gas mixture at a given altitude. The parameter k stands for the Bolzmann constant and T is the local temperature based on the spline mentioned earlier. The partial pressure of all types of gasses then needs to be summed up. With the pressure and the temperature the air density is calculated (NOAA, 1976).

Air-density variations Both the US 1976 Standard Atmosphere and the exponential model of the atmosphere are static models in which a unchanging temperature, pressure, and density over the entire Earth. However, the atmospheric condition can vary considerably as a function of the location on Earth, activity of the sun, or time.

This fact is important to take into account, since the aerodynamics of the reentry vehicle is directly dependent on the density and indirectly on the temperature of the atmosphere. Typical variations in the air density with altitude as predicted by the GRAM-95 model are shown in Figure 3.4 (Cheatwood, 1997).

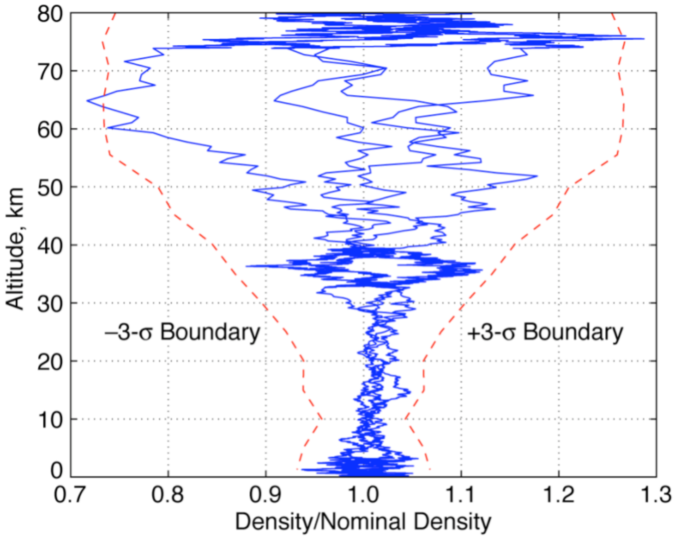

Figure 3.4: Density variation as function of altitude according to the GRAM-95 model (Cheatwood, 1997).

To understand the sensitivity and test the robustness of the reusable upper stage reentry to off-nominal conditions in the atmosphere the density and temperature are randomized in the dispersion analysis according to variations observed in nature. More specifically the density is randomized linearly by $\pm 10\%$ below an altitude of 30 km, by $\pm 20\%$ between 30 and 50 km, and by $\pm 30\%$ above 50 km. This increase in variation with altitude is meant to reflects the variation observed in nature as visible in Figure 3.4. The low density gas in the higher atmosphere is more sensitive to the variations in the radiation coming from the sun in contrast to the lower layers, where the high energy radiation is filtered out by the previous layers and strong convection results in a more stable conditions (Frieman et al., 1994).

3.3. Aerodynamic Model

The development of an accurate aerodynamic model without extensive experimental data is one of the most difficult problems in vehicle design and analysis. The interaction of air even with simple moving shapes can be very complex and often require significant computational resources to estimate to satisfying degree. Adding to that the often complex geometries and attitudes of the vehicle makes the derivation of any meaningful analytic equation for the aerodynamic forces acting on it impossible.

A classical way to determine the aerodynamic coefficients aside from flight testing the finished vehicle are windtunnel experiments of true-scale or sub-scale physical models. These experiments give reasonably accurate results within their range of operating velocities. However, they require a significant time and financial investment to set up and execute, which is not always available during preliminary design or small scale concept analysis such as this one.

Alternative ways based on mathematical laws and relations were developed to avoid expensive physical experiments. One of the first ideas came from Isaac Newton, who developed a theory based on the momentum transfer of moving air as they hit a wall. While his theory predicted the resulting forces poorly at low airspeeds it was later discovered that his theory predicted well the interactions observed at hypersonic airspeeds (Anderson, 1989; Vinh et al., 1980).

Finally, Navier-Stokes derived differential equations for Newtonian fluids, which are used to accurately simulate fluids in Computational-Fluid-Dynamics (CFD) tools on computers. While being the most accurate method to compute aerodynamic forces on a body CFD tools come with the disadvantage of being complex to use and require relatively high computational power (Abevnayaka and Agon, 2013). The set-up requires a complete 3D-mesh of the vehicle’s geometry, which is time consuming and violates the time constraint given in the requirements for the aerodynamic coefficient generator. The execution time for these tools also typically far exceed the practical limit set in the requirements. This method is therefore not an option for this project and would not allow the broad analysis of the aerodynamics of several different upper stage configurations.

For the analysis of the vehicle described in this report a combination of semi-empirical coefficient generator called Missile DATCOM and the modified Newton method is used. It features a straightforward and user-friendly input method, which allows for a quick set-up of less then 1 hour. The tool also executes one run within a few seconds. These specification satisfy the time requirement set for the aerodynamic coefficient generator. The accuracy of the tool is not specified and is therefore investigated here in Section 5.3.

While Missile DATCOM is well suited to provide the aerodynamic coefficients for the cylindrical body of the upper stage, its geometry-input method does not allow for the kind of flaps used for one of the upper stage configurations discussed in Section 2.5.2. The contribution of the flaps to the dynamics of the vehicle are therefore determined using the Newton method. In the following subsections both methods are described.

3.3.1. Semi-Empirical Coefficient Generator (Missile DATCOM)

The investment required for practical experiments as well as tedious and computationally expensive CFD simulation lead to the development of a semi-empirical coefficient calculator called Missile DATCOM. This tool satisfies the need for a quick aerodynamic coefficient calculator for preliminary design and concept evaluation of missiles and projectiles. This is achieved by combining a large set of experimental data and derive empirical relations from them (Rosema et al., 2011). The tool is semi-empirical, because at increasing Mach numbers empirical relations are gradually replaced by the modified Newton method due to the little amount of experimental data at hypersonic airspeeds and the good agreement of the Newton method with reality.

The tool makes use of the fact that missiles and projectiles usually have an axis along which the object can be constructed as body-of-rotation. The geometry of the vehicle can be imputed by specifying a point along that axis and a corresponding radius from it. In addition there are methods to modify the shape even more to an extent but those options are not required for this purpose, since both the Apollo capsule and the upper stage can be entirely constructed as body-of-rotation (Rosema et al., 2011).

As mentioned in the previous chapter a limitation of DATCOM is that it does not take shadowing into account. Hence constructing a shape that has parts in the slipstream of a previous vehicle section would result in erroneous data. The nozzle of the upper stage as drawn in Figure 2.10 is therefore left out of the input for Missile DATCOM.

With the vehicle geometry and a list of angle of attacks, Mach numbers, and altitudes Missile DATCOM generates an output file with a list of aerodynamic coefficients C_D, C_L, and C_M (Rosema et al., 2011). Aerodynamic coefficients are dimensionless parameters that can be used to calculate the drag D, lift L, and pitch moment M as shown in Equation 3.46, 3.47, and 3.48 respectively. Here $\bar{q}$ stands for dynamic pressure, S_{ref} for the reference surface, and L_{ref} for the reference length used to calculate the coefficients (Anderson, 2016).

$$D = C_D \bar{q} S_{ref} \tag{3.46}$$

$$L = C_L \bar{q} S_{ref} \tag{3.47}$$

$$M = C_M \bar{q} S_{ref} L_{ref} \tag{3.48}$$

The dynamic pressure is the pressure generated on the vehicle by the momentum of the incoming airflow and is therefore a function of both the magnitude of the airspeed V_∞ and the density of the air ρ:

$$\bar{q} = \frac{1}{2}\rho_\infty V_\infty^2 \tag{3.49}$$

Note that the side-slip angle and any shift in center of mass are also accepted as input by Missile DATCOM, but are not used and an absolute angle of attack is assumed. The result of a center of mass located on the line of symmetry of the vehicle is a symmetric C_L-α curve. Also the lateral force coefficient C_S and yaw moment coefficient C_N are zero in the Missile DATCOM output file due to the zero side-slip angle. Mapping the total angle of attack to the true angle of attack and side-slip angle as well as adding the effect of the vertical shift in the center of mass is done in the simulator with the relevant equations given in Section 3.5.

Using the concept of body-of-rotation as input method is a powerful way to input cylindrical or conical shapes into DATCOM compared to the mesh generation required as input for most CFD tools. However, using the contour of a body-of-rotation as such lacks the means to add details, such as flaps. Since Missile DATCOM is designed for Missiles, which are often equipped with fins for steering and stability, the option exist to add them to the vehicle. However, they are facing the flow edge-on and cannot be set-up face-on as required for the purpose of a re-entry vehicle. Missile DATCOM is therefore just used for the cylindrical body. The aerodynamic forces and moments from the flaps are calculated and added separately using the modified Newton method.

3.3.2. Modified Newton Method

The Newton method is based around the idea that the incoming inert, non-interacting air particles impart momentum on the vehicle as they collide with the surface of the body. Assuming the surface is inclined with respect to the airstream the momentum transferred is only the one normal to the wall. The net pressure acting on the wall facing the airflow is therefore equal to the reduction of the dynamic pressure due to the impact on the wall. An expression for the net pressure on an inclined wall with the inclination angle θ is (Anderson, 1989):

$$\Delta p = p - p_\infty = \rho_\infty V_\infty^2 \sin^2 \theta \tag{3.50}$$

To derive the pressure coefficient per unit area of wall the expression given in Equation 3.50 is made dimensionless as shown in the following equation (Anderson, 1989).

$$C_p = \frac{\rho_\infty V_\infty^2 \sin^2 \theta}{\frac{1}{2}\rho_\infty V_\infty^2} = C_{p,max} \sin^2 \theta = 2 \sin^2 \theta \tag{3.51}$$

This expression was first derived by Newton and gives a reasonable approximation of the pressure coefficient at an inclined surface in a hypersonic airflow. However, it indirectly assumes that the heat capacity ratio $\gamma = 1$. This results in $C_{p,max} = 2$. To get an even more accurate representation for that coefficient within Earth's atmosphere $C_{p,max}$ has to be calculated using the correct γ for air, which is 1.4. The more appropriate $C_{p,max}$ based on the correct heat capacity ratio for air can be found with (Anderson, 1989):

$$C_{p,max} = \left[\frac{(\gamma+1)^2}{4\gamma}\right]^{\frac{\gamma}{\gamma-1}} \left[\frac{4}{\gamma+1}\right] \tag{3.52}$$

Now for a flat plate the pressure coefficient C_p is equal to the normal force coefficient C_n, which acts perpendicular to the plate's surface.

To arrive at the aerodynamic force coefficients for a body of arbitrary shape Equation 3.51 is integrated over the entire windward surface. At the hypersonic velocities in which the Newton method yields reasonably good solutions the surface in the slip stream is in vacuum and therefore has a C_p of 0 (Anderson, 1989).

This method is used in Missile DATCOM at high hypersonic airspeeds where sufficient empirical data becomes increasingly rare (Rosema et al., 2011). It is also used here to estimate the aerodynamic force produced by body flaps on the upper stage.

For the flaps the assumption is made that a flap can be represented by a flat plate set at a desired deflection angle with respect to the vehicle. This means no force is acting along the wall and only a normal force is acting perpendicular to the surface when the plate is set at an angle of attack. The normal force can be calculated using the Newton method and the surface area of the flap S_{flap} as shown in the following equation.

$$F_N = C_{p,max} \sin^2 \theta \; \bar{q} S_{flap} \tag{3.53}$$

The inclination angle of the flat plate with respect to the incoming airflow θ as the plate is attached to the upper stage can be calculated for the bottom and top flap the following two equations respectively.

$$\theta_{bottom} = \delta_{flap} + \alpha \tag{3.54}$$

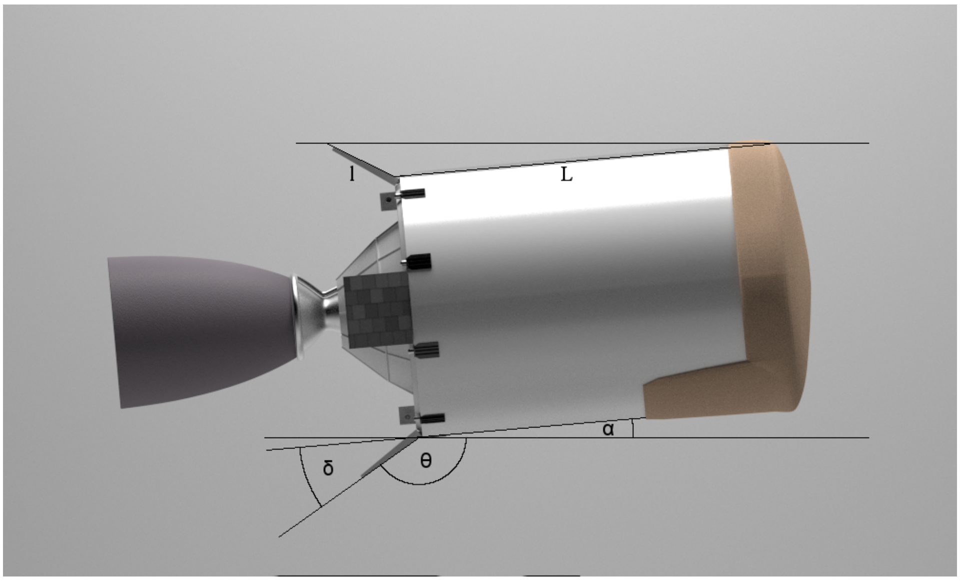

Figure 3.5: Reusable upper stage with flaps and illustrations of the angle of attack α and the flap deflection angle δ used to arrive at the flap inclination angle θ. Those, together with the stage tank length L, are also used to calculate the length of the flap in the shadow l.

$$\theta_{top} = \delta_{flap} - \alpha \tag{3.55}$$

Note that the top flap at positive angle of attack and the bottom flap at a negative angle of attack are in the shadow of the stage from the incoming airflow. The effect of that shadowing can be estimated by calculating the effective reduction in flap surface. The key parameters are illustrated in Figure 3.5 where the variable l, which is the length of the shadow, multiplied with the width of the flap yields the surface of the shadow S' on the flap. This surface is subtracted from the available surface area to arrive at the area immersed the airflow.

For a positive net surface area the normal force can now be calculated in a similar way as shown in Equation 3.53 with the available surface area instead of the total flap area resulting in the equation:

$$F_N = C_{p,max} \sin^2 \theta \; \bar{q} \left(S_{flap} - S' \right) \tag{3.56}$$

For a zero or negative net surface the flap creates no aerodynamic force. To combine the aerodynamic forces acting on the flaps and the aerodynamic forces created by the main body each flap force is transformed into the vehicle body frame using Equation 3.57 for the contribution in the axial direction parallel to the X-axis and Equation 3.58 for the radial direction along the Z-axis for the top and bottom flap.

$$F_{axial} = F_N \sin \delta_{flap} \tag{3.57}$$

$$F_{radial} = F_N \cos \delta_{flap} \tag{3.58}$$

The axial component F_{axial} is always pointing to the back of the vehicle for both the top and bottom flap. The radial components of the top and bottom flap point towards the X-axis of the body frame and have therefore opposite signs with respect to each other. The flap forces now in the body frame can further be transformed into the aerodynamic frame to finally add them to the aerodynamic forces acting on the body as calculated in Equation 3.46, and Equation 3.47. The contribution of the flaps to the pitching moment is calculated using:

$$\mathbf{M}_{flap} = \begin{pmatrix} x_{com} - x_{flap} \\ 0 \\ z_{com} - z_{flap} \end{pmatrix} \times \begin{pmatrix} F_{axial} \\ 0 \\ F_{radial} \end{pmatrix} = \left(\mathbf{x}_{com} - \mathbf{x}_{flap,B} \right) \times \mathbf{F}_{flap,B} \tag{3.59}$$

A second pair of flaps is added along the lateral axis of the vehicle to stabilize the yaw axis using the same principle as described here for the pitch axis.

While these equations model the basic mechanism behind the forces generated by flaps they leave out tangential forces generated by pointing the flaps with a side-slip into the airflow. The pair of flaps stabilizing the pitch axis, for example, are oriented at a side-slip angle with respect to the flow when the entire vehicle is in a side slip. The same is true for the pair of flaps stabilizing the yaw of the vehicle when the vehicle is at an angle of attack. The magnitude of these secondary deflections during flight is at most equal to the current angle of attack or side-slip angle of the vehicle. Hence in both cases they generate a relatively small destabilizing moment compared to the stabilizing moment generated by the opposite pair of flaps, which are deflected by a comparatively large $20°$ to sufficiently stabilize the upper stage. Assuming a secondary deflection of $5°$ and using Equation 3.51 yields a pressure coefficient fraction of 4.26% of the main pressure coefficient resulting from the $20°$ deflection. This aspect is therefore neglected to avoid the introduction of overly complex relations at such an early stage of concept analysis.

3.3.3. Aerothermodynamics

The goal of reentry is to dissipate the kinetic and potential energy stored in the orbiting vehicle entirely and complete that process right when the vehicle reaches a desired position on Earth. This energy is dissipated as heat for the most part into the atmosphere. A fraction of the heat is conducted to the vehicle. Although this fraction is relatively small compared to the heat stored in the air it still represents a dangerous heat load for the vehicle without a thermal protection system (TPS) (Mooij, 2015).

Most reentry vehicles use an ablative heat shield. This type of heat shield absorbs most of that energy by reacting with the hot air and carrying the remaining heat in the resulting reaction products away from the vehicle. The chemical reaction absorbs so much of the incoming energy that the underlying layers remain cool. Other types of heat shields relay on heat resistant ceramics or carbon-carbon to protect the vehicle structure and payload from the heat.

Heat generation varies along the heat shield surface and is usually the highest at the stagnation point where the surface is perpendicular to the flow and the air comes to a dead stop. While total heat generation is the highest at the stagnation point in some cases the heat convection to the vehicle can be larger at other points on the surface. This is often the case for reentry vehicle with complex shapes allowing, for example, for reattachment of the box shock to the surface (Dirkx, 2011). However, in this preliminary analysis the maximum heat rate is assumed to be at the stagnation point.

The heat rate per surface area in $\mathrm{W/m^2}$ can be calculated using the semi-empirical relation given in Equation 3.60, where the constants N_1 and N_2 for a laminar flow are given as 0.5 and 3.15 respectively (Saraf et al., 2004).

$$q_s = k\rho^{N_1}V^{N_2} \tag{3.60}$$

The constant k is calculated with the following relation.

$$k = \frac{1.83 \cdot 10^{-4}}{\sqrt{R_n}}\left(1 - \frac{T_w}{T_{aw}}\right) \tag{3.61}$$

The parameter R_n is the radius of the heat shield at the stagnation point, T_w is the wall temperature, and T_{aw} is the adiabatic wall temperature. As a first-order approximation a cold wall assumption is used, which simplifies T_w/T_{aw} to be approximately 0 (Saraf et al., 2004).

The total heat load per unit of surface area throughout the reentry at the stagnation point is now calculated by integrating Equation 3.60 over time:

$$Q_s = \int_{t_0}^{t_f} q_s dt \tag{3.62}$$

For ablative heat shields the heat flux given in Equation 3.60 is a good indicator for the relative ablation rate at any given time during the reentry. The total heat load integrated over the entire flight ultimately determines the thickness and consequently the mass of the heat shield (Putz and Bartlett, 1973).

3.4. Vehicle Mass Model

To determine the flight and angular dynamics of the upper stage requires knowledge about its mass and the moment of inertia. However, for existing vehicles such numbers are rarely publicly available. The reusable upper stage concept dealt with in this study is based on an existing vehicle, the Falcon 9 upper stage, with some modifications to allow for reentry. To derive a set of mass and moment of inertia numbers they have to be estimated.

The total mass of the vehicle is estimated to be between 3900 kg and 4500 kg (Blau, 2016; Kyle, 2015). However, for the angular dynamics not only the total mass of the vehicle is important, but the internal mass distribution as well, which determines the location of the center of mass and the moment of inertia. In the following two subsections an attempt is made to derive quantitative estimates for these variables. For that estimate mass for critical systems such as electronics and avionics is assumed to be contained in the structural elements listed in Figure 2.6.

3.4.1. Vehicle Mass and Center of Mass Location

The center of mass is a property of lumped masses consisting of several smaller mass elements. The center of mass is a point, where all the mass of an object is focused and around which it rotates if a moment is applied. Forces that act through the center of mass do not create a moment and those that do not create a moment proportional to the distance from the center of mass times the forces (Hibbeler, 2016). Hence, the location of the center of mass of the vehicle is an important point for the analysis of the rotational dynamics of an object.

The derivation of the center of mass requires the separation of the upper stage into mass elements and their location in the vehicle's frame of reference. Making the mass elements infinitely small is impractical for a preliminary analysis and is left for future studies when CAD drawings or a prototype exists. In this study the vehicle is split into simple shaped mass elements to simplify the derivation, while still providing a reasonable estimate for the location of the center of mass.

Constraints used for the estimation are the dimensions shown in Figure 2.8 with some modifications. The payload adapter is removed assuming it would be jettisoned after deployment of the satellite to reveal the heat shield. However, the total length of the vehicle of 11.09 m is maintained by moving the first bulkhead ahead and thereby somewhat approximating the stretching done in the latest upgrades to the Falcon 9.

To maintain the same volume ratio between the liquid oxygen and RP-1 the shared bulkhead is moved proportionally ahead as well. The heat shield is attached directly onto the first bulkhead similar to how the heat shield of the Apollo capsule is attached right against the bottom wall of the crew cabin.

The semi-circle of small Helium or RCS tanks inside the forward propellant tank are moved closer to the first bulkhead to be at the same location relative to it as before. The ring of tanks is reduced to a semi-circle of tanks to induce the shift in the center of mass and achieve a passive trim attitude. This mass asymmetry could be designed into the upper stage or introduced during flight by consuming Helium and/or RCS propellant from just one side of the vehicle for the desired effect. The individual mass elements are listed in Table 3.3. In the bottom row values for the mass and center-of-mass location for the entire vehicle is given. The mass uncertainty for the entire vehicle of 5% given in the last row is applied to the resulting total mass in addition to the uncertainty applied to each individual component.

Each mass element i of N total number of elements with the mass m_i and its location (x_i, y_i, z_i) with respect to the rest of the vehicle is used in Equation 3.63, Equation 3.64, and Equation 3.65 to find the coordinates of the center of mass of the entire upper stage (Hibbeler, 2016). The y-coordinate is 0 for every element, since the vehicle is symmetric along the X-Z plane and is therefore not shown in Table 3.3.

$$x_{cm} = \frac{\sum_{i=1}^{N} m_i x_i}{\sum_{i=1}^{N} m_i} \tag{3.63}$$

$$y_{cm} = \frac{\sum_{i=1}^{N} m_i y_i}{\sum_{i=1}^{N} m_i} \tag{3.64}$$

$$z_{cm} = \frac{\sum_{i=1}^{N} m_i z_i}{\sum_{i=1}^{N} m_i} \tag{3.65}$$

Element	Mass	Mass uncertainty	Long. location(X)	Vert. location(Z)
Heat shield	662.87 kg	±50%	0.05 m	0 m
Bulkhead 1	284.06 kg	±20%	0.1 m	0 m
Tank cylinder	858.78 kg	±20%	2.77 m	0 m
6× RCS/Helium tanks	137.13 kg	±20%	1.01 m	−0.7694 m
Bulkhead 2	284.06 kg	±20%	3.45 m	0 m
Bulkhead 3	284.06 kg	±20%	5.54 m	0 m
Thrust Structure	683.38 kg	±20%	6.223 m	0 m
Engine	599.51 kg	±0%	7.39 m	0 m
Nozzle	116.36 kg	±20%	6.926 m	0 m
Vehicle	**4595.89 kg**	±5%	**3.332 m**	**−0.138 m**

Table 3.3: List of mass elements used to derive an estimate for the location of the vehicle's center of mass.

The reference point of each element used to place them inside the upper stage is each elements respective center of mass, which is the geometric middle or center point for most parts listed in Table 3.3 assuming a uniform density.

The only exceptions are the engine nozzle and the thrust structure, which have no intuitive center of mass location. However, by approximating them as hollow frustums we can find their respective total mass and the location of their center of mass along their longitudinal axis with Equation 3.66 and Equation 3.67, respectively (Diaz et al., 2005). Here the density ρ is again assumed constant and uniform along the entire body and the body of rotation is closed/complete around the X-axis.

$$m = \pi\rho \int_{x_o}^{x_f} \left[f_2(x)^2 - f_1(x)^2 \right] dx \tag{3.66}$$

$$X_{cm} = \frac{\pi\rho}{M} \int_{x_o}^{x_f} \left[f_2(x)^2 - f_1(x)^2 \right] x dx \tag{3.67}$$

The body is defined by the enclosed space between the functions $f_1(x)$ and $f_2(x)$, where $f_2(x) > f_1(x)$ (Diaz et al., 2005). For a frustum the two functions are simple linear functions.

These methods are used to make a preliminary estimate of the dimensions and mass of each mass element given the lack of data on the typical mass distribution within upper stages with the exception of the heat shield. The heat shield mass is estimated by using the relation apparent in Figure 3.6.

In this figure the mass of the thermal protection system is plotted against the total heat load experienced by several reentry vehicle with a trend line plotted through them. The sample used to arrive at the relation represent a wide variety of reentry vehicle in terms of size with the two largest spacecraft being the Apollo capsule and the Mars Viking lander.

Using the relation given in the plot a heat shield mass fraction of 15% is found for the same total heat load per unit area as experienced by the Apollo capsule during reentry from the moon. Since the upper stage is expected to return from a geostationary transfer orbit the entry velocity for the upper stage is close to a return from the moon and therefore a similar mass fraction is assumed as a first approximation. Given the large variations found in Figure 3.6 an uncertainty in the mass of the TPS of ±50% is assumed compared to the ±20% for the remaining structure.

The location of the center of mass of the baseline vehicle is given in the last row of Table 3.3. The variations applied to the individual mass elements translate into a range of different values for the center of mass, which are used for the sensitivity and dispersion analysis. The resulting center of mass locations are plotted into Figure 2.10. An additional ±5% linear dispersion is added to the total mass and center of mass to account for additional uncertainties in the overall design.

3.4.2. Moment of Inertia

The moment of inertia is another property of bodies with non-zero spacial dimensions, which is used to relate its angular momentum to its angular velocity, similar to how the mass of an object relates a force to the resulting acceleration. Hence, it is important to now this property of the vehicle to accurately model and study its rotational dynamics. A general expression for the mass moment of inertia J of an arbitrary body is shown in Equation 3.68 with r being the distance of the small mass element dm from

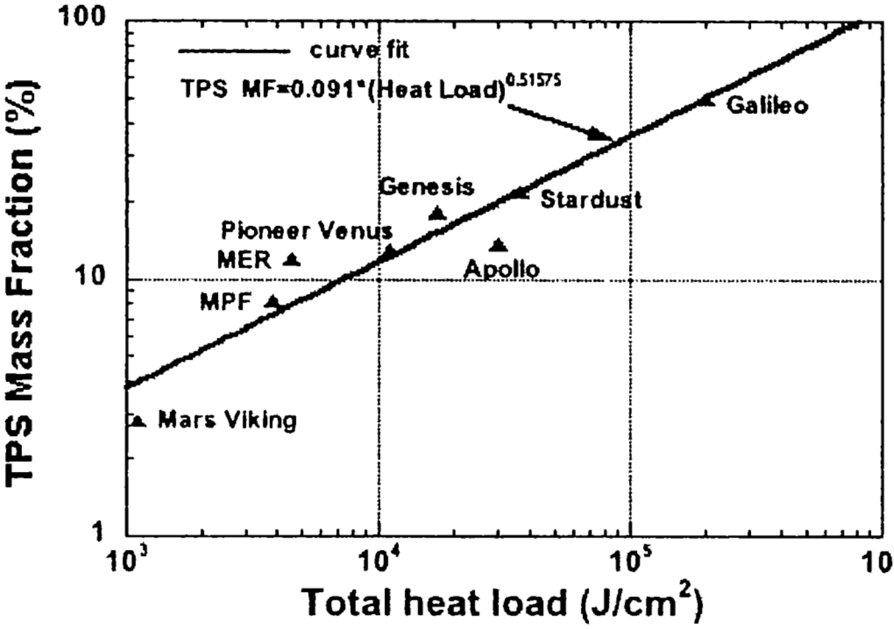

Figure 3.6: TPS mass fraction of a variety of reentry vehicles as function of total heat load (Venkatapathy, 2004).

a given axis of reference around which the moment of inertia is calculated. The integral is integrated over the entire mass m (Hibbeler, 2009).

$$J = \int_m r^2 dm \tag{3.68}$$

Integrating Equation 3.68 for a hollow cylinder with negligible thickness as assumed for the tank along the longitudinal axis yields:

$$J_{cyl,x} = mr^2 \tag{3.69}$$

This is a straightforward example as the distance of the tank wall from the longitudinal axis r stays constant and the mass element dm is assumed to be concentrated at that point. However, calculating the moment of inertia for the Y-axis and Z-axis for the same hollow thin-walled cylinder is more complicated to determine. For many simple shapes expressions for the moment of inertia around each of the three axis are available in literature and can be used to aproximate the mass elements in Table 3.3 (Hibbeler, 2016). The only exception is the hollow frustum, which is the shape used to approximate the thrust cone and nozzle of the upper stage.

For a thin solid disk the moment of inertia around the X-axis pointing through the center of the disk perpendicular to the flat surface using Equation 3.70, around the other two axis with Equation 3.71. Here m is the mass of the disk and R is the radius.

$$J_{disk,x} = \frac{mR^2}{2} \tag{3.70}$$

$$J_{disk,y} = J_{disk,z} = \frac{mR^2}{4} \tag{3.71}$$

For a thin hollow cylinder the moment of inertia along the X-axis pointing longitudinally through the cylinder is given in Equation 3.69 and around the remaining axis in Equation 3.72, where l is the length of the cylinder.

$$J_{cyl,y} = J_{cyl,z} = \frac{m}{12}\left(6R^2 + l^2\right) \tag{3.72}$$

Solid spheres are assumed for the spherical tanks as they may contain propellant or gas. The moment of inertia of a solid sphere along all axis is given as:

$$J_{sph,x} = J_{sph,y} = J_{sph,z} = \frac{2}{5}mR^2 \tag{3.73}$$

Similar to Equation 3.66 and Equation 3.67 a powerful method exists to also calculate the moment of inertia for cylindrical objects using the principle of body-of-rotation. Assuming a uniform density across the entirely closed fully rotated body-of-rotation around the X-axis, and a constant length with x_o being the starting coordinate and x_f the final coordinate of an object its moment of inertia around all three axis can be calculated with Equation 3.74 and Equation 3.75 (Diaz et al., 2005). The functions $f_1\,(x)$ and $f_2\,(x)$ are the same as those used for calculating the mass and center of mass for both the paraboloid and frustum.

$$J_x = \frac{\pi\rho}{2}\int_{x_o}^{x_f}\left[f_2\,(x)^4 - f_1\,(x)^4\right]dx \tag{3.74}$$

$$J_y = J_z = \frac{1}{2}J_x + \pi\rho\int_{x_o}^{x_f} x^2\left[f_2\,(x)^2 - f_1\,(x)^2\right]dx \tag{3.75}$$

The moment of inertia matrix for each individual mass element is then build as shown here:

$$\mathbf{J}_i = \begin{bmatrix} J_{x,i} & 0 & 0 \\ 0 & J_{y,i} & 0 \\ 0 & 0 & J_{z,i} \end{bmatrix} \tag{3.76}$$

To add up all the moments of inertia and arrive at the final figure for the reusable upper stage the individual mass moments of inertia have to be transformed from the axis around which they are calculated to the center of mass of the entire vehicle. This is done by using the parallel axis theorem expressed by Equation 3.77 with $\mathbf{J}_i$ being the individual moment of inertia matrix of an element as calculated earlier, m_i being its mass, and $\mathbf{r}$ being the position vector from the center of mass of the vehicle to the point around which the moment of inertia is calculated, with r being its absolute value and $\mathbf{I}$ stands for the identity matrix (Hibbeler, 2016).

$$\mathbf{J}_{cm} = \mathbf{J}_i + m_i\left(r_i^2\mathbf{I} - \mathbf{r}_i\mathbf{r}_i^T\right) \tag{3.77}$$

Using the theory described here and the mass elements defined in Table 3.3 the resulting moment of inertia matrix for the baseline vehicle turns out to be:

$$\mathbf{J}_{Stage} = \begin{bmatrix} 8489.23 & 0 & 1470.07 \\ 0 & 41200.74 & 0 \\ 1470.07 & 0 & 41596.5 \end{bmatrix} \mathrm{kg}\cdot\mathrm{m}^2 \tag{3.78}$$

The mass uncertainty on each mass element introduced in Table 3.3 is also used to randomize the moment of inertia of each element. An additional 5% linear uncertainty is applied to the vehicle moment of inertia tensor given in Equation 3.78. Given the lack of any publicly-available reference moment of inertia for the Falcon 9 upper stage or similar vehicle the randomization is intended to cover a range of possible values and increase confidence in the results.

3.5. Equations of Motion

In the previous sections of this chapter the reference frames, state variables and the environment, in which the vehicle flies, are discussed. The different elements are now combined into a set of equations of motion, which if properly propagate can predict the state of the vehicle in time. To achieve this all force, position, and motion vectors have to first be expressed in the same reference frame. The different forces can then simply be added up and converted to an acceleration vector as experienced by the vehicle.

Using Missile DATCOM the aerodynamic coefficients are determined as a function of total angle of attack. To split up the absolute lift coefficient into the lateral force and lift coefficient components

Equation 3.80 and Equation 3.81 are used. The drag coefficient as calculated by Missile DATCOM is the same as the actual drag (Mooij, 1998).

$$C_D = C_{D,abs} \tag{3.79}$$

$$C_S = \frac{\cos\alpha \sin\beta}{\sin\alpha_{abs}} C_{L,abs} \tag{3.80}$$

$$C_L = \frac{\sin\alpha}{\sin\alpha_{abs}} C_{L,abs} \tag{3.81}$$

The absolute pitch moment coefficient can also be split up into the corresponding pitch moment and yaw moment coefficient with the following relations (Mooij, 1998).

$$C_l = 0 \tag{3.82}$$

$$C_M = \frac{\sin\alpha \cos\beta}{\sin\alpha_{abs}} C_{M,abs} \tag{3.83}$$

$$C_N = -\frac{\sin\beta}{\sin\alpha_{abs}} C_{M,abs} \tag{3.84}$$

As stated earlier the axis-symmetric shape of the upper stage generates no roll moment. The roll moment coefficient C_l is therefore 0.

The aerodynamic moment derivatives are also governed by a set of coefficients, namely C_{l_p}, C_{m_q}, and C_{n_r}. They are a function of the angular rates of the vehicle and are responsible for dampening any angular rates over time. These are typically very small and turn out to be negligible compared to the much stronger dampening effect of the rapidly changing air density. They are therefore also assumed to be equal to 0.

Using the aerodynamic force and moment coefficients the aerodynamic forces and moment can be calculated with:

$$\mathbf{F}_{aero,A} = \bar{q} S_{ref} \begin{pmatrix} C_D \\ C_S \\ C_L \end{pmatrix} \tag{3.85}$$

$$\mathbf{M}_{aero,B} = \bar{q} S_{ref} L_{ref} \begin{pmatrix} 0 \\ C_M \\ C_N \end{pmatrix} \tag{3.86}$$

As stated earlier the aerodynamic forces and moments provided by Missile DATCOM are with respect to a completely symmetric upper stage. However, a vertical shift in the center of mass Δz_{cm} is introduced to trim the vehicle around a non-zero angle of attack. This results in an additional moment caused by the combined aerodynamic force vector's line of action not passing through the center of mass of the vehicle at an angle of attack of $0°$. The goal of combining the two moment vectors is a stable equilibrium at a non-zero angle of attack. The moment generated by the shift in the center of mass is calculated using:

$$\mathbf{M}_{cm,B} = \begin{pmatrix} \Delta x_{cm} \\ 0 \\ \Delta z_{cm} \end{pmatrix} \times \mathbf{T}_{BA} \mathbf{F}_{aero,A} \tag{3.87}$$

The resultant total moment acting on the vehicle $\mathbf{M}$ is calculated from the combined aerodynamic moment produced by the vehicle fuselage, the flaps as well as the control moment generated by the attitude control system.

$$\mathbf{M} = \mathbf{M}_{aero,B} + \mathbf{M}_{flap,B} + \mathbf{M}_{control,B} \tag{3.88}$$

To calculate the angular acceleration the total moment, its current angular velocity vector $\boldsymbol{\omega}$, and the moment of inertia matrix $\mathbf{J}$ as determined in Section 3.4 are used in the so-called Euler equation of motion for the dynamics of rigid bodies given as (Sidi, 1997; Wie, 2008)

$$\dot{\boldsymbol{\omega}} = \begin{pmatrix} \dot{p} \\ \dot{q} \\ \dot{r} \end{pmatrix} = \mathbf{J}^{-1} \left(\mathbf{M} - \boldsymbol{\omega} \times \mathbf{J} \cdot \boldsymbol{\omega} \right) \tag{3.89}$$

Since the vehicle's attitude state is given in quaternions their rate of change is a function of the vehicle's current attitude and angular velocity (Mooij, 2015; Wie, 2008):

$$\dot{\mathbf{q}} = \frac{1}{2} \begin{bmatrix} -q_1 & -q_2 & -q_3 \\ q_0 & -q_3 & q_2 \\ q_3 & q_0 & -q_1 \\ -q_2 & q_1 & q_0 \end{bmatrix} \boldsymbol{\omega} \tag{3.90}$$

Finally, the equation of motion governing the translation of the vehicle is a function of the aerodynamic and gravitational forces acting on the vehicle. To combine them into a single resultant vector all elements need to be united into the same reference frame, which in this case is the inertial reference frame. The acceleration of the vehicle can therefore be calculated using Equation 3.91, where $\mathbf{T}_{YX}$ is a general form transformation matrices present in Equation 3.91 from the generic X-frame to the Y-frame. The subscripts of the force vectors $\mathbf{F}$ denote the type of force followed by the frame in which it is defined.

$$m\dot{\mathbf{V}}_I = \mathbf{T}_{IA}\mathbf{F}_{aero,A} + \mathbf{T}_{IB}\mathbf{F}_{flap,B} + \mathbf{T}_{IR}\mathbf{F}_{grav,B} \tag{3.91}$$

The rate of position is the velocity of the vehicle and is therefore simply:

$$\dot{\mathbf{R}}_I = \mathbf{V}_I \tag{3.92}$$

4

Guidance & Control

To facilitate recovery and a quick turn-around time it is necessary for a reusable upper stage to control its descent and steer towards a designated landing site. To perform such a guided and controlled return a on-board guidance and control algorithm is implemented.

The guidance algorithm determines the path by using the current state of the vehicle and finding a trajectory that will take it to a desired final state (Mooij, 2015). The independent variable used to generate the range of possible trajectories is the bank angle (Lu, 2008). The resulting optimal bank angle for reaching the target is then used as input by the controller to change the attitude of the vehicle accordingly. The guidance and control methods used are described in this chapter starting with the guidance algorithm in Section 4.1. The controller is described in Section 4.2.

4.1. Guidance Algorithm

The goal of the guidance algorithm is to find an input for the controller that would deliver the vehicle to the target location. Several methods have been developed over the decades since the first manned orbital flights. The method used in the simulator is based on a simplified model of the system integrated forward in time to predict its final state at a desired terminal condition (Lu, 2008). This guidance algorithm has never been used due to its reliance on computational power to integrate the vehicles state. However, improvements in miniaturization, efficiency, and capability of modern computers could make this type of numerical guidance algorithm a viable option.

In contrast a different method for reentry guidance used onboard the Apollo capsule exists, which is based on drag acceleration experienced by the vehicle for tracking and follows a reference acceleration profile (Harpold and Graves, 1979). Tracking the vehicle's acceleration has several benefit, such as no need for an aerodynamic model of the vehicle on board the guidance computer which is prone to uncertainties (Lu, 2008). It also only requires an accelerometer and does not require a complex navigation system or integration of Inertial Measurement Unit (IMU) data to determine the current state of the vehicle for error correction. However, it relies on a drag acceleration profile stored on board as reference, which is optimized for a specific return trajectory and vehicle.

The Predictor-Corrector guidance therefore offers greater flexibility in terms of landing locations and vehicle type (Lu, 2008). This makes this type of guidance algorithm favorable for the simulator given the goal of analyzing the feasibility of a reusable upper stage in different configurations and conditions. The disadvantages only apply to the practical application of this method as onboard guidance, where the state cannot be directly observed and a powerful sufficiently computer system may not be available.

The interface between the guidance and the control is the desired bank angle variable. The bank angle can be used to control the range by increasing or decreasing the magnitude of the vertical component of the lift vector and thereby either lift the vehicle higher or dipping it deeper into the denser parts of the atmosphere. The altitude in turn effects the drag magnitude of the vehicle. Cross-range can be controlled by reversing the bank angle sign when the vehicle has sheered off-course by a predefined heading error (Mooij, 2015). The range prediction and lateral guidance algorithm are discussed in more details in the following two subsections.

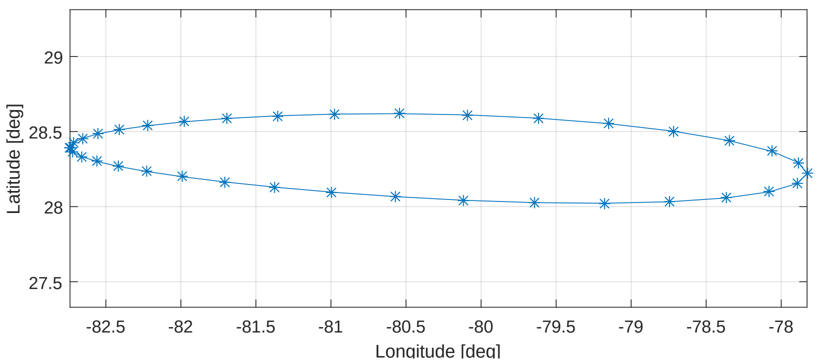

Figure 4.1: Terminal ellipse of the reusable upper stage returning from low Earth orbit.

4.1.1. Range Prediction

The range prediction and targeting algorithm uses a model of the vehicle and environment to simulate the trajectory forward in time. This model is used together with an optimization algorithm to seek a bank angle magnitude, which minimizes the distance between the terminal point of the trajectory and the target point. A variation of this algorithm is proposed by Ping Lu as a guidance method for the Orion reentry capsule (Lu, 2008).

The set of equations given in Equations 4.1 to 4.3 are used by Lu to model the translation of the vehicle in a two-dimensional space.

$$\frac{ds}{de} = -\frac{\cos\gamma}{rD} \tag{4.1}$$

$$\frac{dr}{de} = -\frac{\sin\gamma}{D} \tag{4.2}$$

$$\frac{d\gamma}{de} = -\frac{1}{DV^2}\left[L\cos\sigma + \left(V^2 - \frac{1}{r}\right)\left(\frac{\cos\gamma}{r}\right)\right] \tag{4.3}$$

These equations yield the traveled distance s, the distance between the vehicle and the center of the Earth r, and the flight path angle γ as a derivative of an energy-like parameter e. The variable e combines the altitude and velocity of the vehicle as shown in Equation 4.4 to reduce the number of equations from four to three (Lu, 2008).

$$e = \frac{1}{r} - \frac{V^2}{2} \tag{4.4}$$

The differential equations are integrated to determine the trajectory of the vehicle. To ensure the vehicle arrives at the target when the terminal conditions are met the distance between the initial position and the final position s_f if the reentry trajectory has to be equal to the distance between the initial position and the target s_t. The value s_f can be influenced by the bank angle σ, since a bank angle smaller than $90°$ lifts the vehicle up while a larger bank angle pushes the vehicle down into the atmosphere. Finding the required bank angle for the downrange distance $s_f = s_t$ becomes a matter of determining the root of the function $f(\sigma) = s_f - s_t = 0$, provided $s_f = s_t$ is achievable within the possible bank angle range of $0° \leq \sigma \leq 180°$ (Lu, 2008).

This method assumes that the downrange travel distance is directly dependent on the bank angle magnitude. This can be verified by performing a series of reentry simulations with a number of different constant bank angle and observing the resulting final position. The resulting terminal ellipse is given in Figure 4.1 and indeed confirms this relationship.

To further improve the robustness of this method and ensure sufficient margins at the end of the flight a linear bank angle profile can be used instead of a constant one. This is done by fixing the final bank angle above the target site at $60°$ and the initial bank angle is found, such that the predicted downrange distance matches the distance to the target (Lu, 2008).

While the set of equations proposed by Lu and shown in Equations 4.1 - 4.3 are simplified to the essential and easy to implement they do not provide sufficient flexibility for tuning and analysis of the effect of certain elements in the vehicle's environment on the guidance accuracy. For that and practical reasons the implementation of the vehicle dynamics described in Chapter 3 as implemented for the simulator is also used for the guidance. Notable differences are the use of the exponential atmosphere model. a set of constant reference aerodynamic coefficients instead of the Missile DATCOM data, and drops the simulation of the angular motion of the vehicle to speed up the execution time of the guidance algorithm.

The new dynamics modified for the guidance are then used in an optimization algorithm, which performs the following steps every time the guidance is executed:

1. The maximum and minimum possible distance is determined by assuming that the maximum possible range irrespective of any constraints is achieved with a constant bank angle of $0°$. A minimum range is assumed to be achievable at a constant bank angle of $180°$. The minimum and maximum range, denoted in the diagram as S_1 and S_0, are determined to ensure the target location is within range. If it is the algorithm continues to the next step.

   Otherwise the algorithm commands a bank angle of $0°$ to pull the vehicle up if it undershoots or a bank angle of $180°$ for a pull down in case of an overshoot. This is done to minimize the miss-distance. Some margins are applied to the bank angle limits at which the pull up or pull down is performed even if the target can be reached to gain some room for later in the flight.

2. If the target is within achievable range a bank angle is found, which results in a range-to-go equal to the range-to-target. The root-finding algorithm used is the bisection method. While it is not the best performing root-finding algorithm it is a robust method and requires no bank-angle derivatives of the range-to-go compared to faster algorithms, such as the Newton-Raphson method.

3. The algorithm is stopped when the difference between the target and final position of the vehicle is sufficiently small. The final bank angle is outputted and used by the control as commanded bank angle.

A flow chart illustrating the guidance algorithm is shown in Figure 4.2.

4.1.2. Lateral Guidance

Contrary to aircraft, which head to the desired coordinates above the surface in a straight line and control the range with the engines, the heading guidance for an unpowered reentry vehicle is achieved by setting appropriate heading error boundaries and initiating bank reversals when these boundaries are crossed. This approach is necessary, since the range is also controlled by the magnitude of the bank angle, which forces the vehicle into a turn. A plot of the bank angle as function of time is shown in Figure 4.3, where bank reversals are used to control the descent (Lu, 2008). The magnitude of the bank angle is determined by the downrange guidance while the sign controls the heading error.

The heading error is the error between the current heading of the vehicle and the direction of the target and is calculated using (Mooij, 2015):

$$\chi_T = \arctan\left[\frac{\sin(\tau_T - \tau)\sin(\frac{\pi}{2} - \delta_T)}{\cos(\frac{\pi}{2} - \delta_T)\sin(\frac{\pi}{2} - \delta) - \cos(\tau_T - \tau)\cos(\frac{\pi}{2} - \delta)\sin(\frac{\pi}{2} - \delta_T)}\right] \tag{4.5}$$

The reversal boundaries, which initiate the bank reversals, depend on the cross range capability of the vehicle. For vehicle with a low lift-to-drag ratio tight boundaries are required to recover from the misalignment in time.

4.2. Attitude Controller

The trajectory and final position of the upper stage is controlled using the attitude of the vehicle, which determines the direction of the aerodynamic forces as described in Chapter 3. More specifically the bank angle is used to point the lift vector into the desired direction (Mooij, 2015). In this section the attitude control algorithm used for the upper stage is discussed.

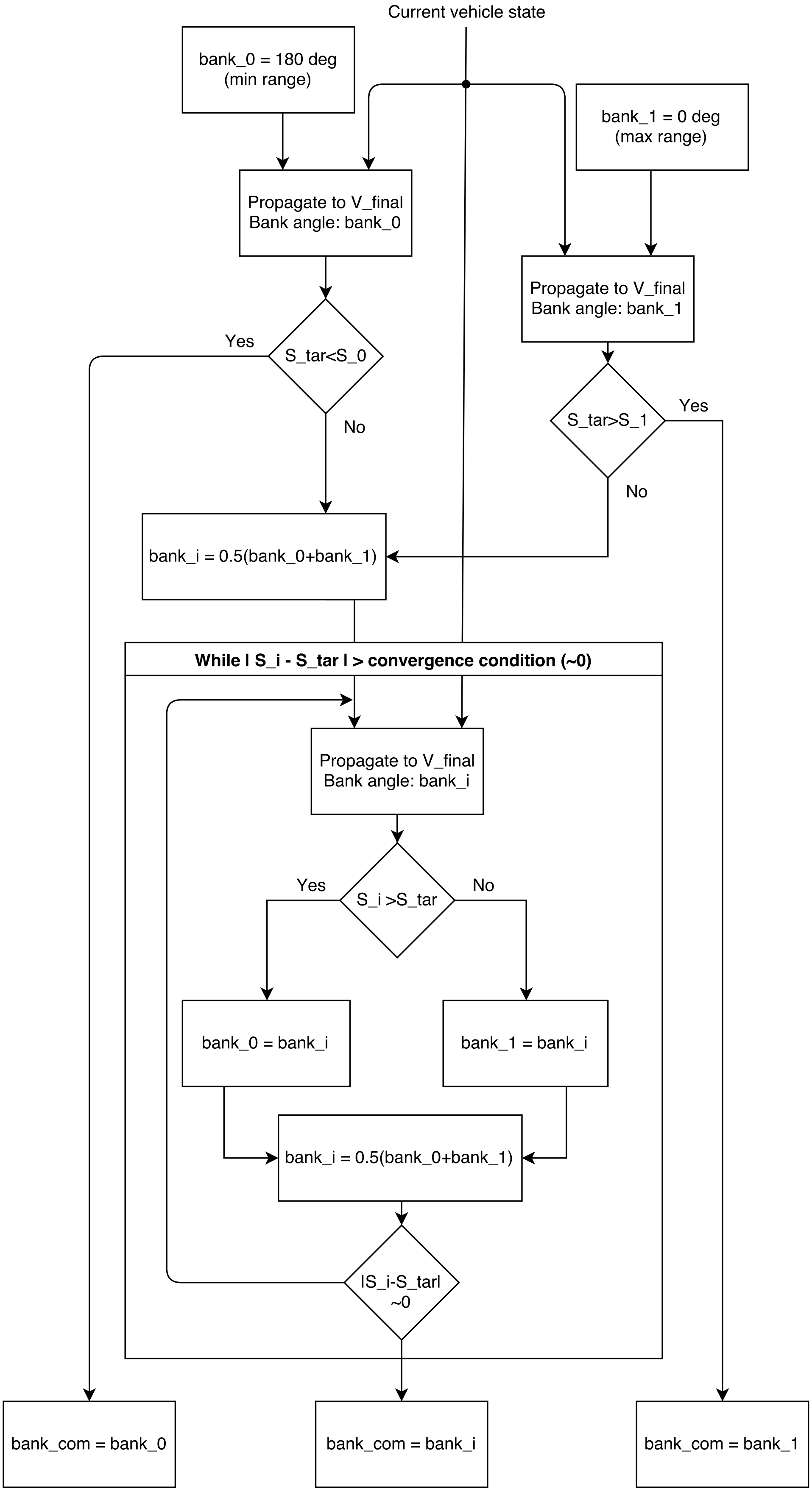

Figure 4.2: Flow chart of the guidance algorithm during execution with $bank\_com$ as output and the current state of the vehicle as input.

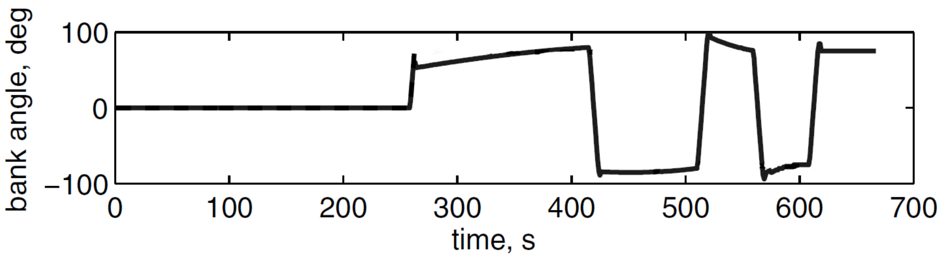

Figure 4.3: Example plot of the bank angle as function of time for a reentry using bank reversals for control (Lu, 2008).

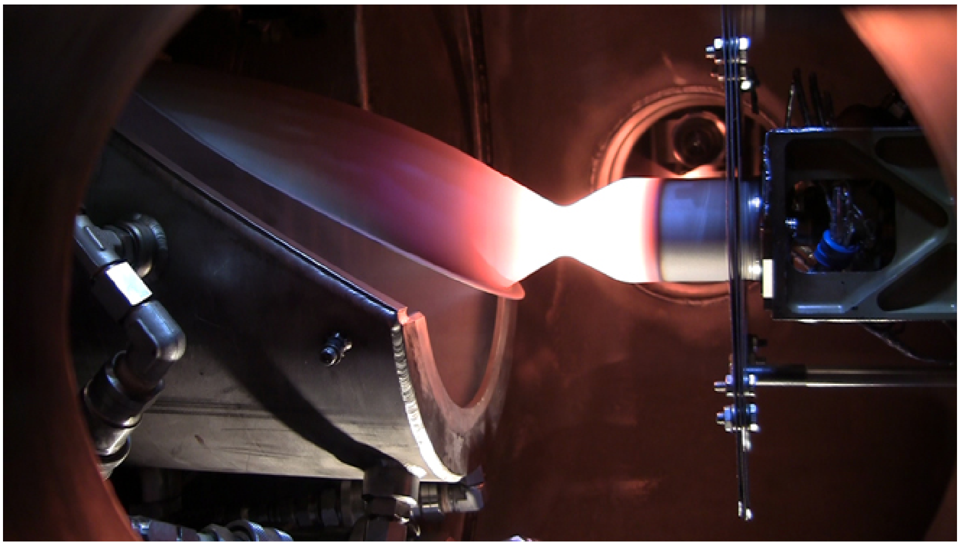

Figure 4.4: Image of the Draco rocket engine during testing. Image credit: SpaceX

4.2.1. Attitude Control Actuator

Controlling the attitude of a spacecraft requires an actuator capable of producing a torque, which turns the spacecraft to a desired orientation. This can be achieved by means of using internal momentum storage devices, such as reaction wheels, external fields or pressure, such as the flow of air from Earth's atmosphere, or forces produced by properly distributed and aligned thrusters. In this particular case the upper stage roll axis is controlled using a set of attitude control thruster while relying on the atmosphere for passive control of yaw and pitch. The attitude rates along all three axis are also controlled using thrusters.

To determine the maximum available control moment and assess propellant amount required for a controlled descent key performance data of a suitable attitude control thruster is required. While recent versions of the Falcon 9 second stage uses nitrogen gold-gas thruster to control its attitude the first generation upper stage of the Falcon 9 used a 400 N hypergolic bi-propellant thruster called Draco (SpaceX, 2009, 2015). The Draco is similar to the R-4D thruster used in the Apollo capsule in terms of propellant type and thrust, which has an specific impulse of around 300 s (Stechman and Harper, 2010). Since the specific impulse for the Draco thruster has not been made public, it is reasonable to also assume 300 s given the similarities. Figure 4.4 shows a Draco thruster during testing for use as attitude and orbit control actuator on the Dragon spacecraft.

With the thrust of the Draco engine and the dimensions of the upper stage a value for the maximum possible control moment can be derived. But to do that an arrangement of the thruster for moment generation has to be assumed.

One possible arrangement is shown in Figure 4.5, where the thrusters are placed in the rear of the upper stage in the area around the thrust cone surrounding the engine. There the thrusters are protected from the incoming airstream yet are able to fire into open space. As an example roll control is achieved by firing one of the engines on the top and one at the bottom of the stage in opposite directions. Yaw can be controlled by firing both top and bottom engines into the same direction. For

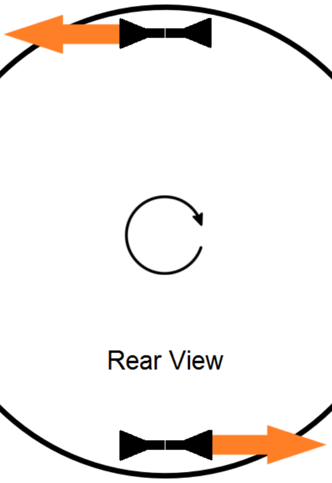

Figure 4.5: Possible thruster arrangement for roll, pitch and yaw control.

pitch the two engines on the left and right are fired into the same direction. While this arrangement is used as baseline for the control system other arrangement are possible, which need a smaller number of thrusters.

Assuming the arrangement given in Figure 4.5 and knowing the stage diameter to be $D_{F9} = 3.66$ m the maximum available moment for roll control is 1464 Nm, since the thrusters can not be placed further out than the maximum radius of the stage. Hence, this maximum control moment and those for the other two axis have to be taken into account when designing the controller.

The specifications given for the Draco engines are also required to determine the amount of propellant used during ascent. From rocket propulsion theory the relationship between thrust and mass flow is given by Equation (Sutton and Biblarz, 2010)

$$F_{draco} = \dot{m} I_{sp} g_0 \tag{4.6}$$

The specific impulse I_{sp} is a measure of efficiency of the conversion of propellant mass flow into thrust. Integrating the mass flow over the entire reentry and descent flight time yields the total propellant amount consumed.

$$M_{prop} = \int_{t_0}^{t_f} \dot{m} dt = \int_T \frac{F_{draco}}{I_{sp} g_0} dt \tag{4.7}$$

4.2.2. Feedback Control

The task of a controller is to move the state of a given system or plant from the current to a desired state. A feedback loop is used to feed the current state of the system into the controller. This allows the controller to apply control inputs appropriate for any given state to achieve a desired response. A system is typically given in a so-called state-space format for non-linear systems as shown in Equation 4.8, where **x** is its current state and **u** is the control input (Mooij, 2015).

$$\dot{\mathbf{x}} = \mathbf{A}\left(t, \mathbf{x}, \mathbf{u}\right) \tag{4.8}$$

Most problems are non-linear, but control theory is mostly focused on linear systems, for which powerful tools have been developed. Non-linear systems are therefore linearized through a Taylor series expansion to make them suitable for these tools. The state-space format of a linear system is given as (Mooij, 2015):

$$\dot{\mathbf{x}} = \mathbf{A}\mathbf{x} + \mathbf{B}\mathbf{u} \tag{4.9}$$

A state feedback controller uses the state $\mathbf{x}\left(t\right)$ to determine the value of the control input given as:

$$\mathbf{u} = -\mathbf{K}\mathbf{x} \tag{4.10}$$

The goal is to determine the gain Matrix **K** such that the state is driven towards the desired value. This is one of the major fields of control theory and several methods exist to find suitable gains.

Most feedback controller are Proportional-Integral-Derivative or PID controller for which the gains are mostly determined through trial and error in the field. However, there are more systematic ways to determine some or all of the gains experimentally or mathematically (Bechhoefer, 2005). One method to mathematically arrive at an optimal feedback controller is the Linear-quadratic regulator.

4.2.3. Linear Quadratic Regulator (LQR)

The linear quadratic regulator is a method to systematically determine optimal control gains for a given linear or linearized model. It does that by defining a cost function based on the settling deviation and control effort for which it finds an optimal solution. The cost function can be stated as (Mooij, 2015):

$$\mathbf{J} = \int_0^\infty \left(\mathbf{x}^T\mathbf{Q}\mathbf{x} + \mathbf{u}^T\mathbf{R}\mathbf{u}\right) dt \tag{4.11}$$

Here the term $\mathbf{x}^T\mathbf{Q}\mathbf{x}$ represents the control deviation and $\mathbf{u}^T\mathbf{R}\mathbf{u}$ is the control effort. The goal is to minimize both by finding an optimal set of gains. The matrices $\mathbf{Q}$ and $\mathbf{R}$ can be used to put more weight on either aspect.

One way of determining them is by using known limitations of the system as shown in Equation 4.12 and Equation 4.13 for $\mathbf{Q}$ and $\mathbf{R}$, respectively. The variable $x_{i,max}$ is the maximum allowable amplitude of the i-th state vector element and $u_{i,max}$ the maximum allowable control input of the i-th control vector element (Mooij, 2015).

$$\mathbf{Q} = \mathrm{diag}\{\ \Delta x_{1,max}^{-2} \quad \Delta x_{2,max}^{-2} \quad \Delta x_{3,max}^{-2} \ \dots\ \Delta x_{n,max}^{-2}\ \} \tag{4.12}$$

$$\mathbf{R} = \mathrm{diag}\{\ \Delta u_{1,max}^{-2} \quad \Delta u_{2,max}^{-2} \quad \Delta u_{3,max}^{-2} \ \dots\ \Delta u_{m,max}^{-2}\ \} \tag{4.13}$$

The optimal gain matrix $\mathbf{K}$, which minimizes the cost function given in Equation 4.11, can be found by solving Equation 4.14, where the matrix $\mathbf{B}$ is the same as in the state-space model of a system give in Equation 4.9.

$$\mathbf{K} = \mathbf{R}^{-1}\mathbf{B}^T\mathbf{P} \tag{4.14}$$

The parameter $\mathbf{P}$ can be solved for numerically using the so-called Riccati equation given in Equation 4.15 (Bechhoefer, 2005). With that the gain matrix **K** can now be calculated by plugging the resulting value for $\mathbf{P}$ back into Equation 4.14.

$$\mathbf{A}^T\mathbf{P} + \mathbf{P}\mathbf{A} - \mathbf{P}\mathbf{B}\mathbf{R}^{-1}\mathbf{B}^T\mathbf{P} + \mathbf{Q} = \mathbf{0} \tag{4.15}$$

4.2.4. Linearized Attitude Dynamics

Using the linear-quadratic regulator to determine optimum gains for the attitude controller requires a linearized model of the attitude of the vehicle. The dynamic and kinematic equations for the attitude of a given spacecraft are given in Equation 4.16 and Equation 4.17, respectively.

$$\dot{\boldsymbol{\omega}} = \mathbf{J}^{-1}\left(\mathbf{M} - \boldsymbol{\omega} \times \mathbf{J} \cdot \boldsymbol{\omega}\right) \tag{4.16}$$

$$\dot{\mathbf{q}} = \frac{1}{2}\begin{bmatrix} -q_4 & -q_3 & q_2 \\ q_3 & -q_4 & -q_1 \\ -q_2 & q_1 & -q_4 \\ q_1 & q_2 & q_3 \end{bmatrix}\boldsymbol{\omega} \tag{4.17}$$

The term **M** is the moment vector acting on the spacecraft. For the control gain calculations the control moments are assumed to be the only moments acting on the vehicle. This assumption is valid for this particular case, because only the roll of the vehicle is controlled to achieve a desired bank angle. As explained in Section 3.5 due to the axis symmetry of the vehicle no aerodynamic roll moment is generated leaving the roll control moment as the only moment acting around the X-axis of the vehicle.

The pitch and yaw axis are not actively controlled during reentry and rely on the atmosphere to maintain a passive trim attitude.

By applying a Taylor-Series expansion and discarding higher order terms one can linearize these equations around a nominal state. Using the stationary point $q_1, q_2, q_3 = 0$, $q_4 = 1$, and $\omega_1, \omega_2, \omega_3 = 0$ as nominal state results in the linearized system of equations given in Equation 4.18 (Yang, 2012).

$$\begin{pmatrix} \dot{\boldsymbol{\omega}} \\ \dot{\mathbf{q}} \end{pmatrix} = \begin{bmatrix} \mathbf{0}_3 & \mathbf{0}_3 \\ -\frac{1}{2}\mathbf{I}_3 & \mathbf{0}_3 \end{bmatrix} \begin{pmatrix} \boldsymbol{\omega} \\ \mathbf{q} \end{pmatrix} + \begin{bmatrix} \mathbf{J}^{-1} \\ \mathbf{0}_3 \end{bmatrix} \mathbf{u} \tag{4.18}$$

The matrices $\mathbf{A}$ and $\mathbf{B}$ specific for this attitude problem and required to solve Equation 4.15 are in this case given in Equation 4.19 and Equation 4.20, respectively (Yang, 2012).

$$\mathbf{A} = \begin{bmatrix} \mathbf{0}_3 & \mathbf{0}_3 \\ \frac{1}{2}\mathbf{I}_3 & \mathbf{0}_3 \end{bmatrix} \tag{4.19}$$

$$\mathbf{B} = \begin{bmatrix} \mathbf{J}^{-1} \\ \mathbf{0}_3 \end{bmatrix} \tag{4.20}$$

4.2.5. Combined Open/Closed Loop Controller

As mentioned before, the angle of attack and side-slip angle is controlled passively using the aerodynamic moments, which push the attitude towards the trim position. This trim position can change slightly throughout the trajectory with changing flight conditions and can be somewhat unpredictable. Given the strong aerodynamic moments acting on the vehicle any attempt to remove its attitude from the trim position is futile. Even if the goal of the control system is to steer the attitude towards the trim position the uncertainty in its exact location simply results in a waste of fuel as well, since it is likely that the predicted location is somewhat off and the controller will constantly try to correct for the gap against the aerodynamic moment.

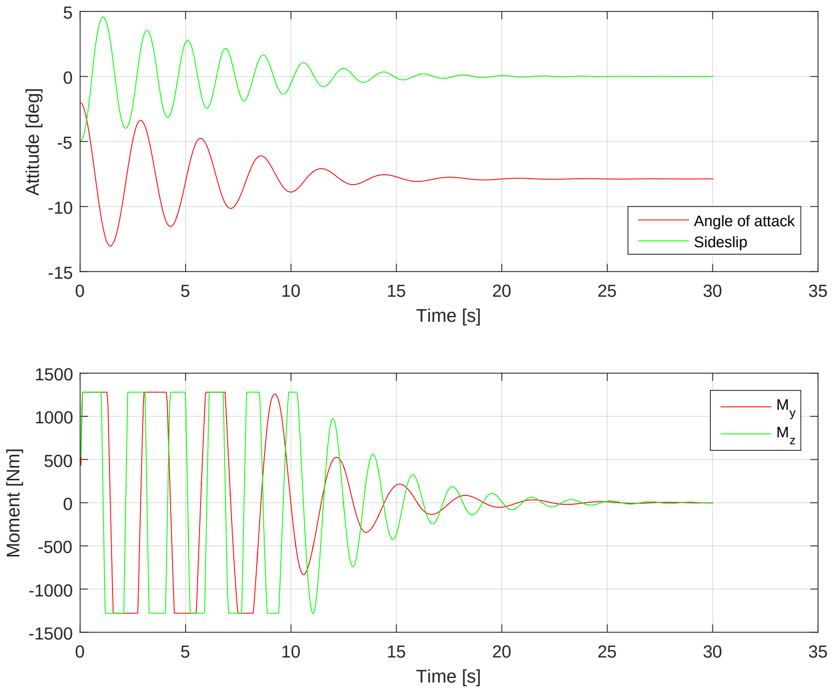

Figure 4.6: Combined open-closed-loop controller response to a step in the commanded bank angle from $90°$ to $-90°$ with the roll rate set to $15°$/s.

Hence, the best course of action is to trim the vehicle for a desired angle of attack and side-slip angle. The control is only used to dampen the angular rates around the pitch and yaw axis. This removes any unwanted oscillation relatively quickly, which would otherwise persist for an extended period of time. The angular rate controller response to an initial deflection in angel of attack of $5°$ and side-slip angle of $-5°$ at 50 km altitude and Mach 20 is plotted in Figure 4.6.

The deflection in the angle of attack and side-slip angle results in an oscillation, which is damped out by the pitch and yaw controller. In the bottom plot the applied control moment show that despite the application of the maximum possible control moment to stop the rate the oscillation still continues for a few cycles, due to the high aerodynamic moments. To prevent any oscillation at the given deflection angle would require very high control moments, which is not practical. However, the dampening achieved with the controller is sufficient to remove any oscillation quickly compared to no rate control for the pitch and yaw axis.

To test the closed-loop bank angle feedback controller derived for the upper stage using optimal control theory a step input in the commanded bank angle is applied. The limits of the controller are probed by commanding the vehicle to perform a $180°$ bank reversal, which is the maximum possible bank error. The vehicle is in vacuum to illustrate also the motion of the angle of attack and side-slip angle when rolling the vehicle. During reentry any angle of attack and side-slip errors from the trim position caused by the roll are corrected by aerodynamic moments. Since the aerodynamic roll moment of the vehicle is always zero, the roll behavior in vacuum is also representative of that in the atmosphere. The response is shown in Figure 4.7.

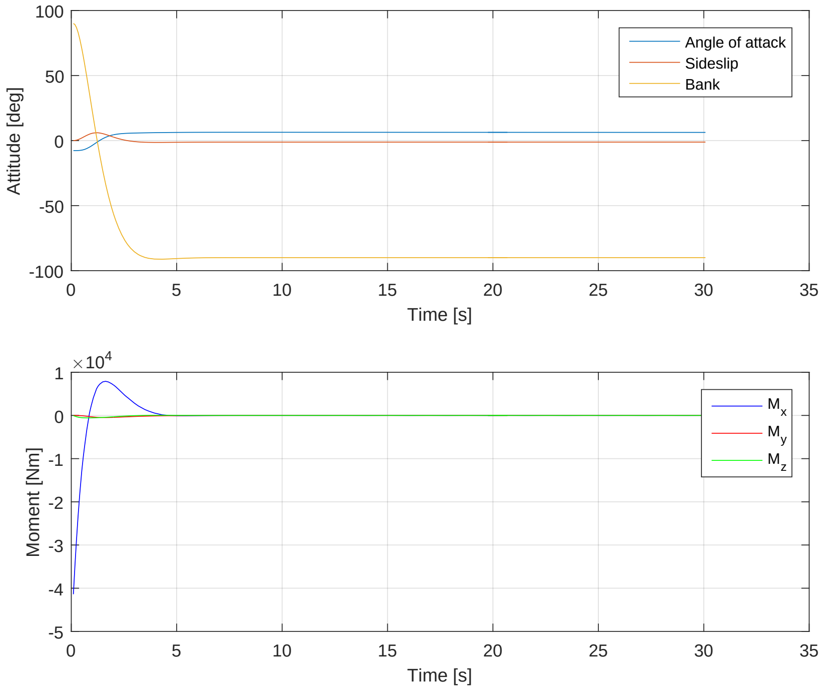

Figure 4.7: Closed-loop controller response to a step in the commanded bank angle from $90°$ to $-90°$.

While the response looks satisfactory in terms of overshoot and convergence one can immediately see that the maximum control moment constraint is violated, which also leads to an excessive attitude rate. The cause for this violation is the assumptions of small angular rates used to linearize the vehicle's attitude dynamics. This assumption no longer applies when dealing with large angles, such as the bank error used here. Simply limiting the applied moment at the maximum for the vehicle invalidates the optimum solution found using the LQR theory and results in an overall not well adjusted controller.

To solve this problem an addition open-loop controller is added to the closed-loop controller and is active for large bank errors. Once the current bank angle is getting close to the commanded bank angle the controller switches to the closed-loop controller, which performs the final convergence of the attitude to the desired state. A flow chart showing the logic behind the two control schemes and when the algorithm decides which one to use is shown in Figure 4.8.

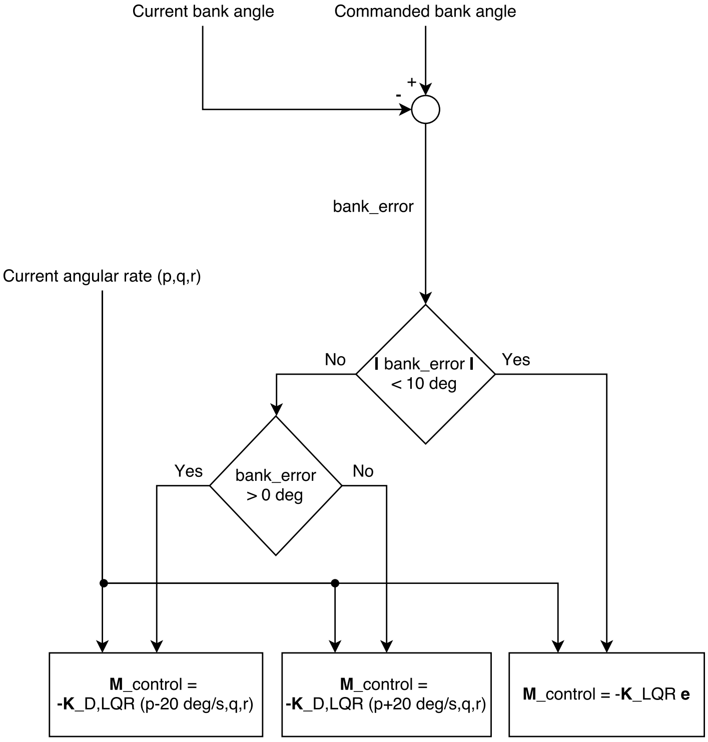

Figure 4.8: Flow chart of the guidance algorithm during execution with $bank\_com$ as output and the current state of the vehicle as input.

The open-loop controller works by simply setting the roll rate of the vehicle to a specified value in the direction of the commanded bank angle. The roll is stopped by the closed-loop controller once the attitude comes within set limits of the target attitude.

The switching condition between the two controls is a trade-off between setting the limits wide enough to give the close-loop controller sufficient time to catch the roll introduced by the open-loop controller and tight enough to make the small-angle approximation valid for the close-loop controller.

In addition to the maximum possible control moment maximum angular rates are physical limitations imposed by the hardware or payload on board the spacecraft. The Apollo CM, for example, has a roll rate capability of $20°$/s (Steketee, 1967). Using the same attitude rate limit and a closed-loop control activation band of $\pm 20°$ within the target bank angle results in the control profile given in Figure 4.9.

This time the top figure shows a satisfactory performance of the bank angle controller in all aspects. The bottom plot shows the control moment applied to achieve the desires change in attitude. The control moment increase to the its maximum value as expected for initiating the roll motion to $20°\ \mathrm{s}^{-1}$ using the open-loop controller. The second bump is the closed-loop controller stopping all angular motion and converging the attitude to the commanded attitude. Here the maximum control moment is reached as well, which indicates that the small angular rate approximation is again not quite valid for a set angular rate of $20°\ \mathrm{s}^{-1}$. Reducing the angular rate to $15°\ \mathrm{s}^{-1}$ results in the solution given in Figure 4.10.

In this figure the roll control moment applied by the close-loop controller stays at less than the maximum possible control moment and consumes less control authority at the cost of increased time till convergence. However, due to importance of fast reversals for a successful guided entry and the good performance of the controller displayed in Figure 4.9 a set angular rate of $20°\ \mathrm{s}^{-1}$ is used. A closed-loop activation band of $\pm 20°$ is found to work well with the given angular rate. A tighter band leaves the closed-loop controller no room to arrest the motion, while a wider band causes the closed-loop system to become invalid again, resulting in an unnecessary acceleration towards the target, excessive overshoot, and long settling times.

To inspect the controller response to the attitude change maneuver shown in Figure 4.9 within the same flight condition as in Figure 4.6 the $180°$ bank angle change is repeated with the vehicle at 50 km altitude and Mach 20. The response is plotted in Figure 4.11 and shows a bank angle behavior similar

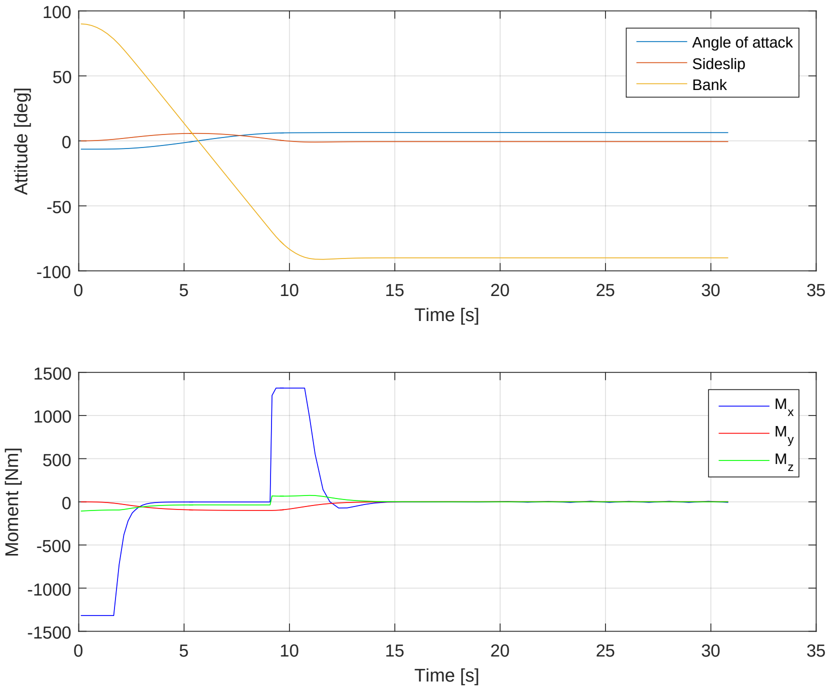

Figure 4.9: Combined open-closed-loop controller response to a step in the commanded bank angle from $90°$ to $-90°$ with the roll rate set to $20°\ s^{-1}$.

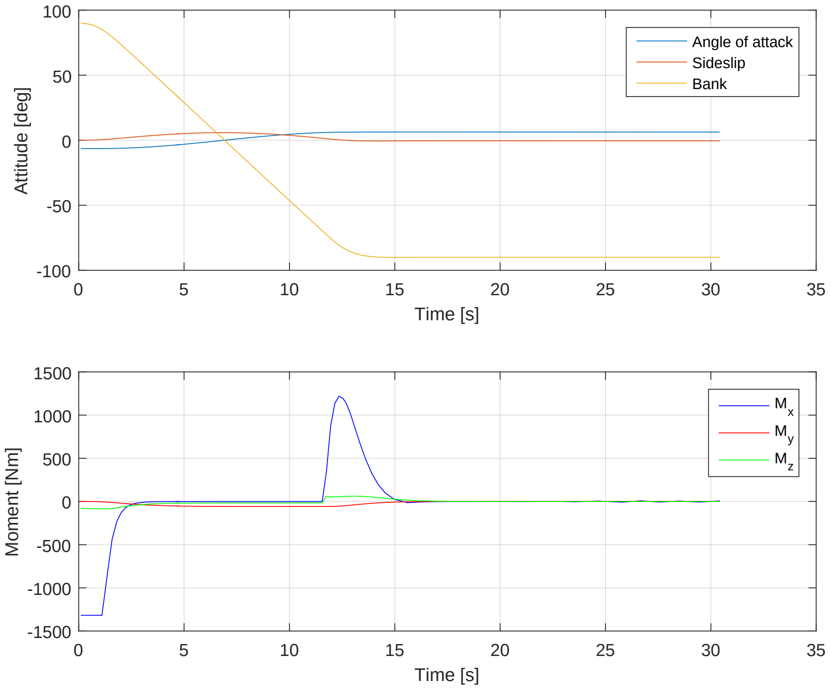

Figure 4.10: Combined open-closed-loop controller response to a step in the commanded bank angle from $90°$ to $-90°$ with the roll rate set to $15°$/s.

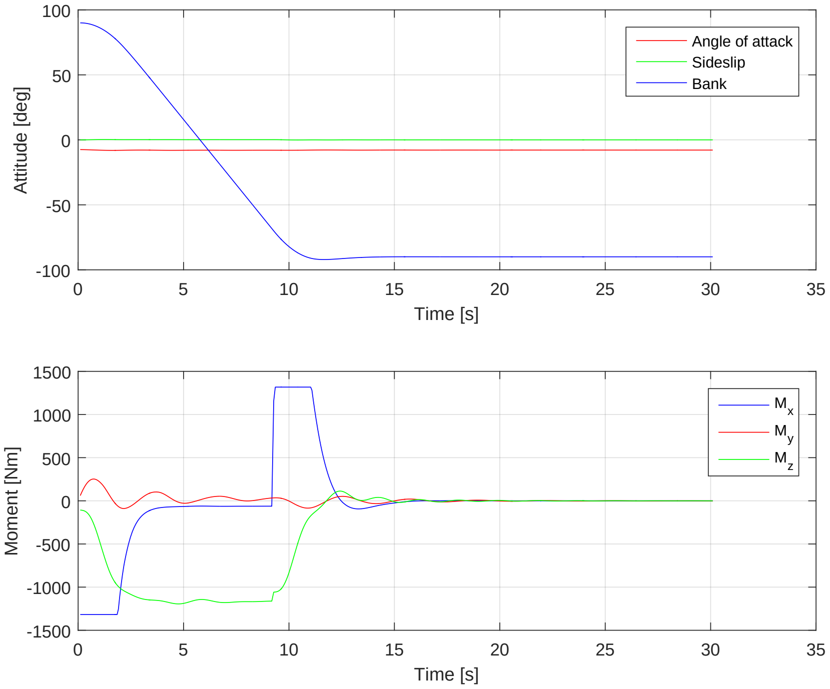

Figure 4.11: Combined open-closed-loop controller response to a step in the commanded bank angle from $90°$ to $-90°$ at Mach 20 at 50 km altitude.

to the response in vacuum.

The long-term oscillation of the angle of attack and the side-slip angle during the roll as observed in vacuum is prevented by the strong aerodynamic moments, which try to maintain the vehicle in the trim attitude. The relatively high angular velocity is then damped by the pitch and especially yaw controller. The yaw control is more strongly active here, because the angle of attack is at its highest point of the oscillation with the rate of change at its minimum while the side-slip angle is at zero and is at its maximum rate of change. As the attitude is constantly reset by the aerodynamic moments and the controller dampens any short term oscillation the yaw continuously deflects resulting in a corresponding push back by the aerodynamic moment and yaw controller response. The pitch experiences only slight motion due to being at the top of the sinus curve of the oscillation.

5

Simulator Design

In the previous chapters the theoretical background required to construct a dynamic model of the vehicle, its controls, and its environment are discussed. In this chapter the implementation of these mathematical constructs into a reentry simulator is discussed. First the numerical methods used in the simulator are presented in Section 5.1. Then the architecture and all the function blocks of the simulator are illustrated in Section 5.2.

5.1. Numerical Methods

To use the differential equations of motion derived in Chapter 3 to predict the trajectory of a vehicle a numerical integrator is required. Other numerical methods are also used to turn discrete data points into a continuous function for use in the simulation or find the root of a complicated function. Numerical methods not only offer a path to finding solution for problems impossible to solve analytically, but also leverage the power of modern computers to quickly arrive at the solution. In this section the numerical integrator, the interpolation methods, and root-finding method used in the reentry simulator are discussed.

5.1.1. Numerical Integrator

Numerical integration is the integration of a function by means of discrete steps and use of the local derivative. The solution is an approximation and always contains a certain error, but that error can be minimized and controlled by means of integration method and choice of steps size.

A simple example for an integration method is the Euler method, which uses the local derivative and multiplies it by a chosen steps size to approximate linearly the difference between the current state and the state a step size away from now in the future. In this case the cause of the error is the assumption that the system is linear between the current and the next step. This is rarely the case. However, one can see that any curvature the function may have decreases between two steps the smaller the chosen step size is. Hence one strategy to reduce the error of numerical integration is to keep the step size sufficiently small. However, reducing the step size indefinitely has practical limitations, such as computation time and the machine epsilon (Press et al., 2007).

Following the same line of thinking it becomes also clear that the higher the rate of change of a function is at any given point the higher the numerical integration error becomes, which assumes a constant rate such as the euler method.

A different approach to improving the efficiency of the numerical integration is to use methods based on higher order polynomials or multiple sub-steps to achieve a more precise result for any given step size. Further improvements in performance can be introduced by using a variable step size, which adapts to the local rate of change and save computation time (Press et al., 2007).

The following paragraphs give a brief introduction into a general set of numerical integration methods of varying orders and describes the integration method used for the propagation of the state of the reentry vehicle in the simulation.

Runge-Kutta methods The Runge-Kutta numerical integration method is a set of integration methods, which include the Euler method mentioned earlier. A general expression of the function of the state at the next time step $n+1$ as a function of the state at the current time step n and the step size Δt is given as (Press et al., 2007):

$$y_{n+1} = y_n + \sum_{i=1}^{s} b_i K_i \tag{5.1}$$

The Runge-Kutta parameters K_i, which are sub-steps between the initial point and next point, are calculated using the set of equations given in Equation 5.2. The order of the integrator can be chosen by selecting the appropriate number of stages s (Press et al., 2007). Note that with the parameter $s = 1$ the resulting method is the Euler method described earlier.

$$\begin{gathered}
K_1 = \Delta t f\,(t_n, y_n) \\
K_2 = \Delta t f\,(t_n + c_2 \Delta t, y_n + a_{21} K_1) \\
K_3 = \Delta t f\,(t_n + c_3 \Delta t, y_n + a_{31} K_1 + a_{32} K_2) \\
K_4 = \Delta t f\,(t_n + c_4 \Delta t, y_n + a_{41} K_1 + a_{42} K_2 + a_{43} K_3) \\
\vdots \\
K_s = \Delta t f\left(t_n + c_s \Delta t, y_n + a_{s1} K_1 + a_{s2} K_2 + a_{s3} K_3 \ldots + a_{s,s-1} K_{s-1}\right)
\end{gathered} \tag{5.2}$$

The Runge-Kutta coefficients a_{ij}, b_i, and c_i give weights to certain sub-steps performed within the evaluation of the next state. The coefficients a_{ij} can be chosen arbitrarily and introduce variations into methods of the same order. The coefficients b_i, and c_i then follow from the choice of a_{ij} as shown in the so called Butcher-tableau given in Table 5.1. The corresponding values of the coefficients b_i, and c_i can be calculated according to Equation 5.3 and Equation 5.4, respectively (Press et al., 2007).

0					
c_2	a_{21}				
c_3	a_{31}	a_{32}			
c_4	a_{41}	a_{42}	a_{43}		
$\vdots$	$\vdots$			$\ddots$	
c_s	$a_{s,1}$	$a_{s,2}$	$a_{s,3}$	$\cdots$	$a_{s,s-1}$
	b_1	b_2	$\cdots$	b_{s-1}	b_s

Table 5.1: Butcher tableau for the Runge-Kutta coefficients (Press et al., 2007).

$$\sum_{j=1}^{i-1} a_{ij} = c_i, \quad \text{where } i = 2, 3, \ldots, s \tag{5.3}$$

$$\sum_{i=1}^{s} b_i = 1, \quad \text{where } i = 1, 2, \ldots, s \tag{5.4}$$

This set-up allows for the derivation of a multitude of different integration methods at various orders. The choice of method specific method depends on the problem at hand and may be determined through experimentation. However, trying them all out is impractical given the sheer number of methods available.

Methods of higher order are generally more efficient for problems with tight error boundaries. However, they require a method-specific minimum number of substeps for each step. For problems with relatively wide error bounds, it may become more computationally intensive than an integration method with a lower order at the same or smaller step size. On top of that comes the rising complexity of the method with increasing order, which makes its implementation into software more difficult and time consuming compared to lower order methods (Nagel, 2012).

For the reentry simulator the Dormand-Prince method is used. It is a well-performing general-purpose propagator and provides a good balance between all the points stated above. A implemented version of that propagator is available and verified in TUDAT.

Dormand-Prince method The Dormand-Prince method is an explicit integration method based on Runge-Kutta methods of the order 4 and 5. It uses these two Runge-Kutta methods to optimize for a step size for which the magnitude of the residual error is less then a specified amount. This improves the overall efficiency of the integrator by selecting a large step size during periods where changes in the state derivative are small and a small step size for periods where changes in the derivative are large. Assuming a vehicle has a nearly constant acceleration, performing a numerical integration with a relatively large step size results in a small error compared to a situation with a rapidly changing acceleration where a smaller step size needs to be used for the same error magnitude (Press et al., 2007).

Variable step size integrators, such as the Dormand-Prince method, make use of the known precision of methods of different orders to estimate the error introduced at every step. The step size is then adjusted accordingly until the error is below a specified tolerance threshold. For the Dormand-Prince method the step size is adjusted using the scaling factor s given in Equation 5.5 where the tolerated error magnitude is given as ϵ_{ref} and the error between the results of the two integration methods of different order is given as ϵ. The new step size can now either be used to repeat and improve the current step or can be used to continue the integration (Press et al., 2007).

$$s = \sqrt[5]{\frac{\Delta t \epsilon_{ref}}{2|\epsilon|}} \tag{5.5}$$

The Runge-Kutta 4 and Runge-Kutta 5 integrator used for the Dormand-Prince method are given in Equation 5.6 and Equation 5.7 respectively with their respective substeps K_1 - K_7 given in Equations 5.8 - 5.14 (Press et al., 2007).

$$y_{n+1} = y_n + \frac{35}{384}K_1 + \frac{500}{1113}K_3 + \frac{125}{192}K_4 - \frac{2187}{6784}K_5 + \frac{11}{84}K_6 \tag{5.6}$$

$$z_{n+1} = y_n + \frac{5179}{57600}K_1 + \frac{7571}{16695}K_3 + \frac{393}{640}K_4 - \frac{92097}{339200}K_5 + \frac{187}{2100}K_6 + \frac{1}{40}K_7 \tag{5.7}$$

$$K_1 = \Delta t f\,(t_n, y_n) \tag{5.8}$$

$$K_2 = \Delta t f\left(t_n + \frac{1}{5}\Delta t, y_n + \frac{1}{5}K_1\right) \tag{5.9}$$

$$K_3 = \Delta t f\left(t_n + \frac{3}{10}\Delta t, y_n + \frac{3}{40}K_1 + \frac{9}{10}K_2\right) \tag{5.10}$$

$$K_4 = \Delta t f\left(t_n + \frac{4}{5}\Delta t, y_n + \frac{44}{45}K_1 - \frac{56}{15}K_2 + \frac{32}{9}K_3\right) \tag{5.11}$$

$$K_5 = \Delta t f\left(t_n + \frac{8}{9}\Delta t, y_n + \frac{19372}{6561}K_1 - \frac{25360}{2187}K_2 + \frac{64448}{6561}K_3 - \frac{212}{729}K_4\right) \tag{5.12}$$

$$K_6 = \Delta t f\left(t_n + \Delta t, y_n + \frac{9017}{3168}K_1 - \frac{355}{33}K_2 - \frac{46732}{5247}K_3 + \frac{49}{176}K_4 - \frac{5103}{18656}K_5\right) \tag{5.13}$$

$$K_7 = \Delta t f\left(t_n + \Delta t, y_n + \frac{35}{384}K_1 - \frac{500}{1113}K_3 + \frac{125}{192}K_4 - \frac{2187}{6784}K_5 + \frac{11}{84}K_6\right) \tag{5.14}$$

To efficiently use this method requires a tolerance, which balances computation power and accuracy. The relationship is not immediately obvious from the tolerance itself, since it only specifies the allowable error with one integration step and accumulates over the entire duration of the simulation. Hence the choice of the right tolerance depends on the application and duration of the simulation.

Since reference data for the exact solution of the equation of motion derived in Chapter 3 is not available, the results for different tolerances can not directly be judged. However, one way of assessing the error is by comparing the results of the same simulation using different tolerances and observing their convergence pattern. The results of simulations with different tolerances are given in Table 5.2. The results show that the error in position is overall small with differences of less than 100 m between tolerances of 10^{-6} and 10^{-8}. The difference between the results of tolerances of 10^{-12} and 10^{-14} is less than 10 m.

A tolerance of 10^{-12} is used, since the integration error in the results is well below the limit set by the requirements for the simulator. A smaller tolerance result in significantly increased computation time with diminishing gains in accuracy.

Tolerance	Longitude	Latitude	Altitude
10^{-6}	$-80.33116564°$	$28.12982416°$	17947.42327 m
10^{-8}	$-80.33195259°$	$28.13002662°$	18007.32019 m
10^{-10}	$-80.33211422°$	$28.13006891°$	18019.85652 m
10^{-12}	$-80.33229089°$	$28.13011504°$	18033.51415 m
10^{-14}	$-80.33230689°$	$28.13011922°$	18034.74974 m

Table 5.2: Terminal position of the reusable upper stage after a passive reentry using different tolerances for the Dormand-Prince method.

5.1.2. Multi-Linear Interpolation

Aerodynamic coefficients of the Apollo capsule and the reusable upper stage are provided as discrete data points. To turn them into a continuous function for use in the simulation they are interpolated and the resulting function is used to determine the value of the aerodynamics coefficient for every given point within the interval of the available data. Since the aerodynamic coefficients of a vehicle are a function of total angle of attack, Mach number, and altitude or more specifically the Reynolds number at the current altitude, a multivariate interpolator is required.

To interpolate a set of ordered but discrete data several powerful methods exist. One of the most common method is the so-called spline interpolation where a subset of data points are joined by a suitable function, usually a polynomial function, and the functions interpolating all subsets are joined together into a spline. The most basic form of a spline is a linear spline interpolation where each two data points are connected by a straight line resulting in a continuous but not smooth function. In this case the first derivative of the function is not continuous. A linear interpolation between the two data points (x_0, y_0) and (x_1, y_1) to calculate the function value y_2 at point x_2 is done as shown in the following equation (Press et al., 2007).

$$y_2 = y_0 + \frac{y_1 - y_0}{x_1 - x_0}(x_2 - x_1) \tag{5.15}$$

To achieve a function with a continuous first derivative as well a quadratic function has to be used for the interpolation with two data points and the value of the first derivative as input for the interpolation. While a starting value for the derivative has to be assumed for the first two data points the derivative of the function at the last point can then be calculated and used for the next two data points to achieve a continuous first derivative. To go even further and interpolate a function with a smooth first and second derivative a cubic function has to be used (Press et al., 2007). While a cubic or higher order spline interpolation is a powerful method to interpolate one-dimensional functions with a single independent variable, the problem becomes increasingly complex with increasing dimensions.

For the simulation the derivative of the aerodynamic coefficients is not required and therefore a linear interpolation is sufficient. Generating the data in Missile DATCOM with an appropriate sampling resolution should further reduce any errors due to the assumption of linearity in between data points. To illustrate the magnitude of the error due to the interpolation a Missile DATCOM drag coefficients table as function of angle of attack is interpolated at the point in between the data points in the list. The resulting interpolation results are compared with the data generated by Missile DATCOM at those angle of attack points. The numbers for both cases are given in Table 5.3 and show that the interpolation matches the original data nearly perfectly with negligible differences around the last digits. The same can be observed for the lift and moment coefficient.

This indicates that the aerodynamic coefficients are nearly linear between the data points and the assumption of linearity is therefore valid. A readily-available and verified muti-linear interpolation function is included in TUDAT. This makes it the most practical and less time-consuming option compared to other existing mostly unverified interpolation tools and creating a custom interpolation function from scratch.

Angle of Attack	**Interpolated C_D**	**Missile DATCOM C_D**
0.5°	1.5775	1.577
1.5°	1.576	1.576
2.5°	1.5735	1.574
3.5°	1.5705	1.571
4.5°	1.5665	1.566
5.5°	1.561	1.561
6.5°	1.555	1.555
7.5°	1.548	1.548
8.5°	1.5405	1.541
9.5°	1.5325	1.533

Table 5.3: Difference between the interpolated drag coefficients evaluated in between two data points and the corresponding drag coefficient as generated by Missile DATCOM at the same point.

While linear interpolation is straight forward to understand for one-dimensional problems as demonstrated in Equation 5.15 for multi-dimensional functions a more elaborate derivation is required. Use can be made of a peculiar property of the linear interpolation by rearranging Equation 5.15 into (Kreysig, 1972):

$$y_2 = \frac{y_0\,(x_1 - x_2) + y_1\,(x_2 - x_0)}{x_1 - x_0} \tag{5.16}$$

Note here how the interpolated function value y_2 is equal to the sum of the distances between either data point and the point-of-interest projected on the x-axis normalized over the projection of the entire length of the interval between the two data points and multiplied by the y-value of the data point on the opposite side. This pattern can be used to systematically construct interpolators of multiple dimensions functions (Kreysig, 1972).

For the interpolation of the aerodynamic coefficients a tri-linear interpolator is required, since the coefficients are a function of the angle of attack, Mach number, and altitude. A general function with three inputs has the form:

$$v = f\,(x, y, z) \tag{5.17}$$

Following the pattern found for the one-dimensional case the tri-linear interpolator is constructed out of the normalized projections of the volumes instead of lengths between the 8 required data points and the point-of-interest N_a - N_h, which are given in Equation 5.18 - 5.25 (Kreysig, 1972).

$$N_a = \frac{(x_1 - x_2)\,(y_1 - y_2)\,(z_2 - z_0)}{(x_1 - x_0)\,(y_1 - y_0)\,(z_1 - z_0)} \tag{5.18}$$

$$N_b = \frac{(x_1 - x_2)\,(y_2 - y_0)\,(z_2 - z_0)}{(x_1 - x_0)\,(y_1 - y_0)\,(z_1 - z_0)} \tag{5.19}$$

$$N_c = \frac{(x_2 - x_0)\,(y_1 - y_2)\,(z_2 - z_0)}{(x_1 - x_0)\,(y_1 - y_0)\,(z_1 - z_0)} \tag{5.20}$$

$$N_d = \frac{(x_2 - x_0)\,(y_2 - y_0)\,(z_2 - z_0)}{(x_1 - x_0)\,(y_1 - y_0)\,(z_1 - z_0)} \tag{5.21}$$

$$N_e = \frac{(x_1 - x_2)\,(y_1 - y_2)\,(z_1 - z_2)}{(x_1 - x_0)\,(y_1 - y_0)\,(z_1 - z_0)} \tag{5.22}$$

$$N_f = \frac{(x_1 - x_2)\,(y_2 - y_0)\,(z_1 - z_2)}{(x_1 - x_0)\,(y_1 - y_0)\,(z_1 - z_0)} \tag{5.23}$$

$$N_g = \frac{(x_2 - x_0)\,(y_1 - y_2)\,(z_1 - z_2)}{(x_1 - x_0)\,(y_1 - y_0)\,(z_1 - z_0)} \tag{5.24}$$

$$N_h = \frac{(x_2 - x_0)\,(y_2 - y_0)\,(z_1 - z_2)}{(x_1 - x_0)\,(y_1 - y_0)\,(z_1 - z_0)} \tag{5.25}$$

A visual representation of all points and their notation is given in Figure 5.1. To calculate the interpolation of the function value at the point-of-interest $v_8\ (x_2, y_2, z_2)$ all normalized volumes together with the given data point values v_0 - v_7 are combined in Equation 5.26 similar to the one-dimensional case in Equation 5.16 (Kreysig, 1972).

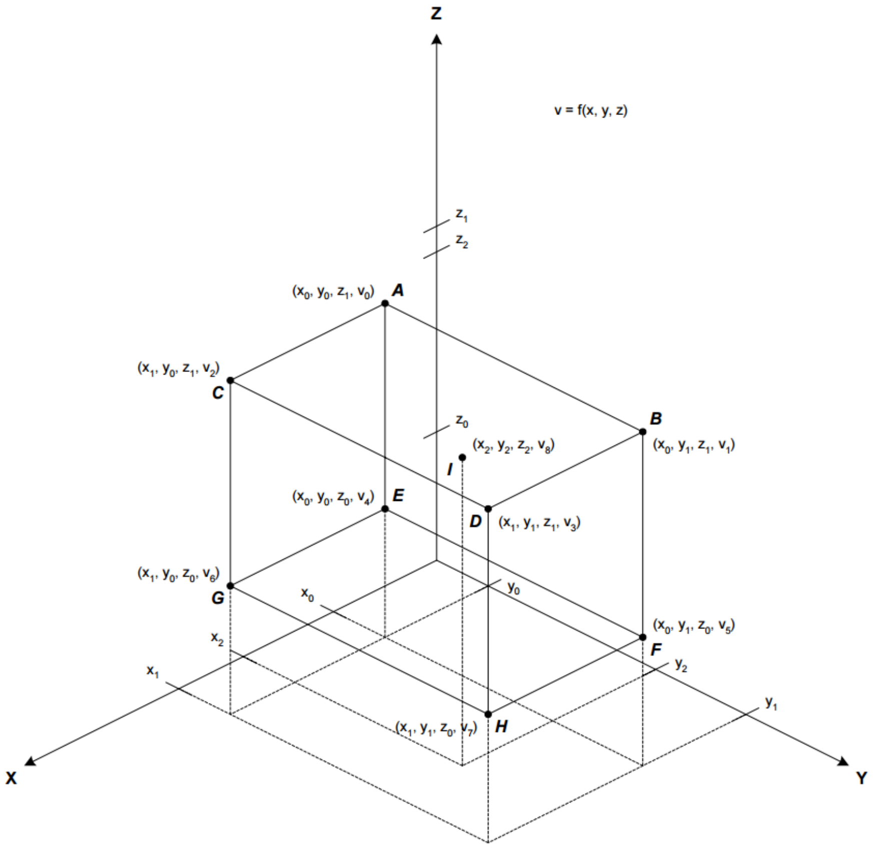

Figure 5.1: Points $(x_0, y_0, z_0)_a, (x_0, y_0, z_1)_b, \ldots (x_1, y_1, z_1)_h$ and the corresponding function values $v_0, v_1, \ldots v_7$ used for linear interpolation of point (x_2, y_2, z_2) to get the value of v_8 (Kreysig, 1972).

$$v_8 = N_a v_0 + N_b v_1 + N_c v_2 + N_d v_3 + N_e v_4 + N_f v_5 + N_g v_6 + N_h v_7 \tag{5.26}$$

5.1.3. Root-Finding Method

A root-finding method is a type of algorithm designed to find the solution to the problem $f\,(x) = 0$. While many applications do have the actual root as target, this statement can be further generalized as shown in Equation 5.27 to enable the search for any solution y.

$$f(x) = y \quad \longrightarrow \quad g(x) = f(x) - y = 0 \tag{5.27}$$

This problem statement is well suited to finding the correct variable for a desired function value for functions, which are difficult or impossible to solve analytically. In this case the root-finding algorithm can be used to find the correct bank angle magnitude for a reentry vehicle to achieve a certain downrange distance. Given the complex interactions involved in the dynamics of reentry a numerical methods is practically required to find the desired bank angle.

Many different algorithms exist to achieve this. A simple, robust, but relatively inefficient example is the bisection method. The bisection method searches for the root by evaluating the function on both edges and the center of the interval in which the root is suspected. This suspicion is confirmed if the value of the function on one edge of the interval has the opposite sign to the value of the function on the other edge of the interval. This is a necessary requirement for this method to work. For a continuous function this can only be true if the function crossed the X-axis in between the two points. Now the value of the function in the center of the interval can be compared to the two points on the edge and the same logic is applied. The root is in between the center point and the one point on the edge, which has a function value with opposite sign to the function value of the center point. This can be continued arbitrarily until the algorithm converges sufficiently to a solution. The bisection method is guarantied to find one root if there is at least one root within the interval (Press et al., 2007).

While very robust the bisection method is not computationally efficient compared to more advanced methods. One alternative is the Newton-Raphson method. This method turns any given function $f(x_n)$ and its derivative $f'(x_n)$ into a linear function with the form (Press et al., 2007):

$$x_{n+1} = x_n + \frac{f(x_n)}{f'(x_n)} \tag{5.28}$$

The principle behind this method is to find the root by determining the root of the derived linear function. This point is then used as the staring point for another iteration of linearization and root finding applied to the derived linear function. This is repeated until the algorithm converges sufficiently to the true root of the function of interest (Press et al., 2007).

This method is not as robust as the bisection method, since there are cases were the algorithm diverges away from the solution or is unable to converge at all. This happens when for instance the function contains a stationary point. This would result in a division by 0 in Equation 5.28 and halt the algorithm. Furthermore as the function comes closer to a stationary point the derivative of the function becomes increasingly small making the second term in Equation 5.28 correspondingly large. This makes the resulting linear function very flat with a root that is far away from the current position. Such an event undoes the progress done by the algorithm and could prevent it from converging if the root is sufficiently close to a stationary point (Press et al., 2007).

On top of the disadvantages of the Newton-Raphson method described here the derivative required for this and other more advance methods makes is difficult to use for optimization of the bank angle in the guidance algorithm. This method would require the derivative of the range as a function of bank angle, which is not directly available. To determine this parameter requires a significant number of additional computations, which would more than negate the higher efficiency of this root-finding method. The bisection method is therefore used for its robustness and transparency in the process of converging to a solution, which is prioritized over an increase in efficiency offered by other methods.

5.1.4. Monte-Carlo Analysis

Any process involves a certain amount of uncertainty, may it be due to a lack of knowledge about that process, measurement noise, or physical limitations preventing the full acquisition of the state of a system. For spacecraft and reentry vehicle uncertainties mostly arise from limitations in the tracking of the satellite, inaccurate orbit prediction capabilities, or unknown vehicle properties during certain mission phases. To improve confidence in the vehicle and mission uncertainties can be reduced on the ground by experiments and analysis.

One way to analyze the effect uncertainties have on the trajectory of the vehicle is to model them as random variables with a realistic spread. Using these randomized variables on successive reentry simulations can uncover trends and verify that the system functions as intended even under off-nominal flight condition. An alternative approach is to divide the variable space into a regular grid and evaluate the reentry simulation on every node. While such an approach offers a systematic way to probe the variable space, it requires a large number of evaluations to cover all combinations of variables and arrive at an exhaustive result, especially when the function has a large number of independent inputs. In the case of reentry simulations and the associated number of variables a dispersion analysis based on the Monte-Carlo method is the most practical approach.

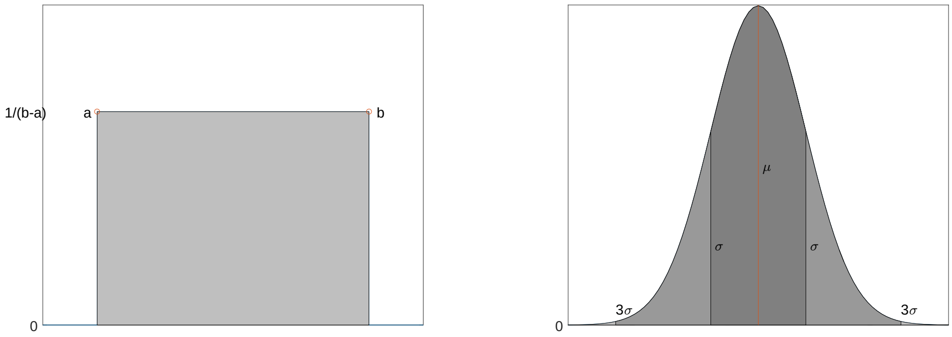

(a) Uniform distribution (b) Normal distribution

Figure 5.2: Probability density function of a uniform and normal distribution, respectively.

A continuous random variable can be designed by defining a so called probability density function (PDF). A property of PDFs in general is that integrating it over the entire space yields the value 1 as expressed in Equation 5.29, which means it encompasses all possible events. The distribution of the probabilities of events within the PDF, however, can be varied and matched to specific phenomena (Teunissen et al., 2010).

$$\int f\,(x) = 1 \tag{5.29}$$

A common type of probability distribution is the uniform distribution, where the probability for an event at any point within an interval is constant and zero outside that interval. These properties are expressed in mathematical terms in Equation 5.30 and Equation 5.29 where $f\,(x)$ is a uniform PDF within the interval from a to b (Teunissen et al., 2010).

$$f\,(x)_{uni} = \begin{cases} \frac{1}{b-a} & \text{if} \quad a \leq x \leq b \\ 0 & \text{if} \quad x \leq a \cup b \leq x \end{cases} \tag{5.30}$$

Such a distribution is useful for variables, which are expected to have no specific or an unknown probability distribution around a certain value and a fixed interval size. An example would be the attitude angle, which is constrained to an interval of size 2π or less. The attitude angles are mostly dependent on the attitude control system, which has a predetermined control accuracy. The probability of the attitude to fall at a certain point within the control accuracy 'dead-band' is regarded as constant. The PDF for a uniform distribution is plotted in Figure 5.2(a).

Another very common probability distribution used to model uncertainty is the normal distribution. This type of distribution assumes that the likelyhood of an event is the highest around an expected mean value μ and decreases rapidly the further away one is from that mean. The spread is quantified by the standard deviation σ, which marks the border of the space around the mean in which 68.2% of all possible event will fall. The second standard deviation consequently marks the space in which 95.4% of the results fall and finally the third standard deviation, also called the 3σ boundary encircles 99.6% of the events (Teunissen et al., 2010). The different probability spaces of a normal distribution are visualized in Figure 5.2(b).

Just like with the uniform distribution integration of the entire normal PDF yields 1. However, in this case the integration has to be performed over both positive and negative infinity, since the probability density far from the mean is small, but never zero. The PDF for a normal distribution is given as (Teunissen et al., 2010)

$$f\,(x) = \frac{1}{\sigma\sqrt{2\pi}} e^{\frac{-(x-\mu)^2}{2\sigma^2}} \tag{5.31}$$

A normal probability distribution is well suited to model uncertainties in predictions. Predicting the future state of s system often requires integration, which accumulates any discrepancies between reality and the model over time and propagates them further. This way a small discrepancy can have a significant effect on the final result.

An intuitive example for how a normal distribution naturally occurs is when considering playing dart. As the player tries to hit the center he will create a cloud of impact points on the target centered around the bullseye. Depending on his skills his standard deviation will either be small and the hits concentrated on the inner circles or large and spread all over and beyond the target disk. However, since he is actively aiming and adjusting to hit the target the probability that he hits it is (usually) higher than to hit the wall behind him. Predicting the trajectory of the dart and targeting its terminal position is not unlike predicting the trajectory of spacecraft and its motion in orbit around the Earth. A normal distribution is therefore well suited to model such uncertainties in the trajectory.

In addition to the two examples given here there are a large number of other continuous probability distributions. Some have a specific bounded interval in which all events occur such as the uniform distribution. Others encompass one or both negative and positive infinities such as the normal distribution. They all vary in the specific shape of their PDFs matching some random phenomena (Teunissen et al., 2010). For the preliminary analysis performed in this study the uniform and normal distributions are adequate to model all the random variables used in the dispersion analysis.

In a so-called Monte-Carlo analysis a simulation run is performed several times with the unknown or uncertain variables randomized to account for any deviations in the design or environment. This gives confidence in the concept, helps identify weaknesses, and can be used to make it more robust.

Variations in the environment such as the atmosphere or uncertainty in the trajectory are inevitable. Even the mass estimate given in Section 3.4 and the aerodynamic coefficients as provided by Missile DATCOM are likely to vary throughout the design and development process until the vehicle is complete and tested. Hence at this stage a Monte-Carlo analysis is critical to ensure the vehicle is able to complete its mission in the face of these uncertainties.

5.2. Simulator Architecture

In the previous chapters a theoretical basis for the laws governing the motion of reentry vehicle as well as numerical techniques to solve the equations of motion are presented. The only remaining task to arrive at a solution is to perform the calculations. While doing the calculation by hand on paper would certainly be possible a much more efficient way to implement such a simulation is in the form of a software script on a computer. In this section the elements and structure of the software code used to simulate the reentry of spacecraft is presented.

5.2.1. Input & Output

Every computer is designed to process inputs by using a set of instructions and produce a useful output. Hence the development of every software tool starts with the definition of the available inputs and desired outputs. In this case the goal of the software is to produces a prediction of the trajectory of a reentry vehicle using its initial condition, properties of the vehicle and properties of the environment as input. The input should be easy to understand and straight forward to change to desired values. The output should describe the trajectory in sufficient detail and also in terms of variables that are intuitive to understand.

In Chapter 3 the state vector and several auxiliary variables are presented. Although both sets of variables describe the state of the vehicle in different ways the auxiliary variables, such as flight-path angle, heading, latitude, longitude, etc., are much more intuitive in conveying the state of the vehicle compared to Cartesian coordinates and quaternions used in the state variables. Hence while the software tool works primarily with the state vector the input file contains the initial state of the vehicle in auxiliary variables. The output file contains a history of both sets of variables and additional parameters, but for an intuitive understanding of the trajectory mostly auxiliary variables are used for visualization of the results in Chapter 6. A summary of the variables contained in the input file is shown in Table 5.4(a).

The parameters shown here are single values, since the input file only contains the initial condition and properties of the vehicle. The output file on the other hand contains parameter arrays where the same element in all arrays i correspond to the state of the vehicle or the environment at the time instants t_i . All parameter and vector arrays saved in the output file are summarized in Table 5.4(b).

Input variables		
Variable	**Unit**	**Description**
t_0	[s]	Initial time
h_0	[m]	Initial altitude
V_0	[m/s]	Initial velocity magnitude in V-frame
τ_0	[rad]	Initial longitude
δ_0	[rad]	initial latitude
γ_0	[rad]	Initial flight-path angle
χ_0	[rad]	Initial heading angle
σ_0	[rad]	Initial bank angle
α_0	[rad]	Initial angle of attack
β_0	[rad]	Initial side-slip angle
$\boldsymbol{\omega}_0$	[rad/s]	Initial angular rate vector
m	[kg]	Vehicle mass
$\mathbf{J}$	[kg/m^2]	Moment of inertia tensor
$\mathbf{r}_{cg}$	[m]	COM vector in B-frame
S_{ref}	[m^2]	Reference area
L_{ref}	[m^2]	Reference length
R_1	[m]	Main heat shield radius
l_{flap}	[m]	Length of flap
w_{flap}	[m]	Width of flap
δ_{flap}	[rad]	Deflection angle of flaps
τ_T	[rad]	Target longitude
δ_T	[rad]	Target latitude
V_f	[m/s]	Final velocity magnitude in V-frame
$C_{D,ref}$	[-]	Reference drag coefficient
$C_{L,ref}$	[-]	Reference lift coefficient
ω_{max}	[rad/s]	Maximum angular rate

(a) Input Table

Output variables		
Variable	**Unit**	**Description**
t	[s]	Time
Δt	[s]	Integration time step
h	[m]	Altitude
V	[m/s]	Velocity magnitude in V-frame
τ	[rad]	Longitude
δ	[rad]	Latitude
γ	[rad]	Flight-path angle
χ	[rad]	Heading angle
σ	[rad]	Bank angle
α	[rad]	Angle of attack
β	[rad]	Side-slip angle
$\mathbf{r}$	[m]	Position vector in the I-frame
$\dot{\mathbf{r}}$	[m/s]	Velocity vector in the I-frame
$\ddot{\mathbf{r}}$	[m/s^2]	Acceleration vector in the I-frame
$\boldsymbol{\omega}$	[rad/s]	Angular velocity vector
$\dot{\boldsymbol{\omega}}$	[rad/s^2]	Angular acceleration vector
$\mathbf{q}$	[-]	Quaternion attitude vector
$\dot{\mathbf{q}}$	[s^{-1}]	Quaternion rate vector
C_D	[-]	Drag coefficient
C_S	[-]	Side force coefficient
C_L	[-]	Lift coefficient
C_M	[-]	Pitch moment coefficient
C_N	[-]	Yaw moment coefficient
$\mathbf{a}_{aero}$	[m/s^2]	Aerodynamic acceleration vector
$\mathbf{a}_{grav}$	[m/s^2]	Gravitational acceleration vector
ρ	[kg/m^3]	Air density
T	[K]	Air temperature
M	[-]	Mach number
Q_{heat}	[W/m^2]	Heat flux
$\bar{q}$	[N/m^2]	Dynamic pressure

(b) Output Table

Table 5.4: List of the simulator inputs and output.

5.2.2. Code Units & Interface

After having established the available inputs and desired outputs the process to generate the output using the input can be designed. The set of instructions is based on the theoretical background described in this report so far. Hence the software script is roughly structured in a similar fashion. A schematic overview of the primary modules and the data path through them is shown in Figure 5.3. In this figure the input and output files are shown as starting and endpoint of the process, respectively. All modules together form the reentry simulation script.

The simulator mainly consists of a while loop, which uses the terminal velocity specified in the input file as primary termination condition. In addition to the primary termination condition secondary monitoring functions ensure, for example, that the simulation does not enter a certain vehicle attitude range, for which no aerodynamic coefficients are available in the Missile DATCOM file. Another monitoring function makes sure the simulation is eventually terminated in case the vehicle has skipped or is not slowing down by limiting the total simulation time.

The simulation starts with loading input data from the input file, and DATCOM output file. Both the DATCOM Importer and the Input Importer are outside the main simulation loop. The Input Importer first converts the initial conditions in the input file into the format used by the simulator and passes this variable into the Vehicle State container. The Input Importer also saves and provides the other variables in the input file to the simulator as needed. The DATCOM Importer initializes the interpolation of the Missile DATCOM data to speed up the coefficient generation process inside the loop. The Output Exporter function on the other hand is contrary to the Input Importer still inside the loop, since it is also tasked with collecting the data during every integration step before generating the output file at the end of the simulation.

The main simulation loop starts by initializing the variable Vehicle State with the initial state of the vehicle provided by the input file. This variable is then accessed by the two main modules of the simulator, which are the Vehicle Dynamics and the Guidance and Control module. The Vehicle

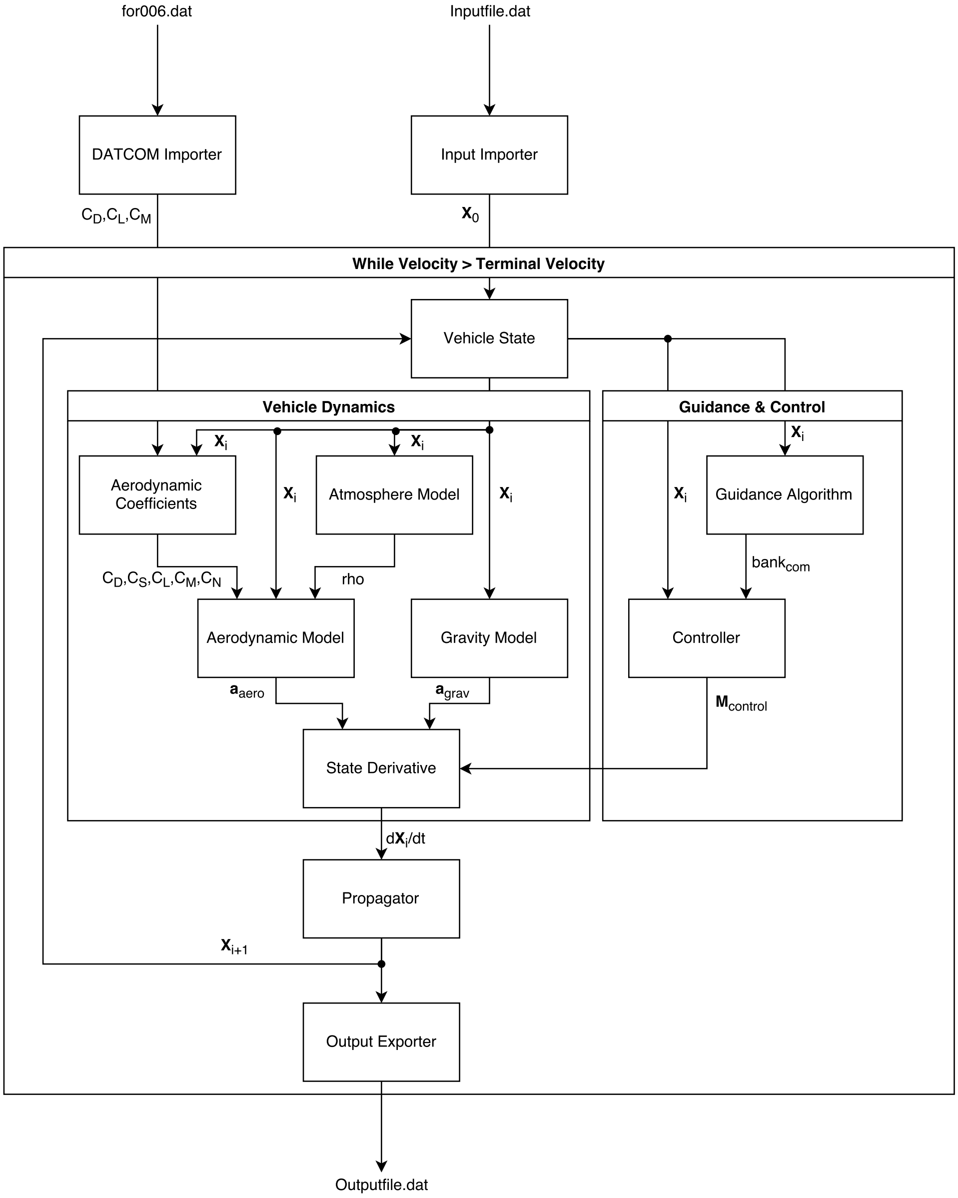

Figure 5.3: Schematic overview of the simulator showing the data flow and processing.

Dynamics module simulates the environment and motion of the vehicle using the models described in Chapter 3. The output of this module is a state derivative variable of the same size as the vehicle state variable. The output of this module is then fed into the propagator to generate the state of the vehicle at the next time step.

The Guidance and Control module interfaces with the Flight Dynamics module and provides control moments, which would otherwise be zero for an uncontrolled reentry.

A switch variable is used to turn off the angular dynamics simulation to simulate a reentry with just 3 degree of freedom or the flight dynamics to just simulate the angular dynamics of the vehicle at certain static environmental condition if needed.

Models and tools implemented into C++ functions created by the author are summarized in Table 5.5 together with a short description and method of verification.

TUDAT Some functions used in the simulation are imported from TUDAT, a C++ toolbox developed and maintained by the students and staff at the Astrodynamics and Space Missions department of the University of Technology Delft. The toolbox provides many important building blocks for creating

Code unit	**Description**	**Verfication method**
Input Importer	Reads input file and provides content and initial state to simulator.	Variables were inspected and compared to input file. State was converted back into auxiliary coordinates and compared to values in the input file.
DATCOM Importer	Reads the for006.dat file produced by DATCOM, interpolates the data, and provides aerodynamic coefficients for a given state within the range of the available data.	Coefficients were produced at several distinct points on top of and in between data points. The output is compared to values in the for009.dat output file produced by Missile DATCOM.
Transformation Matrices	Produces transformation matrices between all defined frames given the current state	A set of different test vectors were transformed. The output was tested for changes in length and nonconformity with the expected direction in the target frame.
Coordinate Transformation 1	Calculates the auxiliary coordinates corresponding to a given state.	Intuitive and random states are converted into auxiliary coordinates. The output is inspected for correctness and transformed back using 'Coordinate Transformation 2' for consistency checking.
Coordinate Transformation 2	Calculates the state corresponding to the given set of auxiliary coordinates.	Intuitive and random auxiliary coordinates are converted into a state vector. The output is inspected for correctness and transformed back using 'Coordinate Transformation 1' for consistency checking.
Exponential Atmosphere	Provides atmospheric temperature, pressure, and density for a given altitude using a simple exponential model.	Proper implementation checked by comparing output to manual computations.
Aerodynamics	Uses the current state, the vehicle's mass, and appropriate aerodynamic coefficients to calculate aerodynamic accelerations and moments acting on the vehicle.	Equations and function implementation were inspected and compared to theory. Test states were used to generate outputs, which were compared to manual computations.
Gravity model	Uses the current state to calculate the acceleration of the vehicle due to gravity.	The output is checked by comparison with expected and manually calculated values.
Euler rotation dynamics	Calculates the angular acceleration of the vehicle given the current state and the vehicle's moment of inertia.	The rotational dynamics of a rotating object was simulated with constant individual and combined rotations around all three axis. The output was analyzed.
Quaternion kinematics	Translates the current angular rate of the vehicle into the rate of change of the attitude quaternion.	This simple matrix-vector multiplication is inspected and tested by comparison with manual computation.
Guidance	Calculates the bank angle that minimizes the distance between the final position of the vehicle and the target.	See Section 5.3.3.
Controller	Outputs an appropriate control moment to eliminate any bank angle error.	See Section 4.2.

Table 5.5: List of primary functions created by the author and used in the software with a short description and method of verification.

simulations of astrodynamic phenomena. Since every function it contains is coded and compiled as C++ functions, they can easily interface with any C++ program script. Furthermore, every tool in TUDAT was carefully verified and includes a unit test to ensure its proper function. This makes it well suited for this project, since most other tools lack the proper verification, documentation thereof or are coded in an incompatible programming environment with the rest of the simulator.

For this project three TUDAT functions are incorporated into the simulation, the variable step size integrator, the multi-linear interpolator, and the US 1976 Standard Atmosphere model. They are summarized in Table 5.6.

Code unit	Description	Verfication method
Standard Atmosphere	Provides atmospheric temperature, pressure, and density for a given altitude according to the US1976 Standard Atmosphere model.	The output at several altitudes is compared to reference values provided by the developer of this model (NOAA, 1976). Verified also by using the TUDAT internal unit test.
Dormand-Prince Propagator	Variable step size numerical integrator used to propagate the state of the vehicle to the next time step.	Verified by using the TUDAT internal unit test.
Multi-linear Interpolator	Interpolation function capable of linearly interpolating multi-dimensional data sets.	Verified by using the TUDAT internal unit test.

Table 5.6: List of primary functions extracted from the toolbox TUDAT provided by the Astrodynamics and Space Missions department of the TU Delft with a short description and method of verification.

5.3. System Verification

A necessary step in the development of a useful software tool is to verify that the tool meets all requirement and the output it provides matches reality sufficiently to confidently answer the research question. A functional verification is possible by analysis of the code output and comparison with reference solutions derived manually or obtained through references. However, a proper verification with actual flight data is more difficult due to the lack of actual flight data.

In this Section the attempts to verify major elements of the simulator are discussed. First Missile DATCOM is tested to determine how well it replicates the aerodynamic coefficients of the Apollo CM. Then the reentry simulator is tested by simulating an open-loop Apollo CM reentry from the moon and comparing the result to reference solutions (Mooij, 2015). Finally the guidance algorithm is verified by performing a dispersion analysis and comparing the result with a reference solution published by Ping Lu (Lu, 2008).

5.3.1. Missile DATCOM Verification

As discussed in Chapter 3 the semi-empirical coefficient generator Missile DATCOM is used to generate the aerodynamic coefficient for the reusable upper stage. As the name suggests this coefficient generator is designed to quickly determine the aerodynamic coefficient for missiles and other type of munition. The accuracy of Missile DATCOM is shown to lie within 25% of windtunnel data for conventional missiles with decreasing accuracy for more unconventional vehicle shapes (Abevnayaka and Agon, 2013).

Unlike missiles the Apollo capsule and the reusable upper stage are blunt bodies. Since Missile DATCOM exhibits that diminishing accuracy for vehicle not shaped like a missile, its accuracy for this study needs to be further analyzed. This is done by generating the aerodynamic coefficients for the Apollo CM with the dimensions shown in Figure 2.9 and comparing it to data available in literature (McNary, 1965; Weiland, 2014).

In Figure 5.4 the drag, lift, and pitch moment coefficient for the Apollo CM generated by Missile DATCOM at Mach 10 is plotted together with windtunnel data from experiments performed during the development of the Apollo CM (McNary, 1965).

While the lift coefficient provided by Missile DATCOM matches the experimental data well and only diverges gradually with increasing angle of attack the other two coefficients do not show much overlap. The drag coefficients have closely matching shapes, but the output of Missiles DATCOM is shifted

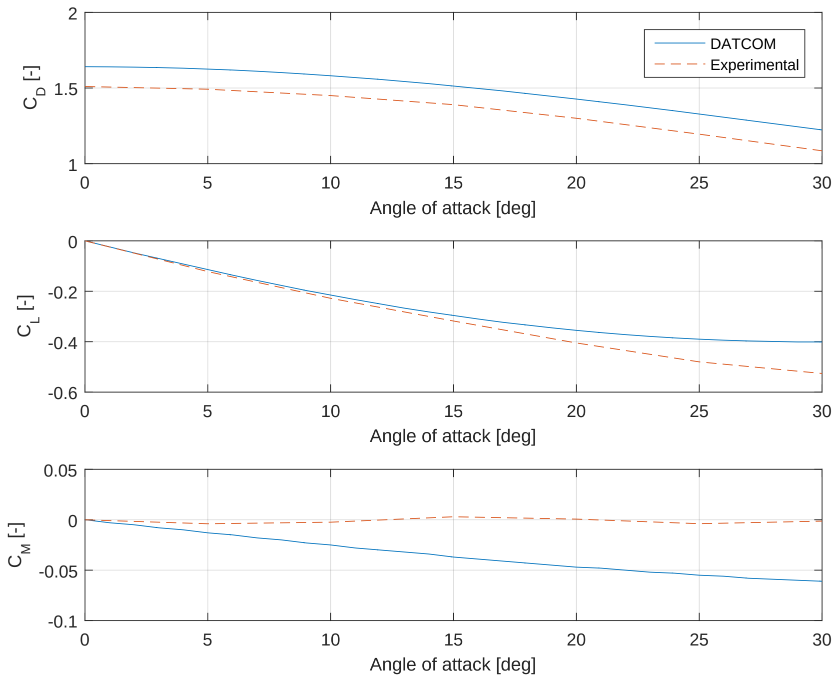

Figure 5.4: Relation between the Earth-centered inertial, Earth-centered fixed, and vehicle-carried vertical frame (Mooij, 2015).

upwards by 0.14 with respect to the experimental data and therefore overestimate the drag by about 10%. The pitch moment coefficients start of from 0, since in both cases a mass symmetric vehicle is assumed. However, right away both values diverge and while the Missile DATCOM data directly drops into the second quadrant in a continuous curve the experimental data jumps around the x-axis.

The pitch moment coefficient at a number of different Mach numbers is again plotted in Figure 5.5(a) with the data generated by Missile DATCOM on top and the experimental data on the bottom.

The Missile DATCOM output shows a similar shape with only slight changes at different Mach number. The experimental data on the other hand shows a more erratic behavior with the potential of instability at certain combinations of Mach number and angle of attack.

To further gain insight into the validity of either results a third set of pitch moment coefficient data is given in Figure 5.5(b) obtained form CFD analysis of the Apollo capsule (Weiland, 2014). Note that in this figure the mass symmetry of the actual Apollo CM is taken into account leading to a passive trim angle at the point where the pitch moment coefficient graphs cross the x-axis.

While a clear trend is also visible here similar to the output of Missile DATCOM this figure shows more pronounced shifts in the pitch moment coefficients with changing Mach number. The different in the value of the pitch moment coefficient in Figure 5.5(b) of 0.05 - 0.065 across the $30°$ range is close to the value found by Missile DATCOM of 0.06.

Given the relative good accuracy in the lift and drag coefficient results as well as the similar pitch moment coefficient compared to CFD solutions Missile DATCOM is deemed sufficiently accurate and remains the most practical tool for the preliminary concept analysis at hand.

5.3.2. Dynamics Verification

In Chapter 3 a mathematical model for the reentry of a vehicle is presented. To verify the implementation of that model the simulator is tested by simulating a passive reentry and descent of the Apollo capsule from a lunar return trajectory without any control input. The result is compared to a reference trajectory with the initial conditions given in Table 5.7 (Mooij, 2015). To match the inputs as much as possible the same set of aerodynamic coefficients are used (McNary, 1965; Mooij, 2015).

The attitude as function of time found using the model presented in Chapter 3 is given in Figure 5.6(a) with the reference for comparison shown on its right in Figure 5.6(b) (Mooij, 2015).

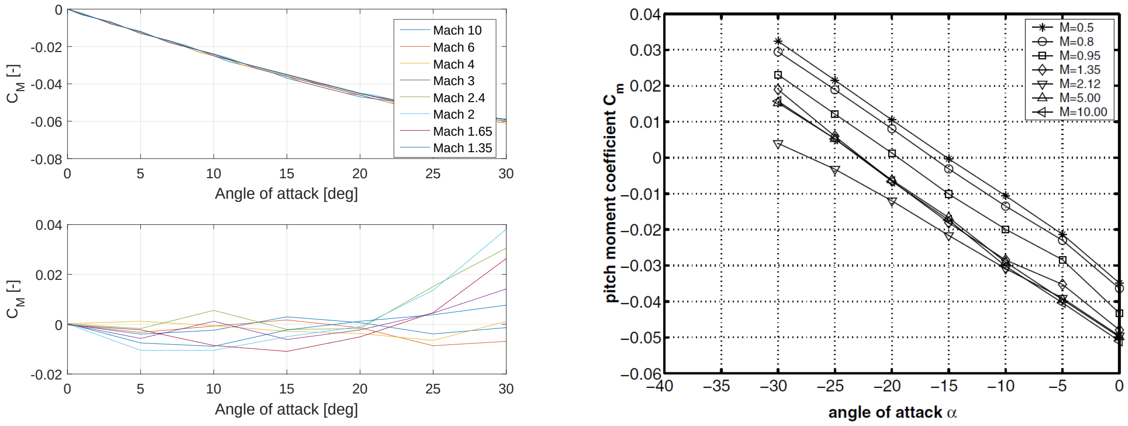

(a) Missile DATCOM(top) vs. experimental data(bottom) (McNary, 1965).

(b) CFD data provided by Weiland (Weiland, 2014).

Figure 5.5: Pitch moment coefficients of the Apollo CM obtained from Missile DATCOM, windtunnel experiments, and CFD analysis.

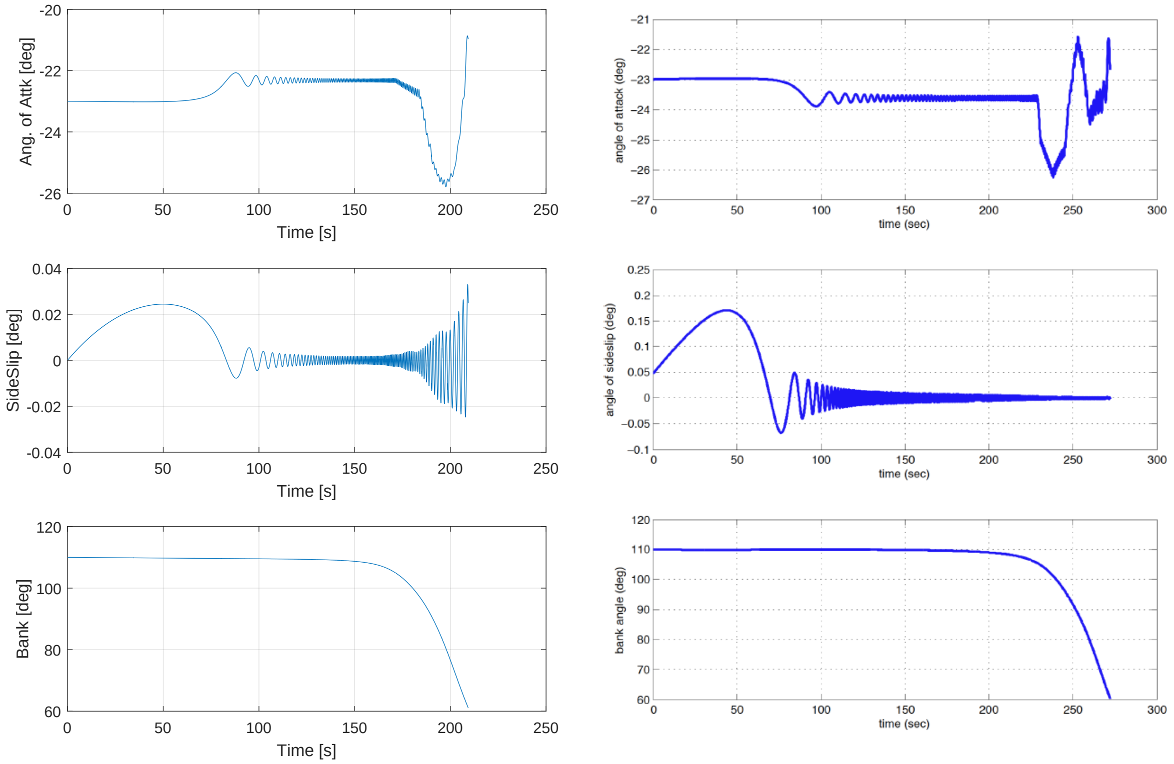

(a) Attitude of the Apollo CM during reentry produced by the simulator.

(b) Attitude of the Apollo CM during reentry as found in the reference (Mooij, 2015).

Figure 5.6: Angle of attack, side-slip, and bank angle as a function of time of the Apollo CM during passive reentry from a lunar return trajectory.

Initial condition	Value
Latitude*	$0.0°$
Longitude*	$-90.0°$
Velocity	11.0 km/s
Altitude	220.0 km
Flight-path angle	$-9.536°$
Heading*	$0.0°$
Angle of attack	$23.0°$
Side-slip angle	$0.0°$
Bank angle	$110.0°$
Roll rate	$-0.013378°/s$
Pitch rate	$0.015658°/s$
Yaw rate	$-0.043446°/s$
Vehicle mass	4976.0 kg
I_{xx}	$5617.605456\ \mathrm{kg/m^2}$
I_{yy}	$4454.623056\ \mathrm{kg/m^2}$
I_{zz}	$4454.80176\ \mathrm{kg/m^2}$
$I_{xz} = I_{zx}$	$1751.99984\ \mathrm{kg/m^2}$
$I_{yz} = I_{zy} = I_{yx} = I_{xy}$	$0.0\ \mathrm{kg/m^2}$

Table 5.7: Initial conditions used for a open-loop entry simulation of the Apollo CM from a lunar return trajectory (Mooij, 2015). The values for the parameters marked with a * are assumed.

The plots show some distinct discrepancies between the two solutions. First the trim angle of attack seems to differ by $1°$ between Figure 5.6(a) at $22.5°$ and Figure 5.6(b) at $23.5°$.

To provide a second verification source for assessing the validity of the simulation Missile DATCOM is used. Missile DATCOM is capable of taking the location of the center of mass into account when calculating the pitch moment coefficient. The Missile DATCOM output file for this case is given in Appendix B and shows a trim angle of attack of $-22°$ at Mach 10. Using an identical but mass symmetric aerodynamic model for the simulation and the same shift in the center of mass in the input file for the simulator yields the results in Figure 5.7. Missile DATCOM confirms the trim angle of attack of exactly $-22°$ at Mach 10.

During the analysis of Figure 5.7 a possible bug in Missile DATCOM was discovered where the aerodynamic coefficients suddenly diverge rapidly and drag the attitude with it. This phenomena is visible at the end of the graph. This sharp increase always seems to occur at Mach 1.1 irrespective of the vehicle's shape and angle of attack. To avoid these anomalous values the terminal velocity for all simulations using Missile DATCOM coefficients is set to 400 m/s.

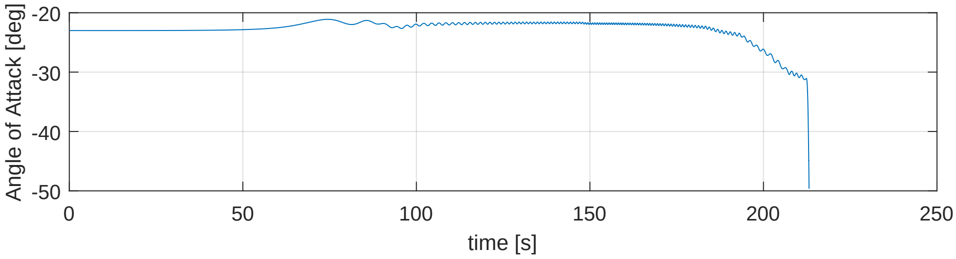

Figure 5.7: Angle of attack of the Apollo CM reentering from a lunar return trajectory using the aerodynamic coefficients generated with Missile DATCOM.

A second discrepancy observed in Figure 5.6 is the magnitude of the deflection of the side-slip angle of just $0.025°$ compared to the reference trajectory of $0.175°$. Furthermore, the magnitude of the side-slip oscillation is first damped and then increases again towards the end of the trajectory. Such a behavior can be explained by the changes in dynamic pressure over the course of the flight. First a rapidly increasing dynamic pressure increases the aerodynamic yaw moment, which stops and reverses the yaw motion more quickly at every successive osculation. The same dynamics applies in reverse as the dynamic pressure drops again towards the end of the flight and the aerodynamic yaw

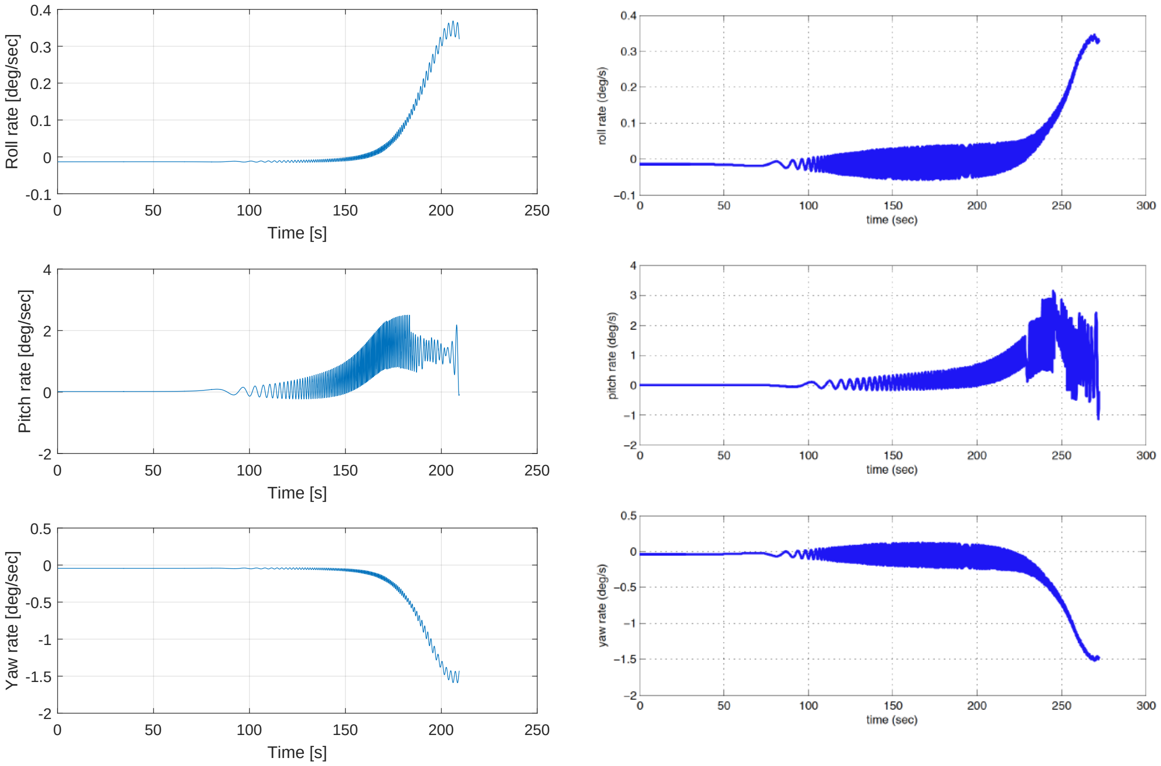

(a) Angular rates during reentry.

(b) Angular rates during reentry as given in the reference (Mooij, 2015).

Figure 5.8: Angular rates as function of flight time past entry interface comparison between the simulator output and the reference (Mooij, 2015).

moment decreases. There the direction of the yaw motion is reversed more slowly on each subsequent oscillation, which increases the amplitude again.

However, no amplitude increase is visible towards the end of the flight in the reference plot of the side-slip angle. The reason for the absence of this increase in amplitude in the reference plot could not be determined and suggests some form of dampening effect in addition to the impact of the change in dynamic pressure on the attitude dynamics.

In Figure 5.8 the angular rate history of the Apollo CM is compared to the reference solution. In this case the angular rates match the reference well in terms of maximum and overall direction. The apparent discrepancies here are the oscillation amplitudes, especially around half-way into the flight, where the reference solution shows overall higher short-term amplitudes. Furthermore the pitch rate does not reach the same maximum as in the reference, but is reasonably close considering the differences in the short term oscillations.

One difference between the simulation and reference trajectory present in all the plots so far is the difference in flight time until the terminal condition is reached. A velocity of $300\ \mathrm{m/s}$ is reached within 275 seconds in the reference while the simulator reaches the terminal condition in 210 seconds. This can only mean that the Apollo CM is decelerating faster in the simulation compared to the reference. This fact is confirmed by Figure 5.9(a), which shows the altitude of the vehicle as a function of G-load and airspeed. Figure 5.9(b) shows the same graph with plots of the reference trajectory.

The reference trajectory shows a peek deceleration of 18 g while the Apollo CM experiences a peek of nearly 30 g according to the simulation results. The magnitude of the aerodynamic forces acting on the vehicle is very sensitive to small direct or indirect variations in the initial condition and especially inaccuracies in the aerodynamics. This sensitivity arises from the exponential relationship of the air density with altitude as well as the quadratic dependency of aerodynamic forces on airspeed. Hence the more time the vehicle spends in the higher atmosphere the more velocity it can bleed of at a lower air density and avoids a combination of a high air density and a high airspeed resulting in higher G-loads.

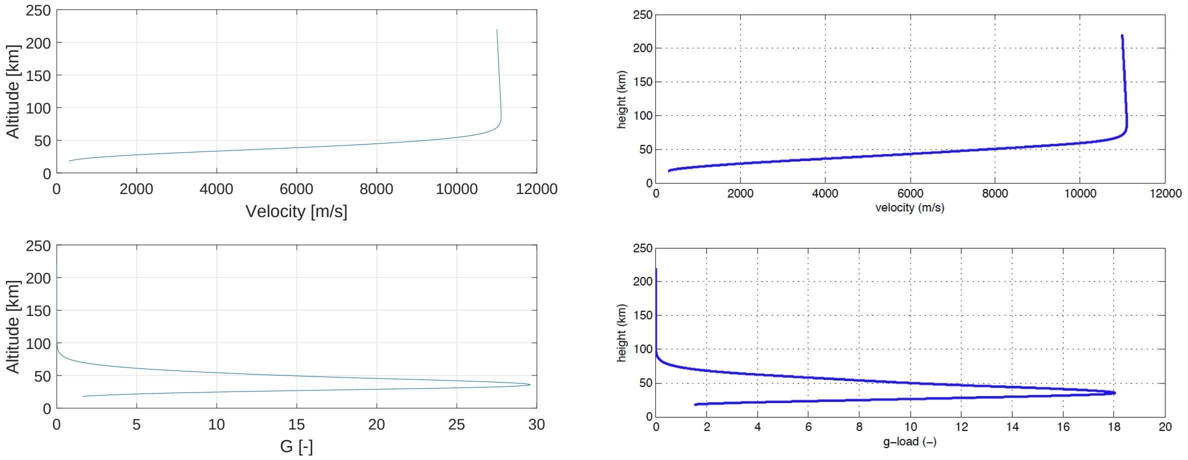

(a) Apollo CM entry simulation by the author.

(b) Apollo CM entry simulation by Mooij (Mooij, 2015).

Figure 5.9: Apollo CM lunar return entry flight profile comparison between the simulator output and the reference (Mooij, 2015).

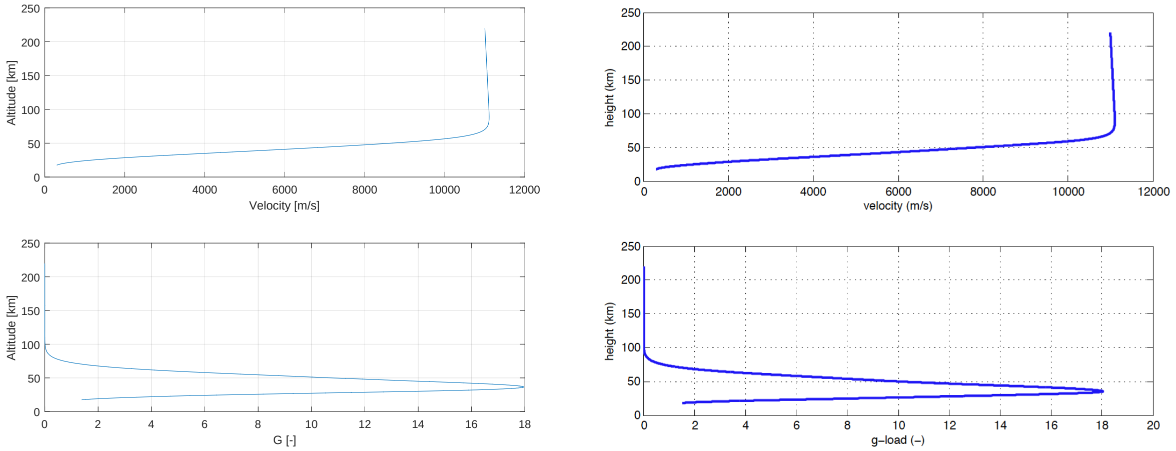

(a) Apollo CM entry simulation by the author.

(b) Apollo CM entry simulation by Mooij (Mooij, 2015).

Figure 5.10: Apollo CM lunar return entry flight profile comparison between the simulator output using a heading angle of $31.5°$ and the reference (Mooij, 2015).

Hence a small difference in density causes a small difference in the drag, which causes a difference in velocity. The difference in velocity further increases the difference in the drag acceleration. Furthermore the velocity variation ultimately leads to an altitude separation, which also further divides the two trajectories. All these errors are propagated and lead to relatively large differences in the outcome despite small initial variations.

To illustrate the sensitivity of the trajectory to the initial conditions a different heading of $31.5°$ is used. The heading is linked to the trajectory through the J_2 harmonic and the fact that the Earth is modeled as oblate spheroid, which in turn has a slight effect on the altitude above Earth's surface used for the atmosphere model. This introduces slight differences in the simulation, which results in the trajectory shown in Figure 5.10. The heading is chosen such that it would result in a perfect match with the reference trajectory.

A second set of reference computations were provided as raw data[1] to compare the variables directly and are plotted against the simulation results in Figure 5.11. The simulation in this case is truncated at 170 seconds of flight time. Here we see that the deceleration given in the top plot is initially identical and starts to diverge as the interaction with the atmosphere increases. The end points of

---

[1] Provided by Dr. Erwin Mooij during face-to-face communication

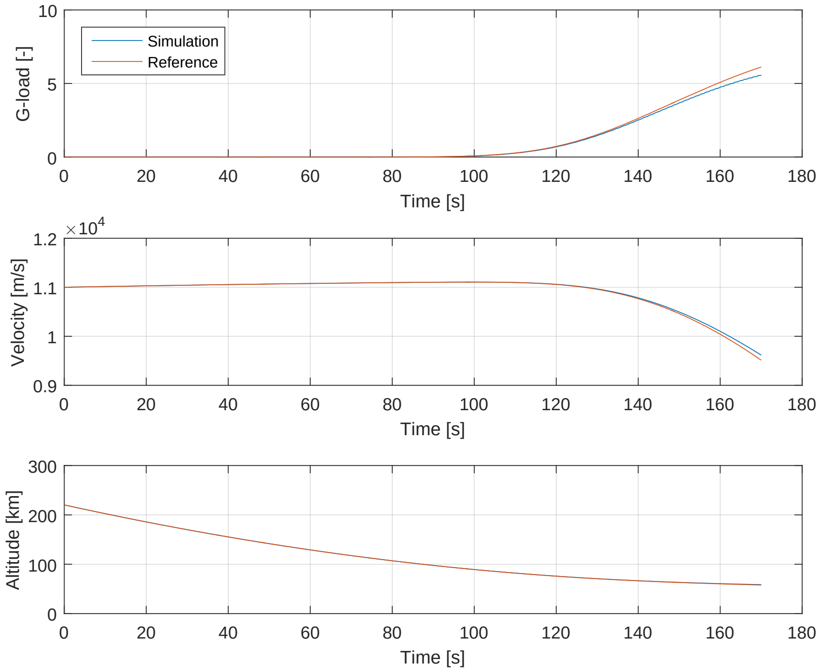

Figure 5.11: Direct comparison between the simulation result and another set of reference solution.

both G-load plots as well as intermediate points are verified to correctly correspond to the aerodynamic deceleration expected at the altitude and velocity given in the bottom two plots.

Sources for the variations observed in Figure 5.9 could be a different initial position and heading, which can have a significant effect on the trajectory due to Earth's rotation and the J_2-effect. Furthermore, small discrepancies in the air temperature are found when the data plotted in Figure 5.11 was analyzed. This discrepancy is due to the use of different atmosphere models.

But small differences in the intermediate solutions of the integration can also arise from the choice of numerical integrator or computation setup. This can also lead to a divergence of results due to the mechanism explained earlier.

This mechanism also effects real reentry vehicles as well and can cause deviations of several kilometers due to navigation uncertainties or variations in the atmosphere. This is the reason for the large landing ellipses for uncontrolled reentry vehicle such as the Mars Exploration Rovers and stresses the importance of dispersion analyses especially for open-loop entries (Knocke et al., 2004).

The maximum execution time experienced with the simulator with active guidance is always less then 20 seconds, which is sufficiently low to satisfy the execution-time requirement and allow for a 500 run dispersion analysis in a practical time frame.

5.3.3. Guidance Algorithm Verification

Just like with the reentry simulation the guidance algorithm is verified by inspection and by comparison with a reference solution. For this again the solution found by Lu is used as reference. A nominal reentry simulation and a dispersion analysis are performed using the same initial conditions and uncertainties as used by Lu (Lu, 2008). The initial condition were either taken as stated in the text or inferred from plots in his paper. A comparison of the reference results and the simulator output are given in Figure 5.12.

The solution found by the guidance algorithm are very similar to the results found by Lu with the largest discrepancy found towards the end of the flight, where the aerodynamic coefficients used in the 6 degree-of-freedom simulation become more erratic while Lu used a 3 degree-of-freedom simulation with constant aerodynamic coefficients. The altitude-velocity plot as well as the plot showing the ground track of the vehicle are also matching each other closely with small differences in the last part of the

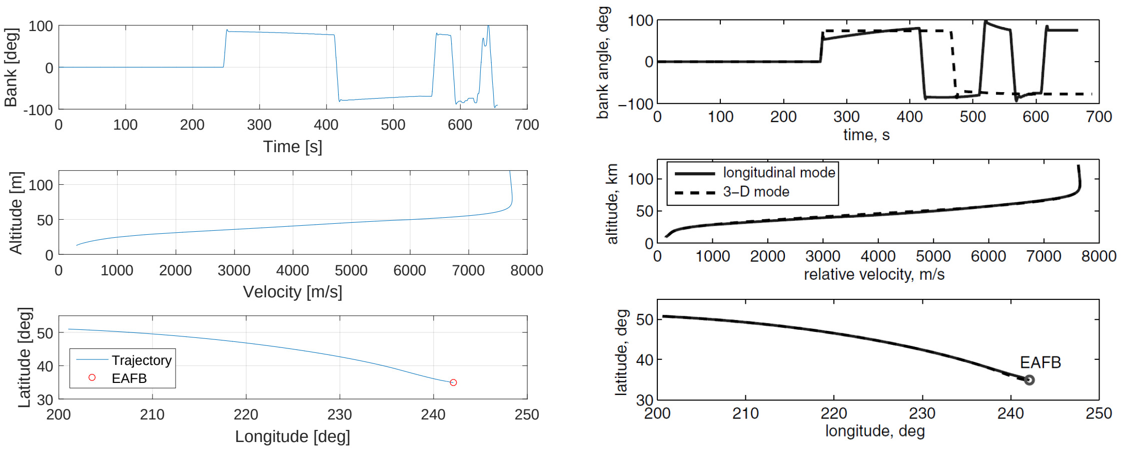

(a) Nominal trajectory of the Apollo CM returning from ISS as found by the author.

(b) Nominal trajectory of an CEV returning from ISS as given by Lu (Lu, 2008).

Figure 5.12: Comparison of the nominal trajectory established by the guidance algorithm of the author and Lu (Lu, 2008).

Variable	3σ/Range	Distribution
Initial longitude [deg]	$0.59°$	Normal
Initial latitude [deg]	$0.66°$	Normal
Initial velocity [m/s]	0.41	Normal
Initial flight-path angle [deg]	$0.023°$	Normal
Initial heading [deg]	$0.39°$	Normal
Atmospheric density	$\pm 10\%$	Uniform
Drag Coefficient	± 0.06	Uniform
Lift Coefficient	± 0.03	Uniform
Vehicle mass	$\pm 5\%$	Uniform

Table 5.8: Uncertainties used by Lu for a dispersion analysis of the guidance algorithm he proposed for the Orion capsule (Lu, 2008).

trajectory as a result of the fluctuations in the aerodynamic coefficients.

To assess the robustness of the guidance algorithm a dispersion analysis is performed, which introduces random variations in the initial conditions, the vehicle properties, and air density that are expected to occur during development and operation of the vehicle. This is to ensure that the algorithm can still guide the vehicle to the target site despite off-nominal conditions. The uncertainties used by Lu to test his version of the guidance algorithm are summarized in Table 5.8 (Lu, 2008).

For the purpose of verifying the algorithm presented in Section 4.1 and comparisons with the results from Lu the same uncertainties are applied. Using those randomized variables and running 500 simulations yields the scatter plot of the final position of the vehicle in Figure 5.13(a). For comparison the scatter plot produced by Lu is shown in Figure 5.13(b). To further test the robustness of the guidance algorithm the uncertainties in the aerodynamic coefficients are doubled and the resulting points are shown in the same plot by a different symbol.

While the terminal points mostly remain within a 5 km radius of the target area the spread observed in Figure 5.13(a) is higher compared to the spread in Figure 5.13(b) with a mean miss distance of 1.49 km compared to a mean miss distance of 0.945 km. Doubling the uncertainty range of the aerodynamic coefficients yields an average miss distance of 1.54 km.

The approximately half a kilometer difference as well as the different pattern of the terminal points may be explained by differences in the models used, such as a constant lift-to-drag ratio used by Lu compared to the interpolated data of aerodynamic coefficients used in the simulator. The reference vehicle used by Lu is the Orion capsule, which is here compared to the reentry of the Apollo capsule for which data is more readily available. As noted earlier relatively small difference in these and other

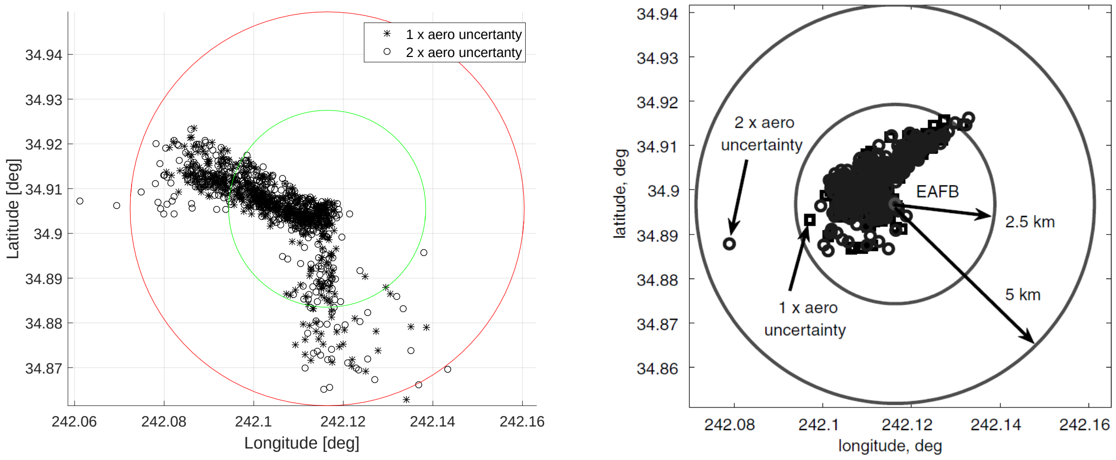

(a) Dispersion analysis of the guided reentry simulation

(b) Dispersion analysis by Lu

Figure 5.13: Dispersion analysis performed to test and verify the guidance algorithm using the uncertainties given by Lu (Lu, 2008).

variables can have a significant influence on the trajectory.

However, overall the guidance shows the ability to consistently guide the vehicle to within 5 km of the target position in the presence of relatively high uncertainties. While a higher accuracy would be desirable for a real vehicle the performance shown here is sufficient for the purpose of this investigation.

5.3.4. Verification Summary

The simulator has consistently shown the capability to reproduce reference solutions with small deviations due to the sensitivity of the reentry environment. The differences can mostly be attributed to differences in the models used to represent the environment and the vehicle, such as the aerodynamic model used for the Apollo capsule compared to the static aerodynamic coefficients used in the reference solution for the Orion capsule in the verification of the guidance module. The guidance nevertheless performed satisfactory by delivering the vehicle consistently within the target area of 5 km and thereby fulfilling its targeting accuracy requirement.

The reentry dynamics simulator can also reproduce the trim attitude predicted by Missile DATCOM and the trajectory as given in the reference open-loop reentry solution. A certain initial heading is used to tune the results and make them match the reference trajectory. The exact initial heading used to generate the reference solution is not known. The difference in the result due to different heading angles highlight the sensitivity of a reentry to the initial conditions and the environment along the trajectory. A second set of reference solutions with matching initial conditions are compared in detail. They show how small differences in the models or even in the computer set-up, such as the precision of the variable used, can introduce a divergence in two different simulations due to the error accumulating effect of numerical integration in general and the amplification effect of that error due to the atmosphere.

In accordance with the requirement for accuracy in the results of the dynamics simulator the errors due to numerical errors or simplifying assumptions is strictly maintained at less then 100 m by inspecting and appropriately designing the various elements.

The error in the results due to uncertainties in the models, such as the atmosphere model or the aerodynamic model, is not specified on purpose as these elements can not be designed for, but only estimated.

The semi-empirical coefficient generator Missile DATCOM is verified separately against experimental and CFD data to determine the quality of its output. It yields representative solutions at high mach numbers for the lift and drag coefficients. Its prediction of the moment coefficient is uncertain given the differences in available references. However, the resulting trim angle due to the pitch moment coefficient and the shift in the center of mass for the Apollo capsule is relatively close to values given in various Apollo CM vehicle specifications.

6

Results

The goal of this work is to assess the feasibility of reentering a reusable upper stage safely back into Earth's atmosphere and guiding it to a target location. For this a simulator is developed to test a model of a upper stage in realistic reentry conditions during a nominal mission. In this chapter the results from the reentry simulations are presented. Section 6.1 first discusses the aerodynamic coefficients and static stability of the vehicle calculated using Missile DATCOM. Then the angular dynamics of the only stable vehicle variant is simulated in response to a hypersonic airflow and the results discussed in terms of dynamic stability. Finally, in Section 6.2 the results for a nominal reentry are discussed with the focus on flight behavior, loading, and control. To increase confidence in the results a dispersion analysis is performed with randomized initial state and vehicle characteristics. The miss-distances of every terminal point as well as the peak loads are presented in scatter plots. Finally, results for reentries from a geostationary transfer orbit are discussed to assess the viability of returning a reusable upper stage from one of the most popular orbital destinations back to Earth.

6.1. Upper Stage Aerodynamic Stability

The attitude stability of a reentry vehicle in an airstream is primarily governed by its aerodynamic coefficients, especially the aerodynamic moment coefficients. The aerodynamic forces and moments acting on the upper stage are caused by an asymmetric airflow around the vehicle, which create pressure on the surface and force couples around the center of mass of the vehicle. In this section the aerodynamic force and moment coefficients for the reusable upper stage are presented as generated by Missile DATCOM.

6.1.1. Aerodynamic Coefficients and Static Stability

The lift and drag coefficients of the upper stage are analyzed, since they provide the forces that control the trajectory and are therefore critical indicators for the trajectory control authority available to the reusable upper stage. The lift and drag coefficients of the baseline upper stage generated by Missile DATCOM are given in Figure 6.1. Note again that a symmetric vehicle is studied here with the center of mass centered on the longitudinal axis of the vehicle.

From this figure it is clear that the lift-to-drag ratio is relatively low even compared to non-winged ballistic capsules such as the Apollo CM. Furthermore, the lift coefficient shows a peculiar behavior by starting at zero with a negative but increasing slope until an angle of attack of 15° is reached. There the slope becomes positive and the lift coefficient continues to increase past zero lift at an angle of attack slightly larger than 30°. The curve then continues to increase further into the first quadrant. This shape of the lift coefficient curve can be explained by the geometry of the vehicle itself and is illustrated in Figure 6.2.

Here, one can see that at small angles of attack the relatively flat heat shield deflects most of the incoming air upwards, with a fraction of the airflow hitting the tank on the opposite side of the vehicle. The deflected airflow is illustrated as curved orange arrows. With increasing angle of attack the fraction of the air hitting the side wall of the tank increases while less of the heat shield area is projected into the flow. The resulting forces on the vehicle from both deflections are opposite to each other and shown

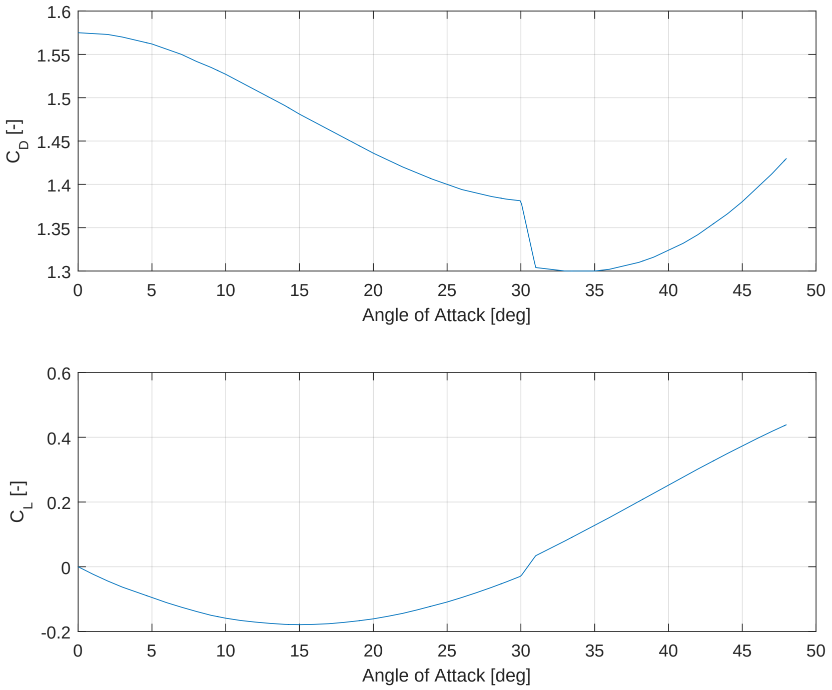

Figure 6.1: Drag and lift coefficient as function of the angle of attack of the baseline reusable upper stage generated using Missile DATCOM.

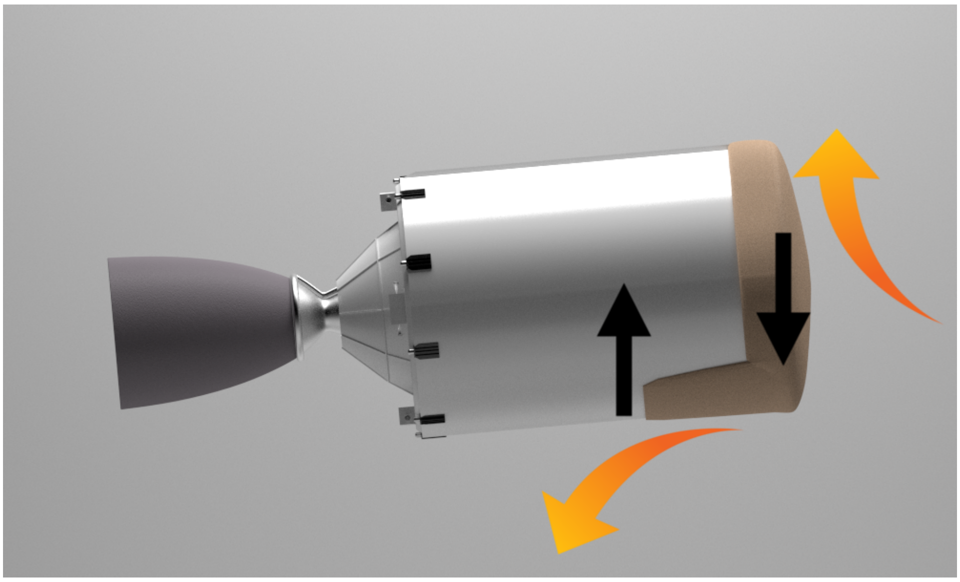

Figure 6.2: Airflow deflection from the vehicle at an angle of attack depicted as orange curved arrows with the corresponding reaction forces in black straight arrows.

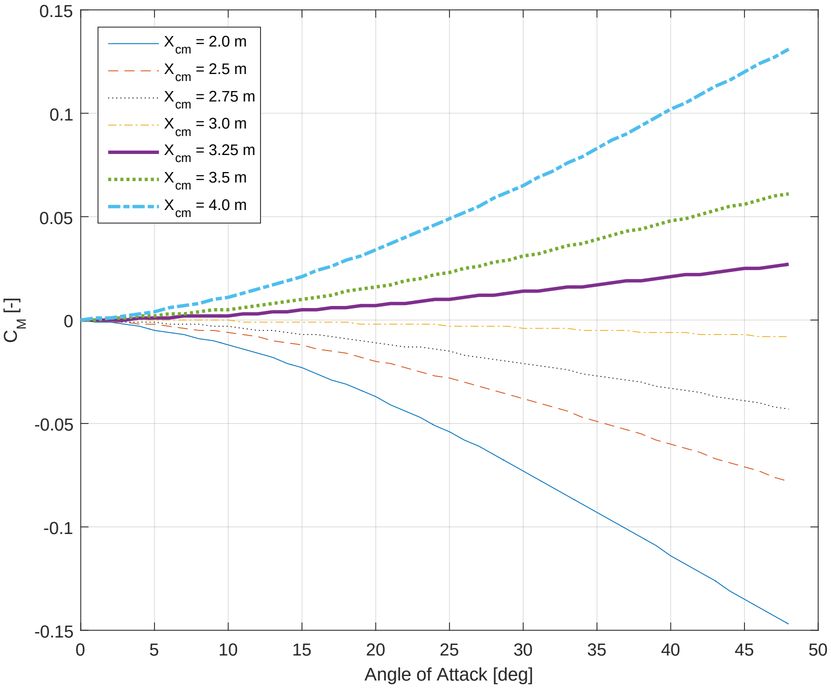

Figure 6.3: Moment coefficients as functions of the angle of attack of the baseline reusable upper stage with different center-of-mass locations along its longitudinal axis.

as straight black arrows. Hence, while at small angle of attack the lift is primarily produced by the heat shield the contribution of the side walls increase with increasing angle of attack. That force counteracts the force acting on the heat shield until it surpass it and reverses the sign of the lift coefficient at around $30°$ angle of attack.

The moment coefficient is the driving factor in the stability of the vehicle. Since the vehicle under consideration is symmetric along its longitudinal axis in shape and mass distribution the same moment coefficient profile applies to both pitch and yaw while the roll moment at any attitude with respect to the flow is always zero. The pitch moment coefficient as a function of total angle of attack of the reusable upper stage is shown in Figure 6.3 for several different center-of-mass locations along the longitudinal axis of the vehicle.

This figure unsurprisingly shows an increase in instability the further aft the center of mass is located. As described in Section 3.4 and shown in Figure 2.10 the center of mass of the vehicle is estimated to be located on average 3.3 m from the nose, which would make the vehicle clearly unstable.

The second vehicle configuration shown in Figure 2.11(b), which is believed to improve the stability compared to the baseline configuration, is the vehicle with extended aft skirt. The added surface area behind the center of mass pushes the resultant center of pressure to the back and counteracts the moment created by the forces ahead of the center of mass. This seems indeed to be the case according to Figure 6.5, which shows the pitch moment coefficient as function of angle of attach for a vehicle with a 7 m long body compared to the 5.5 m body of the baseline configuration using the same center-of-mass locations relative to the front. The aft skirt extension seems to be effective at bringing the moment coefficients curves down substantially and makes the vehicle statically stable for all but the extreme center-of-mass locations close to 4 m from the nose. However, this approach is also limited by practical consideration such as available space between the stages and a window for the radiative cooling of the nozzle.

In Figure 6.6 the lift-to-drag of the baseline configuration is compared to the vehicle configuration with aft skirt. This plot also highlights another drawback of having that aft skirt. While the skirt improves the lift-to-drag figures of the vehicle at large angles of attack it actually reduces it at the low angle of attack range at which the vehicle is intended to fly.

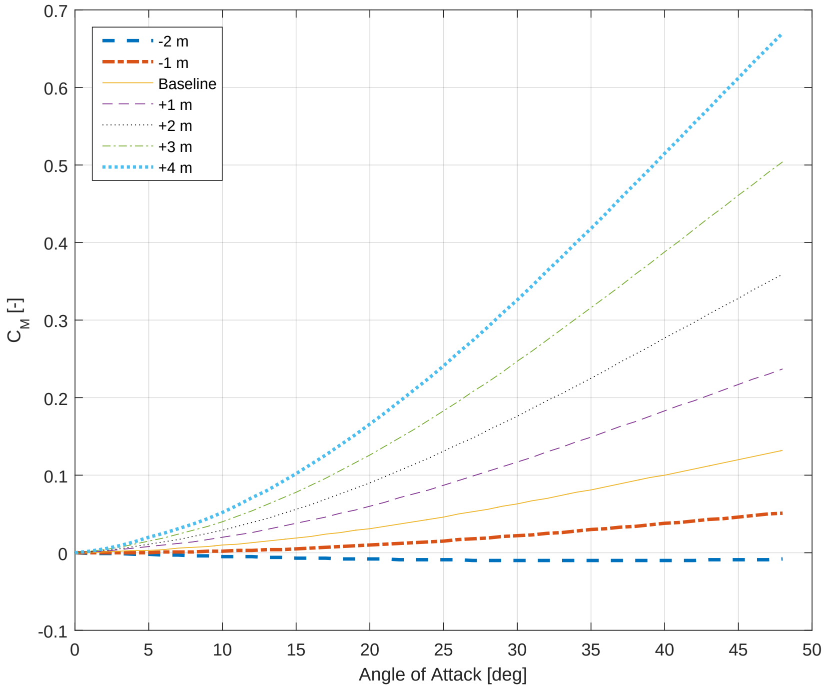

Figure 6.4: Moment coefficients as functions of the angle of attack of the baseline upper stage of different lengths. The center of mass is kept fixed relative to the aft part and engine of the rocket stage.

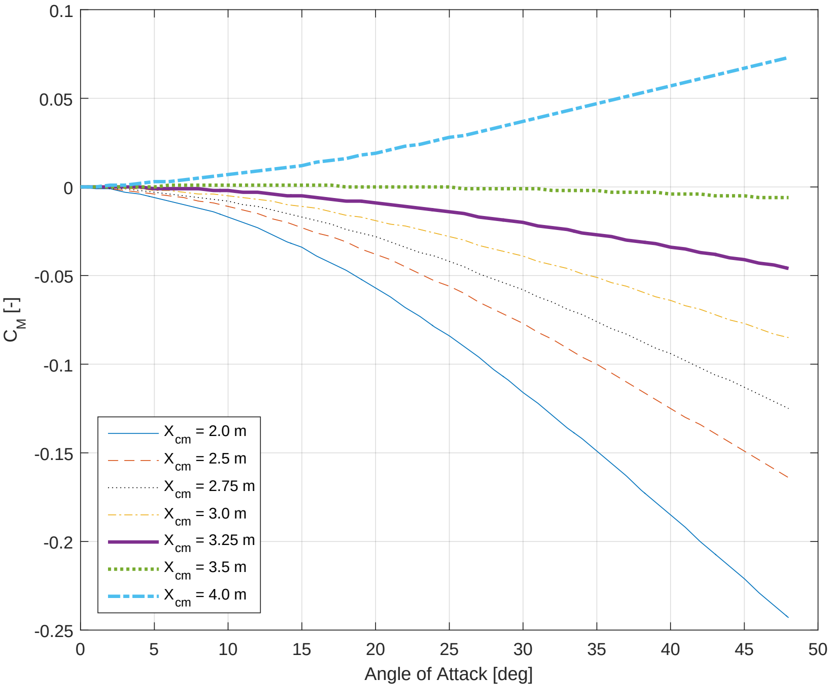

Figure 6.5: Moment coefficients as functions of the angle of attack of the reusable upper stage with aft skirt with different center-of-mass locations along the vehicles longitudinal axis.

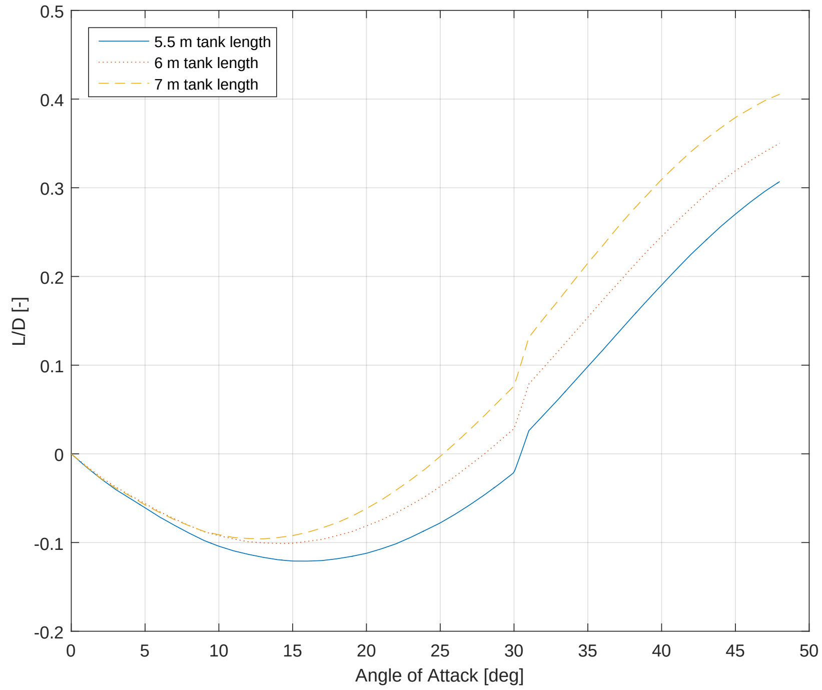

Figure 6.6: Comparison of lift-to-drag ratios between the basline vehicle and the upper stage with 0.5 m, and 1.5 m aft skirt.

The third and ultimately chosen configuration is the vehicle with passive flaps for stabilization. As described in Section 2.5.2 it uses the aerodynamic coefficients generated for the baseline together with flaps to arrive at a stable vehicle model. The flaps ensure that the vehicle is stable for all center-of-mass locations and for a wide range of angles of attack, which is not given for the upper stage variant with extended aft. The stability of this configuration is demonstrated by simulating the angular dynamics of the vehicle in a hypersonic flow. The results are discussed in the following section.

6.1.2. Dynamic Response in a Hypersonic Airflow

To study the dynamic response of the vehicle with flaps to a deflection away from the trim attitude the vehicle's angular motion is simulated in a Mach 10 airflow. The flaps are deflected by $20°$. The center of mass is shifted along the Z-axis in the body frame of the vehicle to generate a passive trim angle of attack. The angle of attack and side-slip angle are turned away from the stable position by $\pm 3°$ and $\pm 6°$. The attitude response is plotted in Figure 6.7.

The plots show a stable oscillation around the trim attitude with constant amplitude at the level of initial offset. Dampening coefficients are not taken into account in the model and assumed to be small anyway, which would otherwise slowly reduce the amplitude of the oscillation (Mooij, 2015). Overall the upper stage equipped with flaps shows a stable behavior in a constant airflow.

6.2. Guided Entry and Descent Performance

To fully assess the viability of a reusable upper stage a guided entry from low Earth orbit is simulated. Such a simulation gives a comprehensive insight into the performance of a reentry vehicle in terms of landing accuracy, maneuverability, and stability across a realistic range of flight regimes. This also allows the determination of propellant consumption, heat load, and mechanical loading on the vehicle. First the result of a nominal reentry simulation is presented. To test the robustness of the design a sensitivity analysis is performed, where the initial condition and vehicle characteristics are randomized within a certain uncertainty range. Finally, a reentry from a geostationary transfer orbit is simulated and analyzed.

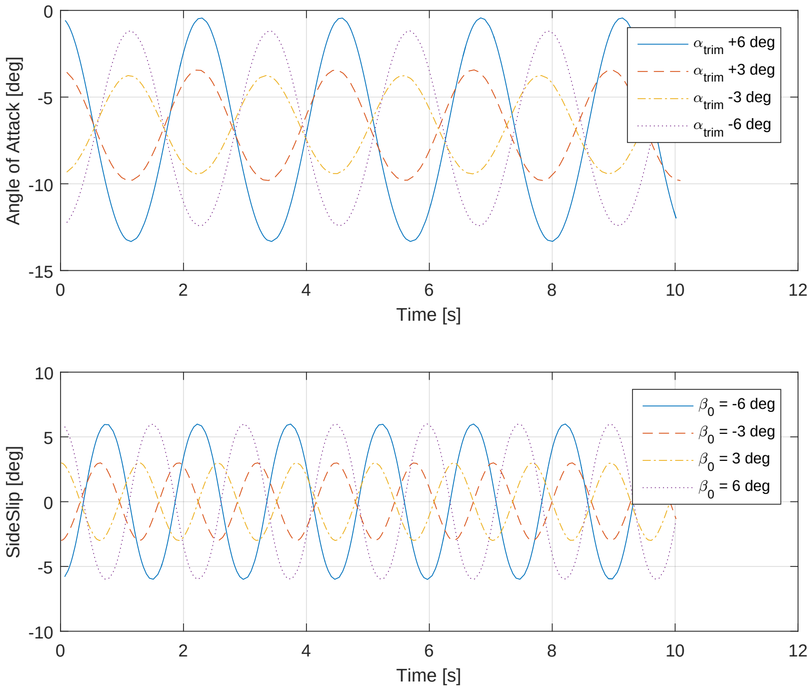

Figure 6.7: Vehicle's angle of attack and side-slip response to 3°, and 6° deflections to ether side from the passive trim angle in a Mach 10 airflow.

6.2.1. Nominal Mission

After delivering the satellite into low Earth orbit and performing the deorbit burn the nominal reentry starts with the vehicle at the entry interface at 120 km altitude descending with an airspeed of $7.7\ \mathrm{km/s}$ and a flight-path angle of -3° with respect to the Earth's surface. The vehicle is passively stabilized by the aerodynamic surfaces with a constant deflection angle of 20°. The simulation is terminated when the final velocity of $400\ \mathrm{m/s}$ is reached. The target location is Landing Zone 1 at the Cape Canaveral Air Force base in Florida at 28.48° latitude and 279.46° longitude. Plots of key parameters of the flight are shown in Figures 6.8 - 6.10.

Aerodynamics and stability In Figure 6.8(a) the angle of attack, side-slip angle, and bank angle are plotted as function of elapsed time since entry interface. The vehicle shows a stable attitude with an angle of attack trimmed at around -6.1°. The side-slip angle remains stable at 0°. The bank angle is controlled by the vehicle's guidance and control, indicated by the regular bank reversals and the bank angle adjustments by the guidance.

The spikes in the angle of attack and side-slip angle are caused by the bank reversal maneuver. This coupling is due to the fact that the bank is controlled via the roll of the vehicles body axis, which is not aligned with the aerodynamic frame. Hence, a change in roll has an effect on the angle of attack and side-slip angle as well. This can clearly be seen during the first bank angle correction 10 s into the simulation. This coupling is suppressed by the aerodynamic moments later in the flight keeping the angle of attack and side-slip angle firm in the trimmed position.

At around 300 s into the flight the vehicle enters the low supersonic airspeed range, where the aerodynamic coefficients show a more erratic behavior. The aerodynamic coefficients as a function of time are shown in Figure 6.8(b) with the noisy behavior visible towards the end of the flight. The bump in the drag and lift coefficients at around 110 s into the flight is an artifact caused by a discontinuity in the first derivative at 84 km altitude in the function of the standard atmosphere used within Missile DATCOM.

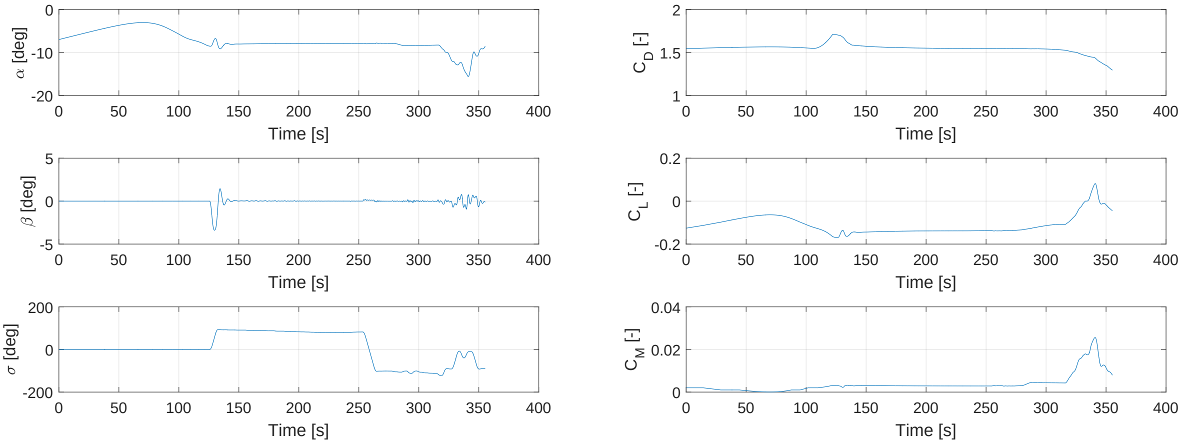

(a) Attitude angles as function of time

(b) Aerodynamic coefficients as function of time

Figure 6.8: Attitude angles and aerodynamic coefficients during a reentry from LEO.

Flight profile and loads In Figure 6.9(a) key flight parameters are plotted against each other and show a relatively steady descent. The acceleration peaks at 40 km with a maximum of 5.75 g.

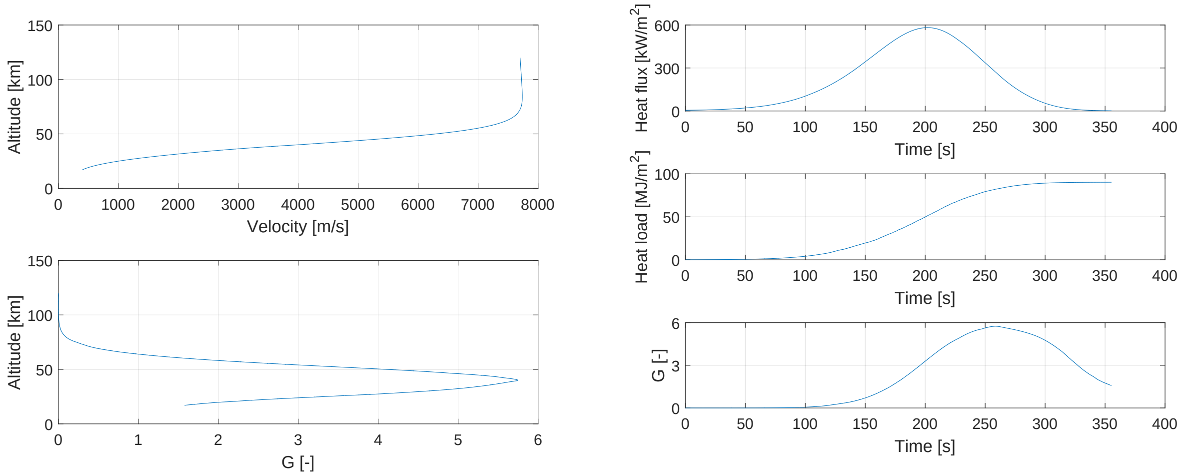

(a) Altitude as function of velocity (top) and G-load (bottom).

(b) Heat flux, total heat load, and G-load as function of time.

Figure 6.9: Flight profile and flight loads during reentry from LEO.

The heat flux and G-loads experienced by the vehicle are given in Figure 6.9(b) and show a behavior typical for atmospheric reentries. The peak G-load occurs slightly after the peak in heat flux, since the G-load is a function of dynamic pressure, which in turn is linearly proportional to the air density and the square of the airspeed. The heat load, however, is proportional to the airspeed cubed but only proportional to the square-root of the air density.

RCS propellant consumption Finally to assess the propellant requirement for steering such a vehicle through reentry and descent an analysis of the applied control moment is performed. The control moments around all three vehicle axis as a function of time are plotted in the bottom graph of Figure 6.10(a) with the top graph showing the angle of attack, side-slip angle, and bank angle.

The spikes in the roll control moment M_X appearing at regular intervals correspond to bank reversal events with the smaller spikes appearing every 10 s indicating guidance updates in the bank angle

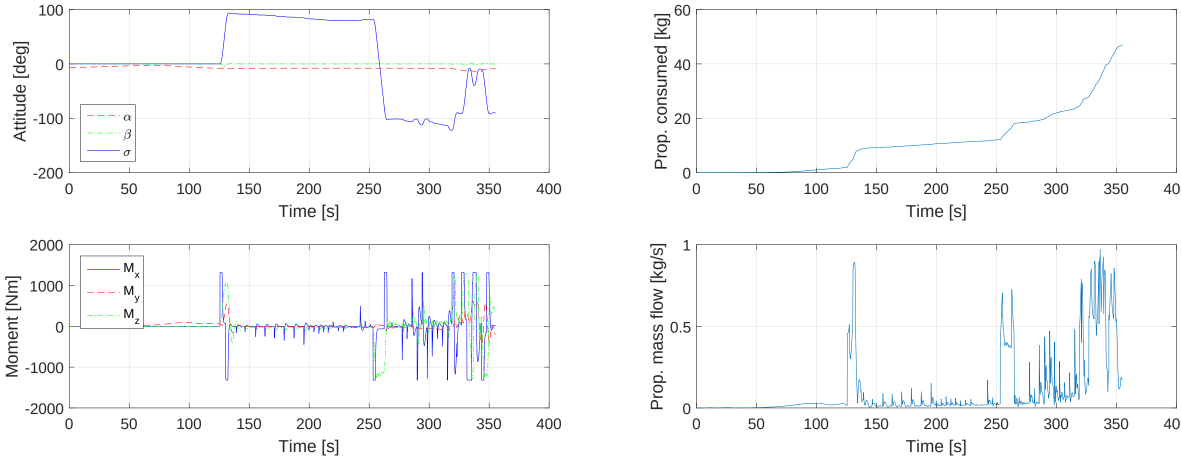

(a) Attitude angles (top) and control moments (bottom) vs time.

(b) Propellant consumption (top) and propellant mass flow (bottom) vs time

Figure 6.10: Plots illustrating the control effort required for steering the vehicle to the target.

magnitude. The pitch and yaw control moment reacts accordingly to dampen out any angular rates.

Using the relation between the control moment and attitude control thruster activation derived in Section 4.2 the total amount of fuel as well as the mass flow can be calculated for every point in time of the flight. Both are given in Figure 6.10(b) as a function of time.

A total propellant mass of 46 kg is consumed for attitude control until the terminal point is reached. In comparison the Apollo capsule consumed 14 kg of propellant from entry interface till drogue parachute deploy (Maynard et al., 1969). There are several possible reasons for the difference.

The erratic bank angle adjustments and attitude rate dampening due to the fluctuating aerodynamic coefficients consume most of the propellant. This may be reduced by terminating bank angle updates close to the terminal point and keeping the bank angle constant. This would make the last part of the trajectory open loop and would introduce a potential error source for an improved propellant economy.

A second explanation for the higher propellant consumption is also the difference in the moment of inertia. Although the reusable upper stage mass derived in Section 3.4 is less then the mass of the Apollo capsule of 4976 kg the moment of inertia around all three axis. The moment of inertia of the Apollo CM is (Mooij, 2015):

$$\mathbf{J}_{Apollo} = \begin{bmatrix} 5617.605 & 0 & 1751.999 \\ 0 & 4454.623 & 0 \\ 1751.999 & 0 & 4454.8018 \end{bmatrix} \text{kg} \cdot \text{m}^2 \tag{6.1}$$

This difference in the moment of inertia is due to more mass being located further away from the center of mass of the upper stage compared to the Apollo CM.

6.2.2. Dispersion Analysis

To gain confidence in the results found from simulating a nominal mission a dispersion analysis is performed. A dispersion analysis introduces uncertainties that are inevitably in any system, such as in this case fluctuations in the atmospheric density due to, for example, seasonal changes or solar activity, or navigation errors. Uncertainties are also present within the vehicle itself, since it does not yet exist. Hence, properties such as mass, mass distribution, or aerodynamic coefficients have to be viewed as estimates at best rather than reliable values.

A sensitivity analysis on the mass and mass distribution was performed and is presented in Section 3.4 to analyze the range of values the mass, center-of-mass location, and moment of inertia can have. The center of mass for a variation of mass distributions are plotted as green dots in Figure 2.10. The resulting variations in the vehicle's mass, moment of inertia, and center of mass are used in the dispersion analysis together with variations in the variables listed in Table 6.1 to assess the effect of

Variable	3σ/Range	Distribution
Longitude [deg]	0.3° (0.9°)	Normal
Latitude [deg]	0.3° (0.6°)	Normal
Airspeed [m/s]	5	Normal
Flight-path angle [deg]	0.05°	Normal
Heading [deg]	0.05°	Normal
Angle of attack [deg]	1.0°	Uniform
Angle of side-slip [deg]	1.0°	Uniform
Atmospheric density (Alt. ≤ 30000 m)	$\pm 10\%$	Uniform
Atmospheric density (Alt. ≤ 50000 m)	$\pm 20\%$	Uniform
Atmospheric density (Alt. > 50000 m)	$\pm 30\%$	Uniform
Atmospheric temperature [K]	$\pm 10\%$	Uniform
Drag Coefficient [−]	$\pm 10\%$	Uniform
Lift Coefficient [−]	$\pm 10\%$	Uniform
Moment Coefficient [−]	$\pm 10\%$	Uniform

Table 6.1: Uncertainties used to test the sensitivity of the outcome of the simulation to variations in the initial conditions and environment.

uncertainties on the reentry and descent performance of the upper stage.

The uncertainties shown in this table are for the most part based on variations used to test the performance of reentry guidance algorithms given in Table 5.8 with some modifications (Lu, 2008). The uncertainties in initial latitude and initial heading are reduced compared to the reference and are more in line with expected orbit injection uncertainties for the Falcon 9 launch vehicle given in Table 2.4. Due to relatively low lift produced by the upper stage compared to Apollo-type capsules it is unable to correct the same heading and latitude error.

Downrange distance is less susceptible to this limitation, since the effect of the pull-up or down is amplified by the increase and decrease air density with changing altitude. Uncertainties in the air density are modeled more accurately by stepping the uncertainty in density based on the data in Figure 3.4. The uncertainty starts with $\pm 10\%$ at see level, increases to $\pm 20\%$ for altitudes above 30 km up to 50 km, where the uncertainty is set to $\pm 30\%$ for altitudes above that. Also the temperature is randomized in addition to the density. Finally, since the upper stage is simulated with six degrees of freedom the angle of attack and side-slip angle are randomized as well to account for any impact a slight off-point can have on the results.

With these randomized variables 500 simulation runs were performed. The resulting terminal point positions with respect to the target are shown in Figure 6.11(a).

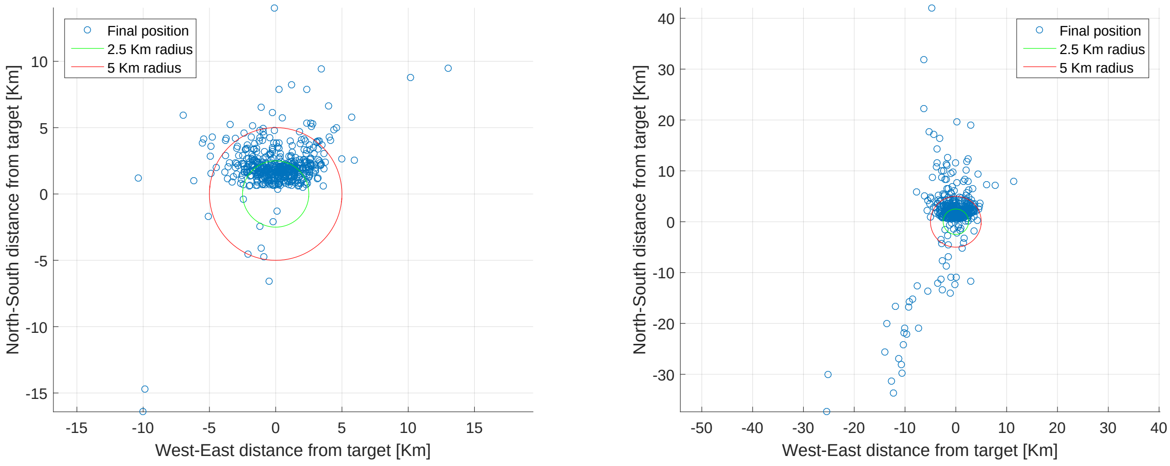

(a) Analysis with small uncertainty in initial position.

(b) Analysis with high uncertainty in initial position.

Figure 6.11: 500 run Monte-Carlo dispersion analysis performed on the reentry of the reusable upper stage from LEO.

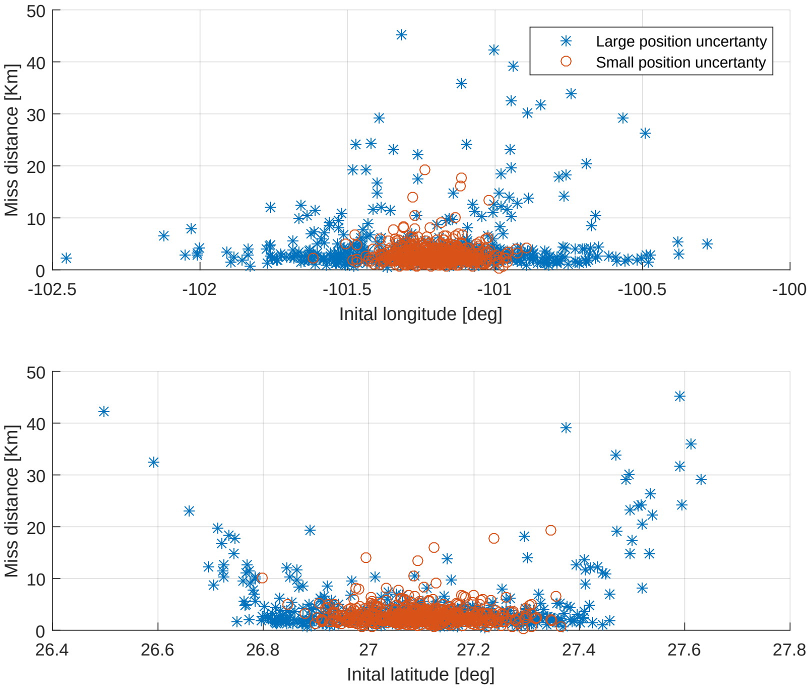

Figure 6.12: Miss distance as a function of longitude in the plot above and latitude on the plot below from the second dispersion analysis with expanded position uncertainty.

Here we see that most of the points are located within 5 km of the target. The average miss distance is 2.63 km with a standard deviation of 1.64 km. To probe the sensitivity of the upper stage to larger inaccuracies in the initial position the standard deviation of the initial longitude and latitude is increased to $0.9°$ and $0.6°$, respectively. Figure 6.11(b) shows the result of that increase in uncertainty. As expected the upper stage is mainly limited in its crossrange capability, which results in the visible spread of the terminal positions to the north and south as the spacecraft flies from west to east. This pattern becomes more clearly visible in Figure 6.12, where the miss distance from the target is plotted as function of initial longitude in the top and as function of initial latitude on the bottom graph.

While the initial longitude shows no clear correlation and appears random a clear pattern is visible in the initial latitude. The points where the limit of the vehicle to correct lateral deviation is reached is clearly visible, where the miss distance suddenly rises linearly at around $26.8°$ and $27.4°$ with increasing deviation in the initial latitude from the nominal value of $27.1°$.

This highlights the need for accurate orbit control and precise reentry burns ahead of the entry interface to ensure it does not deviate too much from the course towards the target site. After passing the entry interface these errors are difficult to correct aerodynamically given the low lift of the upper stage.

A scatter plot of the loads experienced by the vehicle in the 500 simulation runs are shown in Figure 6.13 with the maximum heat flux experienced during the descent for every run shown in the top plot, the total heat load in the center plot, and the maximum G-load in the bottom plot. All loads are plotted as function of miss distance from the target, but the different loads seem random at any distance indicating no obvious relationship.

This makes sense as the load is mostly dependent on the velocity, flight-path angle, and the altitude of the vehicle at any given time. These variables can be controlled by the vertical part of the lift force with respect to the ground. However, the reason for the terminal points furthest away from the target is the lack of crossrange capability to remove the heading error.

To minimize the miss distance to the target the guidance commands the vehicle into a turn. For the sharpest possible turn the vehicle has to bank to the left or right by $90°$, which points the lift vector directly into the turn direction and does therefore not produce particularly high or low loads.

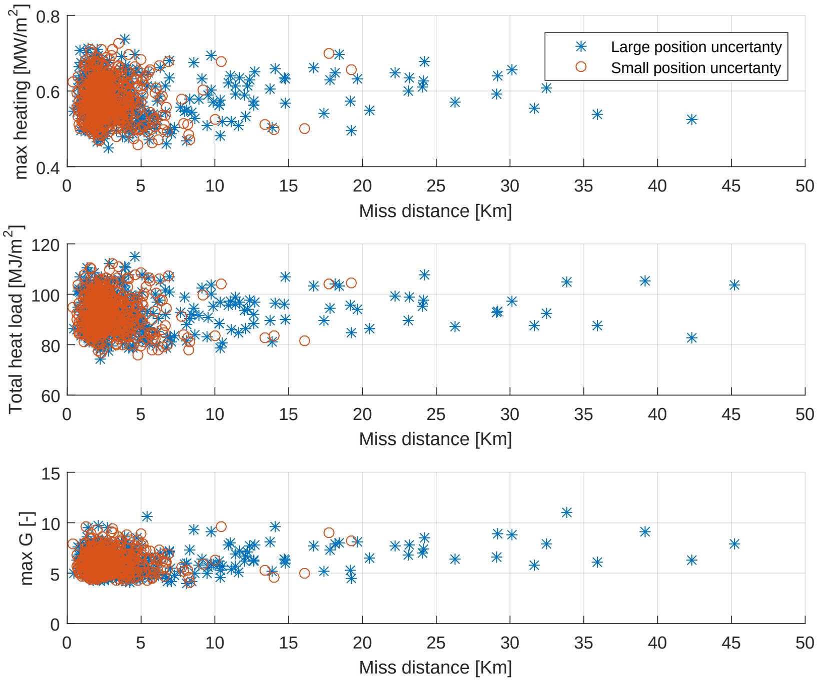

Figure 6.13: Maximum heat and mechanical loads experienced by the vehicle in 500 simulation runs.

The loads are instead influenced by either banking the vehicle fully down or up, thereby controlling the rate of descent of the vehicle into the denser part of the atmosphere. Hence, one would expect to see dependencies between the initial longitude and the loads when increasing where the vehicle would have to use the vertical lift component to control the range.

This is indeed confirmed in Figure 6.14(a) where a trend is noticeable in the maximum G-load plot as function of initial longitude. Varying the initial longitude in this case changes the downrange distance of the vehicle to the target given the nearly eastward trajectory. Hence, the closer the vehicle is to the target the higher the bank angle magnitude and therefore usually the G-loads experienced during descent. The highest G-load experienced by the vehicle in the 500 s simulations is 10 g and the lowest maximum G-load is 3.9 g.

Figure 6.14(b) shows propellant consumption as function of miss distance and also here an interesting relation becomes apparent. The smaller the heading error the higher the propellant consumption. This relationship is due to the number of bank reversals required for trajectories that are heading straight to the target. Trajectories with a large heading error spend more time in a turn to correct the error instead of performing regular reversals to maintain course. The most expansive descent in terms of propellant consumed 57.6 kg of propellant while the cheapest reentry only consumed just 20 kg.

6.2.3. Reentry from Geostationary Transfer Orbit

One of the most common missions for current launch vehicles is launching communication satellites into a geostationary transfer orbit (GTO). In 2014 5 out of 6 launches of the Ariane 5, all 8 launches of the Proton, and 3 out of 6 launches of the Falcon 9 targeted that orbit[1]. Hence, analyzing the reentry performance of a reusable upper stage from a geostationary transfer orbit together with the analysis of the return from low Earth orbit covers most flight conditions a launch vehicle of this type encounters. For the return from a GTO mission Landing Zone 1 is kept as target location as well as the entry interface altitude of 120 km. The initial airspeed is increase to $10.5\ \mathrm{km/s}$ and the flight-path angle is increased to -6°. Figure 6.15 shows the angle of attack, side-slip angle, and bank angle as a function of time for such a return.

---

[1] `http://www.spacelaunchreport.com/log2014.html`

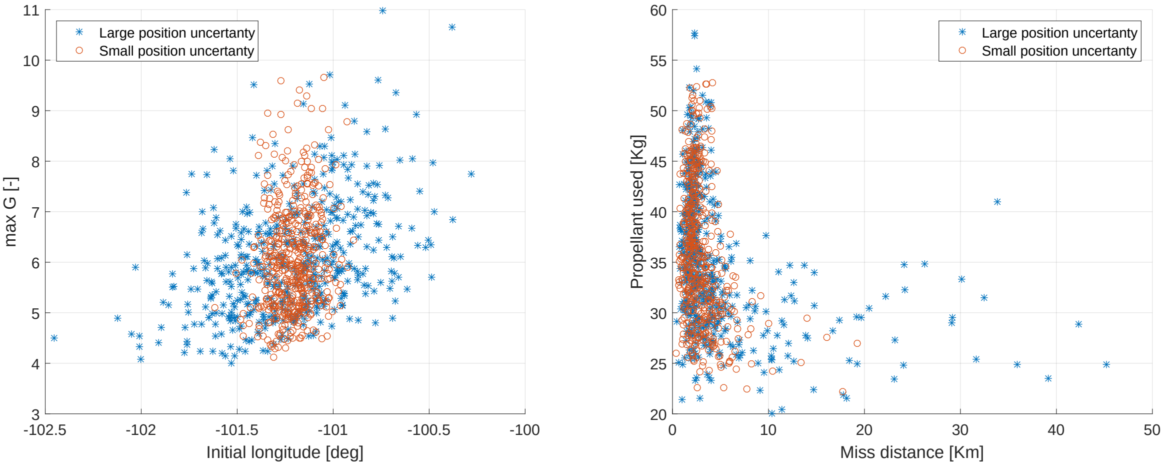

(a) Maximum G-load vs. initial longitude.

(b) Propellant consumption vs miss distance.

Figure 6.14: Maximum G-load and propellant consumption for each of the 500 simulations performed for the dispersion analysis.

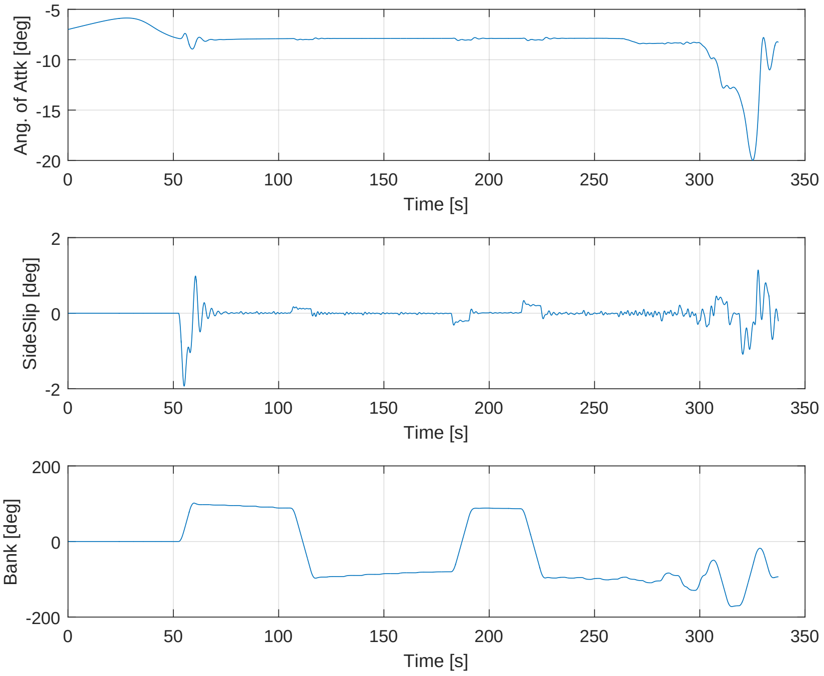

Figure 6.15: Aerodynamic angle as a function of time for the return from GTO.

Just as with the return flight from LEO the entry starts with a short coast phase, where the bank angle is held at $0°$ until aerodynamic acceleration reaches a value of 0.2 g and the guidance algorithm becomes active. The higher initial velocity and the steeper flight-path angle results in a higher dynamic pressure experienced by the vehicle earlier in the flight compared to a return from LEO. This leads to the 0.2 g condition to be met only 50 s after entry interface. The angle of attack and side-slip angle show a similar behavior to the reentry from LEO. The most significant difference is a higher dampening of any oscillation due to a more rapid rise in dynamic pressure.

The heat flux, total heat load, and G-load as a function of time are given in Figure 6.16(b) in the top, center, and bottom plot, respectively. The peak in this case occurs already at around 120 s. A slightly smaller bump in G-loads is visible between 250 s and 330 s. This is caused by the rapidly increasing air density as the vehicle begins to fall towards the Earth again, which in turn leads to a rapid increase in dynamic pressure.

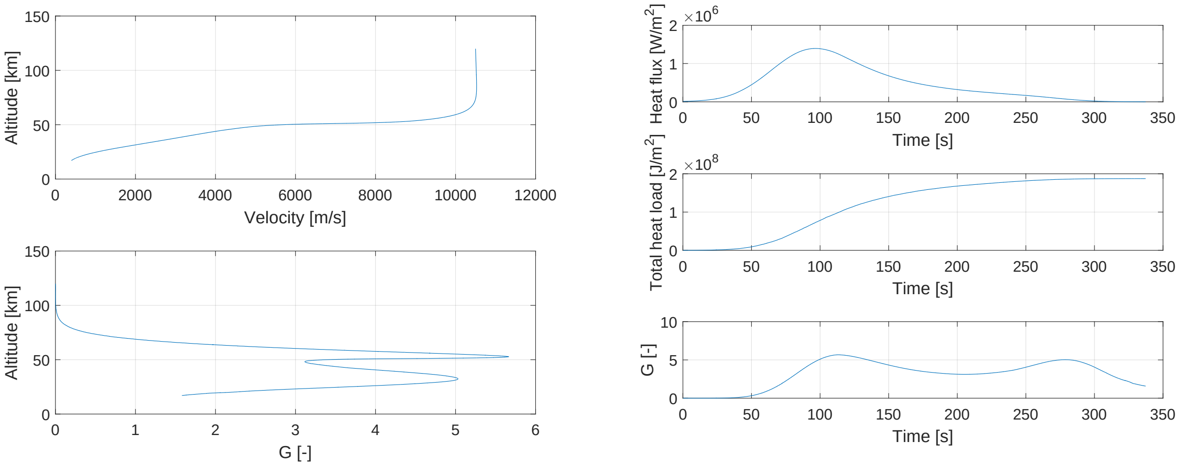

(a) Altitude as function of velocity(top) and G-load(bottom).

(b) Heat flux, total heat load, and G-load as function of time.

Figure 6.16: Flight profile and flight loads during reentry from GTO.

The flight-path angle at entry interface for high orbit reentries is chosen higher than for reentries from lower orbits. The vehicle enters the atmosphere at significantly higher velocities and needs the initial period of atmospheric deceleration to lower the apogee of the orbit. If the vehicle's flight-path angle is too low the upper stage risks exiting the atmosphere again and climbing to the new apogee before reentering one orbit later. However, using a steeper flight-path angle means the vehicle descents deeper into the atmosphere, where the higher density combined with the high entry velocity cause higher loads.

Hence, as one would expect the value for the heat flux is significantly higher, proportional to the airspeed to the third power compared to a reentry from LEO. As mentioned earlier the heat flux is only proportional to the air density to the power of one half, which is also the reason for the lack of a second bump like in the G-load plot.

Plots of the altitude as a function of airspeed and G-load are given in Figure 6.16(a). Here we see that the vehicle flies almost horizontally for a portion of the trajectory, where it experiences the highest deceleration until the apogee drops below the perigee and the descent continues.

To study the effect of the flight-path angle on the reentry loads the reentry of the upper stage from GTO is simulated again with flight-path angles of $-6°$, $-6.5°$, and $-7°$. The results are plotted in Figure 6.17.

As expected a steeper flight-path angle results in an increase in the peak heat flux and G-load on the vehicle due to a more rapid descent into deeper layers of the atmosphere. Interestingly the total heat load is smaller due to a shorter reentry duration. The reduction in total heat load could translate into a reduction in heat shield mass. However, this gains must be compared to a higher structural mass due to the higher G-loads and the need for a more robust overall heat shield design with higher insulation due to the more extreme heat flux.

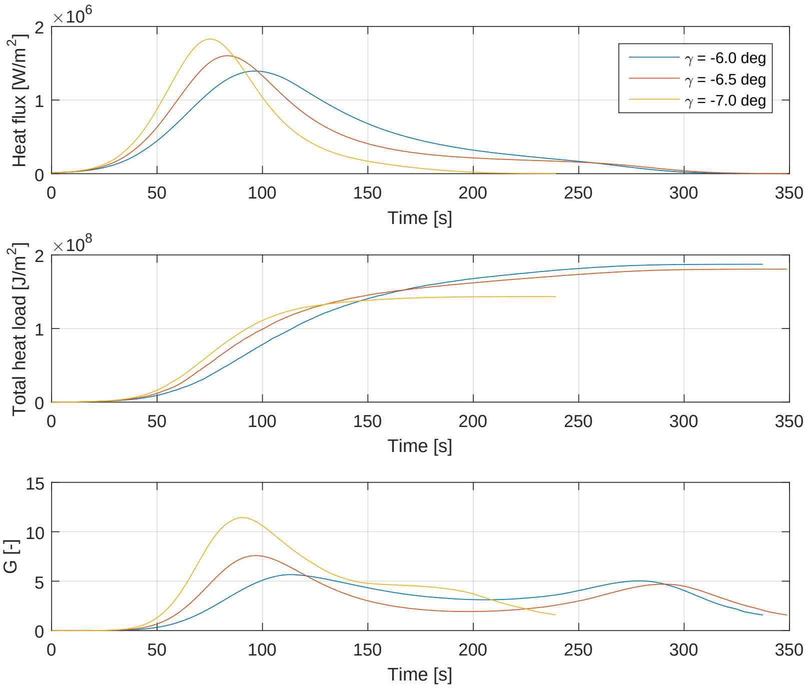

Figure 6.17: Loading during reentry from GTO at flight angles of $-6°$, $-6.5°$, and $-7°$.

In Figure 6.18 the controller response is plotted as function of time for the reentry from GTO. The guidance and control system reacts as intended and delivers the vehicle to the target with the same accuracy as for reentries from LEO. The most notable differences compared to a reentry from LEO is the slightly higher propellant consumption due to the higher number of bank reversals. But again most of the propellant is consumed towards the end of the flight when the vehicle attempts to stabilize itself amid rapidly changing aerodynamic coefficients and resulting commanded bank angle.

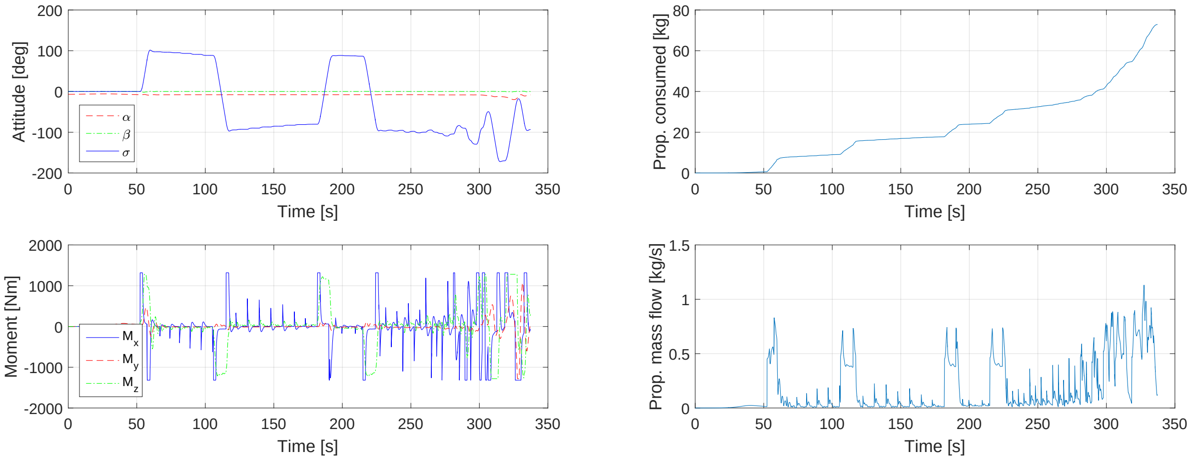

(a) Attitude and control moment as function of time

(b) Propellant consumption and propellant mass flow as function of time

Figure 6.18: Control response plots for an upper stage returning from GTO.

7

Conclusion & Recommendations

With the results presented in Chapter 6 it is now possible to give a tentative answer to the research question, which is stated as:

> *”Is it possible to stabilize and control a conventionally-shaped reusable upper stage during reentry and descent?”*

Given the complexity involved with predicting the flow of air around a vehicle a definitive answer can only be given by flight testing a prototype vehicle. However, this research uses available theoretical models to give a preliminary assessment, which can be used to justify more detailed analysis into the different aspects of a reusable cylindrical upper stage.

This final chapter first summarizes the results obtained in the previous chapter and based on that presents a conclusion, which answers the research question. Since this work is only a preliminary analysis of this concept, the conclusions are followed by recommendations for future steps towards further analyzing, improving, and ultimately realizing such a vehicle.

7.1. Conclusion

As stated in Chapter 1 to assess the stability and controllability of the reference upper stage vehicle an analysis of several aspects of the vehicle and its descent trajectory into the atmosphere is necessary. The first major aspect is its aerodynamic stability, which is a prerequisite for a successful reentry at the desired nose-first attitude. Given a stable entry attitude it is also necessary for the descent to be save and economical in terms of flight loads and propellant consumption for the concept to be viable. Finally, the ability of such a vehicle to complete its mission and reach a position above the landing site is demonstrated under realistic conditions using reentry simulations. All of these points are discussed and evaluated in this section.

7.1.1. Aerodynamic Stability

The aerodynamic stability of the vehicle depends on the sign of the moments acting on the vehicle and either push it towards an equilibrium attitude or away from it when disturbed. The positive sign of the moment coefficients at positive angles of attack for the baseline reference vehicle indicate a static instability. Moving the center of mass further to the back only worsens the static instability. This is despite also a length increase, which has on its own a stabilizing effect.

A positive relationship between shorter upper stages and an increased static stability is found, which is usually at odds with the common rocket design practice of minimizing rocket body diameter to reduce drag during ascent (Sutton and Biblarz, 2010). However, the expected economical and practical benefits of reusability could potentially more than justify such a performance hit and allow for one launcher to put multiple times its payload capacity into orbit.

Designing the reusable upper stage with a certain length-to-diameter ratio is an option for new launch vehicle developments with reusability in mind. However, if that ratio is constrained due to heritage or other limitations two methods are investigated to improve the static stability of the reference vehicle. First a stretching of the upper stage body is analyzed without changing the center of mass to observe its effect on the stability. This can be achieved in practice by, for example, integrating part of the interstage to the back of the upper stage effectively creating an aft skirt.

The baseline and aft-skirt configuration are both analyzed in terms of static aerodynamic stability using Missile DATCOM. The addition of an aft skirt improved the stability of the baseline vehicle sufficiently to make it stable for most of the center-of-mass locations found in the analysis in Section 3.4. It could prove sufficient to stabilize a reusable upper stage especially with a more favorable length-to-diameter ratio.

Simulations of the attitude dynamics of a vehicle with flaps show a harmonic motion around the equilibrium attitude as one would expect in a constant airflow, since no dampening coefficients are used to model any aerodynamic resistance to the rotation. The effectiveness of the flaps becomes clear as they stabilize the vehicle with much less surface area compared to the extended aft skirt configuration. Given the heritage behind flap stabilization of vehicle, such as the Space Shuttle or the Falcon 9 first stage, a flapped configuration of the upper stage is regarded as a promising solution for the stability problem of potentially unstable cylindrical upper stages.

Full 6-degree-of-freedom reentry simulations mirror the results found so far on the stability of this vehicle configuration throughout the reentry and decent amid the rapidly changing forces and moments due to variations in the atmosphere and the vehicle's state. The aerodynamic angles remains close to the passive trim attitude up to the terminal point despite the erratic behavior of the aerodynamic coefficients at low supersonic velocities.

From these results one can conclude that aerodynamic stability for a reusable upper stage as proposed by SpaceX is possible at least with some modifications to the vehicle. The stability of a typical upper stage that consists of a cylindrical body with the thrust structure and engine in the back in general depends on the position of the center of mass with respect to the heat shield surface and the diameter of the upper stage. In terms of aerodynamic stability a short upper stage is favored over more elongated one, which is at odds with typical rocket design philosophies of reducing rocket diameter to minimize aerodynamic drag during ascent. However, it may be worth it economically, since the vehicle could then potentially deliver multiple flights worth of payload to space, which would make up for the hit in payload capacity due to being reusable and causing more drag during ascent.

7.1.2. Reentry Loads and Propellant Consumption

For a reentry vehicle to not only be feasible, but also economical, the heat and mechanical loads experienced during descent must be such that no excessive structural strengthening or thermal protection is necessary.

The heat loads experienced by the upper stage in the reentry simulation from LEO reflect a typical reentry environment as experienced by low lift-to-drag reentry vehicle (Jenkins, 2012; Mooij, 2015). With a maximum G-load of less than 6 g the vehicle does not exceed the level of stress experienced during ascent with the payload mounted on top of it. Hence in terms of longitudinal mechanical loading an upper stage build for ascent at 6 g such as the Falcon 9 should have the required structural integrity for reentry (SpaceX, 2015). However, while most reentries in the dispersion analysis remained below that value careful trajectory design is required to avoid the cases, where the vehicle experienced excessive G-loads. Otherwise some structural reinforcement along the longitudinal may be required. The maximum G-loads observed when returning from GTO are somewhat similar to the reentry form LEO given also proper trajectory design and control before entry interface.

However, the capability of an upper stage with its thin walled tank walls to withstand the lateral forces at a useful angle of attack is a big uncertainty. The maximum lateral acceleration expected during a Falcon 9 launch is 2 g (SpaceX, 2015). Using a relatively small angle of attack may limit the stresses on the side walls during reentry to similar levels. However, reducing the angle of attack and therefore lift comes at the cost of reduced crossrange control authority.

These measures can address the accelerations as experienced by the center of mass, but due to a current lack of detailed flow analysis around the vehicle localized pressure peeks can not be ruled out. Hence localized structural strengthening of the sidewalls in certain areas may nevertheless still be required.

While the mechanical stress environment experienced by the upper stage during reentry may be quite similar to those experienced during launch the heat load the vehicle is subjected to during descent far exceeds those during launch. This makes a dedicated thermal protection system for the reentry necessary. As expected, a significant increase in the heat flux is observed for returns from GTO compared to reentries from LEO. Important for the design of the heat shield is the total heat load experienced as it determines the total amount of ablation material needed. The heat flux only influences the rate of ablation assuming an ablative heat shield is used. The total heat load almost doubles as the upper stage returns from GTO compared to LEO, but in both cases remains within a practical range compared to past reentries (Jenkins, 2012). Adjusting the flight-path angle offers some room for further reducing the heat shield mass, but at the cost of higher heat rate and G-loads.

The heat shield design including the interface with the payload and fairing represents one of the major design challenges of such a vehicle compared to a conventional upper stage. A working example of something approximating a reusable upper stage is the Space Shuttle, which had both an interface with the external tank and landing gear bays on the bottom, where the main heat shield is located. Similar mechanisms can be used to interface the vehicle with the payload and fairing despite the heat shield.

The final aspect studied in this project is the propellant consumption for the attitude control during reentry. The propellant adds to the mass of the upper stage, where every kilogram of additional vehicle mass must be subtracted from the payload mass. The required propellant mass for a guided reentry from LEO is shown to be no more than 57 kg using thrusters with an I_{sp} of 300 s. This represents a small fraction of the total vehicle and is less than the mass of most ob-board subsystems. Even for returns from GTO the amount of propellant is still relatively small. All upper stages today are already equipped with an attitude and orbit control system for precise orbital insertion of the satellite at the desired attitude. Hence this makes the additional propellant indeed all that is required to control the vehicle's attitude during reentry and descent as well.

Results from the dispersion analysis hint at the possibility to optimize fuel consumption by minimizing the number of bank reversals through either biasing the heading of the vehicle either way or through the use of a guidance algorithm aimed at minimizing bank reversals. Also turning off the guidance or even the entire attitude control system at low supersonic velocities may yield even higher propellant savings at the cost of making the vehicle passive for the last portion of the flight.

7.1.3. Crossrange Capability

The capability to change heading and steer a vehicle to a predefined target site accurately is crucial for a successful pinpoint landing and rapid reusability. The crossrange capability of the reference reusable upper stage is the limiting factor due to the small lift-to-drag ratio. This issue has been identified in several other projects aimed at developing a vehicle similar in shape, such as the Delta Clipper or FESTIP Concept 3. Both vehicle suffer from a similar crossrange limitation due to their shape. Capsules such as the Apollo CM or Soyuz descent module use a relatively large angle of attack to increase lift, which is difficult and unfavorable for reusable rocket stage.

As the angle of attack of the upper stage increases so does the fraction of the lift produced by the cylindrical body instead of the heat shield surface at the head of the vehicle. Both fractions of the lift force oppose each other, which makes the lift go into the negative direction at first, reaching a minimum at $15°$, and then rises again to the positive.

At an angle of attack similar to the Apollo capsule of $-23°$ the lift would be the same as at an angle of attack of $-7°$. To achieve the same lift force magnitude as observed at an angle of attack of $-15°$ on the positive side would require at least an angle of attack of $38°$, which is not desired due to excessive lateral forces and heating on the side walls of the tank. To limit the exposure of the side walls to these loads an angle of attack of less then $10°$ is more favorable. Through the mass estimation performed in Section 3.4 an angle of attack of $-6.5°$ is found to be feasible. These constraints leave little room to improve the lift without an extensive redesign of the upper stage more akin to a space plane.

The lacking crossrange capability can be compensated for with accurate tracking and maneuvering in orbit to ensure the vehicle is heading straight to the target. Given the orbit determination and maneuvering accuracy possible today the vehicle's crossrange capability should be sufficient to compensate for any remaining deviations (Jekeli, 1999).

In this study an extensive analysis of the trajectory and aerodynamics of a potentially reusable upper stage returning from both LEO and GTO is done within the possibilities of the available data. The overall conclusion is that such a vehicle has the potential to be aerodynamically stable and controllable, or can be made stable using flaps for stabilization. Furthermore, the impact of reusability on the economics of the launch vehicle are touched upon within the scope of the available results. While the available results are by far not all-encompassing for a final verdict on its profit margin, they do not show any glaring physical or practical issues that would render this concept unfeasible and uneconomical.

7.2. Recommendations

After the conclusion of this report is given attention is now drawn to critical areas, where available information is lacking or a gap in knowledge is present, which needs to be addressed to further improve the certainty in the feasibility of reusable upper stages based on expandable upper stages flying today.

7.2.1. Aerodynamic Model

One of the key uncertainty in this concept is the aerodynamics of an upper stage as proposed by SpaceX and presented in this report. The stability of the vehicle is dependent on the aerodynamic moment coefficients, which is a result of the air pushing on the vehicle. Determining the airflow around even simple shapes is often very complex and requires sophisticated fluid simulation techniques or even practical experiments to achieve it accurately.

Hence the first and most important next step in the analysis and development of a reusable upper stage as presented in this report is to perform numerical fluid dynamics analysis or wind tunnel experiments. A better aerodynamic model of the vehicle improves confidence in the design and helps to determine appropriate measures to stabilize the vehicle. Also the impact of the bell nozzle on the aerodynamic stability of a reusable upper stage can be studied, which was not possible in this project due to limitations in Missile DATCOM.

7.2.2. Localized Heating and TPS Design

A preliminary analysis of the thermal environment of the upper stage at the stagnation point is presented in this report. Using an appropriate aerothermodynamic modelling tool the thermal environment around the entire upper stage during reentry must be studied, especially the side walls, which may experience significant heating without the protection of the strong shock wave generated at the flat front. Knowledge of the thermal environment is an important input for material selection and sizing of the heat shield.

Determining the dimensions of the heat shield is not only important from a design standpoint, but crucial also to the question of practicality of such a concept. The primary mission of an upper stage is to deliver a payload into orbit. Any additional structural mass that needs to be carried to orbit effectively reduces the payload capability of the launcher by the same amount. The impact of the additional mass on the payload capacity of the launcher needs to be assessed to ensure that the launch vehicle remains not only a practical, but even a more economical option compared to expandable rockets despite the modifications.

Hence a careful analysis of the thermal environment around the upper stage and especially any interaction between the reentry plasma and the vehicle must be performed. The information gained from such an analysis can be used to properly design the thermal protection system and determine its true mass. However, one must keep in mind that terminal deceleration devices such as landing gears, parachutes, and/or landing thrusters must be introduced into the analysis as well in terms of mass and feasibility to gain a complete picture of the vehicle. Since the focus of this work is the reentry, this is left for the interested reader to work on in the future.

7.2.3. Lateral Stresses and Structural Reinforcement

Given the primary mission of every launch vehicle it can be assumed that any longitudinal stresses experienced during ascent is on the same order or higher than the stress experienced on return, primarily due to the moderately high G-loads coupled with the heavy payload mass sitting on top of the vehicle during ascent.

Lateral stresses on the other hand are more difficult to compare. Most launch vehicle use gravity turns until the launch vehicle has left Earth's atmosphere before activating more sophisticated guidance methods for orbit insertion. In a gravity turn the launch vehicle points its longitudinal axis in the direction of the velocity vector in the aerodynamic frame. This results in a purely ballistic flight with zero angle of attack and side-slip angle. Such a configuration minimizes lateral forces, where the thin walled tanks of rockets are the weakest.

By choosing a low angle of attack an effort is made to keep lateral stresses low while still generating a lift force adequate for control. This comes at the cost of reduced trajectory control authority, especially in the ability to control the heading. Despite the effort the lateral forces generated during reentry as a result may be higher than those experienced during ascent using the gravity turn. It is therefore also critical to perform a more detailed structural analysis and design of a reusable upper stage to first determine any additional lateral stresses experienced by the vehicle during reentry and then reinforce the structure where necessary. This task also lies in the critical path towards realizing a reusable upper stage for the same reason as for the heat shield. An excessive increase in mass of the upper stage due to the additional structural reinforcement could compromise the practicality or even the feasibility of such a vehicle.

7.2.4. Active Flaps

The primary vehicle configuration described in this report uses flaps to stabilize the upper stage. A shift in the center of mass of the vehicle results in a fixed passive trim attitude given the current flight regime. By changing the flap deflection angle during flight the trim attitude can be controlled. This is not necessary for a successful reentry of a reusable upper stage as one can see in the results given in Chapter 6 as well as in the success of many ballistic reentry vehicle such as the Apollo CM. However, using active flaps enables the upper stage to adjust the angle of attack as needed, either to compensate for any difference between the expected and actual location of the center of mass or to improve control over the trajectory.

A fixed trim attitude yields a maximum downrange distance when the bank angle is $0°$ and a minimum downrange distance when the bank angle is $180°$. With an active flap the maximum downrange distance can be changed by pointing the vehicle at an angle of attack, which results in a higher lift-to-drag ratio. To minimize the downrange distance an attitude with maximum lift combined with a $180°$ bank angle may be used to bend the trajectory down into the denser parts of the atmosphere. To improve the crossrange capability maximum lift can again be used in combination with a $90°$ bank angle to quickly remove excessive heading errors before transitioning back to maximum lift-to-drag ratio. This ignores limitation of the vehicle such as heating and G-loading for the sake of illustrating the concept, which may be exceeded when executing such a maneuver. This also needs to be taken into account.

Bibliography

Abby, G., Bauman, W., Cook, D., Ehemberger, J., and et. al., D. F. (2010). Guide to reference and standard atmosphere models. American Institute of Aeronautics and Astronautics/American National Standards Institute.

Abevnayaka, D. and Agon, A. (2013). Comparison of computational and semi-empirical aerodynamics tools for making fit-for-purpose modelling decisions. In 20^{th} *International Congress on Modelling and Simulation*.

Ambrosius, B. A. C. (2009). Rocket motion. AE4870A TU Delft Lecture Notes, Astrodynamics and Space Missions.

Anderson, J. D. (1989). *Hypersonic and High Temperature Gas Dynamics*. McGraw-Hill Book Company.

Anderson, J. D. (2016). *Introduction to Flight*. McGraw-Hill Education.

Angelo, J. A. (2006). *Frontiers in Space: Rockets*. Facts on File Inc.

Barrio, A. M., Sudars, M., Aulisio, R., Massobrio, F., and Passarelli, G. (2011). Expert - the esa experimental re-entry test-bed.trajectory and mission design. *AIAA Guidance, Navigation, and Control Conference*.

Bechhoefer, J. (2005). Feedback for physicists: A tutorial essay on control. *REVIEWS OF MODERN PHYSICS*, 77.

Bezos, J. P., Lai, G., and Findlay, S. R. (2014). Sea landing of space launch vehicles and associated systems and methods.

Blau, P. (2016). Falcon 9 ft (falcon 9 v1.2) launch vehicle overview. [Last accessed: 1.6.2016].

Brooks, C. G., Grimwood, J. M., and Swenson, L. S. (1979). Chariots for Apollo: A History of Manned Lunar Spacecraft. NASA History Office.

Bullard, J. W. (1965). History of the redstone missile system. Technical report, Army Missile Command.

Button, E. C., Lilley, C. R., Machenzie, N. S., and Sader, J. E. (2009). Blunted-cone heat shield of atmospheric entry vehicles. *AIAA Journal*, 47(7).

Casey, P. I. (2013). *Mission Decade of Achievement*. JS Blume.

Cheatwood, P. N. D. . R. A. M. . F. M. (1997). Entry dispersion analysis for the stardust comet sample return capsule. In *GNC, AFM, and MST Conference and Exibit (AIAA)*.

Chertok, B. (2005). *Rockets and People*. NASA History Office.

Cooper, P. A. and Holloway, P. F. (1981). The Shuttle Tile Story. *Astronautics and Aeronautics*.

de Selding, P. B. (2016). Spacex to launch ses-10 on previously flown falcon 9 this year. SpaceNews.com.

Diaz, R. A., Herrera, W. J., and Martinez, R. (2005). Some powerful methods to calculate moments of inertia. Technical report, Universidad Nacional de Colombia, Departamento de Física. Bogotá, Colombia.

Dinardi, A., Capozzoli, P., and Shotwell, G. (2008). Low-cost launch opportunities provided by the falcon family of launch vehicles. In *The Fourth Asian Space Conference*.

Dirkx, D. (2011). *Conceptual Shape Optimization of Entry Vehicles*. Delft University of Technology.

Dujarric, C. (1999). Possible future european launchers: A process of convergence. Technical report, European Space Agency.

Frieman, E. A., Barron, E. J., Costanza, R., Dozier, J., Eagleson, P., Grew, P. C., and Hallgren, R. E. (1994). *Solar Influences on Global Change*. The National Academies Press.

Gatland, K. W. (1976). *Manned Spacecraft*. Macmillan.

Harpold, J. C. and Graves, C. A. (1979). Shuttle entry guidance. Technical report, National Aeronautics and Space Administration, Mission Planning and Analysis Division.

Harvey, B. and Zakutnyaya, O. (2011). *Russian Space Probes: Scientific Discoveries and Future Missions*. Springer.

Hertzfeld, H. R., Williamson, R. A., and Peter, N. (2005). Launch vehicles: An economic perspective. Technical report, Space Policy Institute, The George Washington Univeristy.

Hibbeler, R. C. (2009). *Engineering Mechanics Dynamics*. Prentice Hall.

Hibbeler, R. C. (2016). *Engineering Mechanics: Statics*. Pearson Education Limited.

Jekeli, C. (1999). The determination of gravitational potential differences from satellite-to-satellite tracking. *Celestial Mechanics and Dynamical Astronomy*, 75(2).

Jenkins, D. R., Landis, T., and Miller, J. (2003). *American X-Vehicle*. NASA History Office.

Jenkins, R. D. L. . D. R. (2012). *Coming Home: Reentry and Recovery from Space*. U.S. National Aeronautics and Space Administration.

Knocke, P. C., Wawrzyniak, G. G., Kennedy, B. M., Desai, P. N., Parker, T. J., Golombek, M. P., Duxbury, T. C., and Kass, D. M. (2004). Mars exploration rovers landing dispersion analysis. AIAA/AAS Astrodynamics Specialist Conference and Exhibit.

Koelle, D. E., Grallert, H., Peters, K., and Sacher, P. (2007). *Deutsche Raketenflugzeuge und Raumflugzeug-Projekte*. Bernard & Graefe.

Korkegi, R. H., Clayton, J., and Farrar, A. L. (1983). Assessment of constrains on space shuttle launch rates. National Research Council.

Kreysig, E. (1972). *Advanced Engineering Mathematics*. John Wiley and Sons, Inc., tenth edition edition.

Kuipers, J. B. (2002). *Quaternions and Rotation Sequences: A Primer with Applications to Orbits, Aerospace and Virtual Reality*. Princeton University Press.

Kyle, E. (2015). Space launch report: Spacex falcon 9 v1.1 data sheet. [Last accessed: 1.6.2016].

Lebreton, J.-P., Witasse, O., Sollazzo, C., Blancquaert, T., Couzin, P., Schipper, A.-M., Jones, J. B., Matson, D. L., Gurvits, L. I., Atkinson, D. H., Kazeminejad, B., and P□rez-Ay□car, M. (2005). An overview of the descent and landing of the huygens probe on titan. *Nature*, 438.

Leverington, D. (2001). *New Cosmic Horizons: Space Astronomy from the V2 to the Hubble Space Telescope*. Cambridge University Press.

Lu, P. (2008). Predictor-corrector entry guidance for low-lifting vehicles. *Journal of Guidance, Control, and Dynamics*, 31(4).

Massobrio, F., Viotto, R., Serpico, M., and Muylaert, J. (2007). Expert: An atmospheric re-entry test-bed. *Acta Astronautica*, 60(12).

Maynard, O. E., Low, G. M., and Kraft, C. C. (1969). CSM/LM Spacecraft Operational Data Book: Mass Properties. Technical report, National Aeronautics and Space Administration, Apollo Spacecraft Program Office Systems Engineering Division.

McNary, R. L. (1965). Aerodynamic data manual for project apollo. Technical report, North American Aviation, Inc.

Meyerson, R., Emde, W., Wallace, D., and Barber, D. (1999). Development of a reusable thermal protection system for the k-1 orbit vehicle. In *50th International Astronautical Congree*.

Miller, F. E., Cassidy, J. L., Leveye, J. C., and Johnson, R. I. (1964). The mercury-redstone project. Technical report, Marshall Spaceflight Center.

Montenbruck, O. and Gill, E. (2011). *Satellite Orbits*. Springer.

Mooij, E. (1994). The motion of vehicle in a planetary atmosphere. Technical report, University of Technology Delft.

Mooij, E. (1998). *Aerospace-Plane Flight Dynamics: Analysis of Guidance and Control Concepts*. PhD thesis, Delft University of Technology.

Mooij, E. (2015). Re-entry systems. AE4870B TU Delft Draft Lecture Notes, Astrodynamics and Space Missions.

Morgan, M. G., Caluori, V., Davis, J., Dergarabedian, P., McKinney, B., Rubin, C. P., Schnitt, A., Drew, R., Fester, D. A., and Shore, T. (1989). Big dumb boosters: A low-cost space transportation option? Technical report, Office of Technology Assessment.

Mulder, J. A., van Staveren, W. H. J., van der Vaart, J. C., de Weerdt, E., in't Veld, A. C., and Mooij, E. (2011). Flight dynamics. AE3202 TU Delft Lecture Notes, Control and Simulation.

Nagel, J. R. (2012). Introduction to numerical integration. ECE 5340/6340 University of Utah Lecture Notes, Department of Electrical and Computer Engineering.

NOAA, N. (1976). Us standard atmosphere 1976. Technical report, National Aeronautics and Space Administration.

Novak, H. L., Hall, P. B., and Martin, D. (2002). Environmentally compatible vapor-phase corrosion inhibitor for space shuttle hardware. In *5th AMPET Conference*.

O'Leary, B. (1973). The space shutte - nasa's white elephant in the sky. *Bulletin of the Atomic Scientist*.

Paschen, H. (1993). Technikfolgenabschätzung zum Raumtransportsystem Sänger. Büro für Technikfolgen-Abschätzung beim Deutschen Bundestag.

Perez, E. (2011). *Ariane 5 User's Manual*. Arianespace.

Pichon, T., Coperet, H., Foucault, A., and Lacombe, A. (2005). Vinci upper stage engine nozzle extension development status. In *41st AIAA/ASME/SAE/ASEE Joint Propulsion Conference & Exhibit*.

Pielke, R. A. (2008). The rise and fall of the space shuttle. *American Scientist*, 96.

Polyanin, A. D. and Manzhirov, A. V. (2007). *Handbook of Mathematics for Engineers and Scientists*. Chapman & Hall/CRC.

Press, W. H., Teukolsky, S. A., Vetterling, W. T., and Flannery, B. P. (2007). *Numerical Recipes: The Art of Scientific Computing*. Cambridge University Press, 3rd edition.

Putz, K. E. and Bartlett, E. P. (1973). Heat-transfer and ablation-rate correlations for re-entry heat-shield and nosetip applications. *Journal of Spacecraft and Rockets*, 10(1).

Reed, R. D. (1997). *Winged Flight: The lifting body story*. NSAS History Office.

Rosema, C., Doyle, J., Auman, L., Underwood, M., and Blake, W. B. (2011). *Missile DATCOM User's Manual*. U.S. Army Aviation and Missile Research, Control Design and Analysis Branch.

Rudman, T. J. and Austad, K. L. (2002). The centaur upper stage vehicle. In *4th International Conference on Launcher Technology*.

Saraf, A., Leavitt, J. A., Chen, D. T., and Mease, K. D. (2004). Design and evaluation of an acceleration guidance algorithm for entry. *AIAA Journal of Spacecraft and Rockets*, 41(6).

Schnitt, A. (1998). *Minimum Cost Design for Space Operations*. Foyle Publishing.

Schutz, B., Tapley, B., and Born, G. H. (2004). *Statistical Orbit Determination*. Academic Press.

Sidi, M. J. (1997). *Spacecraft Dynamics and Control*. Cambridge University Press.

SpaceX (2009). *Falcon 9 Launch Vehicle Payload User Guide*. Space Exploration Technologies Corp., rev. 1 edition.

SpaceX (2015). *Falcon 9 Launch Vehicle PAYLOAD User Guide*. Space Exploration Technologies Corp., rev 2 edition.

Stechman, C. and Harper, S. (2010). Performance improvements in small earth storable rocket engines - an era of approaching the theoretical. In *46th AIAA/ASME/SAE/ASEE Joint Propulsion Conference & Exhibit*.

Steketee, F. D. (1967). Nasa contractor report: Dynamic stability of space vehicle. Technical report, General Dynamics Corporation.

Stewart, J. (2008). *Calculus: Early Transcendentals*. Cengage Learning Emea.

Sutton, G. P. and Biblarz, O. (2010). *Rocket Propulsion Elements*. Wiley, 8th edition.

Tapley, B. D., Schutz, B. E., and Born, G. H. (2004). *Statistical Orbit Determination*. Elsevier Academic Press.

Teunissen, P., Simons, D., Tiberius, C., and Verhagen, S. (2010). Probability and statistics for aerospace engineering. WI2207LR TU Delft Lecture Notes, Faculty of Aerospace Engineering.

VanHooser, K. P. and Bradley, D. P. (2011). Space shuttle main engine - the relentless pursuit of improvement. In *AIAA SPACE 2011 Conference*.

Venkatapathy, B. L. . E. (2004). Thermal protection system technology and facility needs for demanding future planetary missions. In *Planetary Probe Atmospheric Entry and Descent Trajectory Analysis and Science*, volume 544.

Vinh, N. X., Busemann, A., and Culp, R. D. (1980). *Hypersonic and PlanePlan Entry Flight Mechanics*. The University of Michigan Press.

Wachtel, C. (1982). Design studies of the Vostok-J and Soyuz spacecraft. *British Interplanetary Society Journal (Soviet Astronautics)*, 35.

Wakker, K. F. (2010). Astrodynamics 1+2. AE4874 TU Delft Lecture Notes, Astrodynamics and Space Missions.

Website, S. (2016). Falcon 9. [Last accessed: 1.6.2016].

Weiland, C. (2014). *Aerodynamic Data of Space Vehicles*. Springer.

Wertz, J. R., Meissinger, H. F., Newman, L. K., and N.Smit, G. (2009). *Orbit and Constellation Design and Management*. Microcosm Press and Springer.

Wie, B. (2008). *Space Vehicle Dynamics and Control*. American Institute of Aeronautics and Astronautics.

Wilkins, M. (2010). *Atlas V Launch Service User's Guide*. United Launch Alliance & Lockheed Martin Commercial Launch Services.

Yang, Y. (2012). Analytic lqr design for spacecraft control system based on quaternion model. *Journal of Aerospace Engineering*, 25(3):448–453.

A

Apollo CM DATCOM for006.dat File

```
1         ***** THE USAF AUTOMATED MISSILE DATCOM * REV 03/11 *****
               AERODYNAMIC METHODS FOR MISSILE CONFIGURATIONS

     CONERR - INPUT ERROR CHECKING

     ERROR CODES - N* DENOTES THE NUMBER OF OCCURENCES OF EACH ERROR
     A - UNKNOWN VARIABLE NAME
     B - MISSING EQUAL SIGN FOLLOWING VARIABLE NAME
     C - NON-ARRAY VARIABLE HAS AN ARRAY ELEMENT DESIGNATION - (N)
     D - NON-ARRAY VARIABLE HAS MULTIPLE VALUES ASSIGNED
     E - ASSIGNED VALUES EXCEED ARRAY DIMENSION
     F - SYNTAX ERROR

     ************************* INPUT DATA CARDS *************************

    1 CASEID ApollotestComp
    2 DIM M
    3 DERIV DEG
    4  $REFQ
    5  XCG=1.1,
    6  ZCG=0.137,
    7  SREF=12.0,
    8  LREF=3.911,
    9  LATREF=3.911,
   10  RHR=400.0,
   11  $END
   12  $FLTCON
   13  NALPHA=50.,
   14  ALPHA=-0.,-1.,-2.,-3.,-4.,-5.,-6.,-7.,-8.,-9.,
   15  ALPHA(11)=-10.,-11.,-12.,-13.,-14.,-15.,-16.,-17.,-18.,-19.,
   16  ALPHA(21)=-20.,-21.,-22.,-23.,-24.,-25.,-26.,-27.,-28.,-29.,
   17  ALPHA(31)=-30.,-31.,-32.,-33.,-34.,-35.,-36.,-37.,-38.,-39.,
   18  ALPHA(41)=-40.,-41.,-42.,-43.,-44.,-45.,-46.,-47.,-48.,-49.,
   19  BETA=0.,
   20  NMACH=1.0,
   21  MACH=10.0,
   22  ALT=35000.0,
   23  $END
   24  $AXIBOD
   25  NX=11.0,
```

```
  26  X=0.0,0.0467818,0.0935637,0.187127,0.280691,0.374255,0.419348,
  27  X(8)=0.464441,0.509534,0.554628,2.627,
  28  R=0.0,0.661059,0.932535,1.31215,1.59886,1.83669,1.90183,
  29  R(8)=1.93402,1.95074,1.956,0.314172,
  30  DEXIT=0.0,
  31  DISCON=11.0,
  32  $END
  33 SOSE
  34 NO LAT
  35 PLOT
  36 PRINT GEOM BODY
  37 SAVE
    NEXT CASE                  ** MISSING NEXT CASE CARD ADDED **
1        ***** THE USAF AUTOMATED MISSILE DATCOM * REV 03/11 *****    CASE   1
              AERODYNAMIC METHODS FOR MISSILE CONFIGURATIONS         PAGE   1
    CASE INPUTS
    FOLLOWING ARE THE CARDS INPUT FOR THIS CASE

 CASEID ApollotestComp
 DIM M
 DERIV DEG
  $REFQ
  XCG=1.1,
  ZCG=0.137,
  SREF=12.0,
  LREF=3.911,
  LATREF=3.911,
  RHR=400.0,
  $END
  $FLTCON
  NALPHA=50.,
  ALPHA=-0.,-1.,-2.,-3.,-4.,-5.,-6.,-7.,-8.,-9.,
  ALPHA(11)=-10.,-11.,-12.,-13.,-14.,-15.,-16.,-17.,-18.,-19.,
  ALPHA(21)=-20.,-21.,-22.,-23.,-24.,-25.,-26.,-27.,-28.,-29.,
  ALPHA(31)=-30.,-31.,-32.,-33.,-34.,-35.,-36.,-37.,-38.,-39.,
  ALPHA(41)=-40.,-41.,-42.,-43.,-44.,-45.,-46.,-47.,-48.,-49.,
  BETA=0.,
  NMACH=1.0,
  MACH=10.0,
  ALT=35000.0,
  $END
  $AXIBOD
  NX=11.0,
  X=0.0,0.0467818,0.0935637,0.187127,0.280691,0.374255,0.419348,
  X(8)=0.464441,0.509534,0.554628,2.627,
  R=0.0,0.661059,0.932535,1.31215,1.59886,1.83669,1.90183,
  R(8)=1.93402,1.95074,1.956,0.314172,
  DEXIT=0.0,
  DISCON=11.0,
  $END
 SOSE
 NO LAT
 PLOT
 PRINT GEOM BODY
 SAVE
 NEXT CASE
```

```
    THE BOUNDARY LAYER IS ASSUMED TO BE TURBULENT
    THE INPUT UNITS ARE IN METERS, THE SCALE FACTOR IS   1.0000
1       ***** THE USAF AUTOMATED MISSILE DATCOM * REV 03/11 *****  CASE   1
             AERODYNAMIC METHODS FOR MISSILE CONFIGURATIONS        PAGE   2
                               ApollotestComp
                        AXISYMMETRIC BODY DEFINITION

    LENGTH                2.6270    FINENESS RATIO        0.6715
    PLANFORM AREA         6.3068    AREA CENTROID         1.0841
    WETTED AREA          32.6277    VOLUME             13.9249
    VOLUME CENTROID       0.9301    UNITS ARE IN   M

                              MOLD LINE CONTOUR

    LONGITUDINAL STATIONS   0.0000    0.0468    0.0936    0.1871    0.2807
        0.3743     0.4193     0.4644     0.5095     0.5546     2.6270*

               Z-OFFSET    0.0000    0.0000    0.0000    0.0000    0.0000
        0.0000     0.0000     0.0000     0.0000     0.0000     0.0000*

             BODY RADII    0.0000    0.6611    0.9325    1.3122    1.5989
        1.8367     1.9018     1.9340     1.9507     1.9560     0.3142*
    NOTE - * INDICATES SLOPE DISCONTINUOUS POINTS
1       ***** THE USAF AUTOMATED MISSILE DATCOM * REV 03/11 *****  CASE   1
             AERODYNAMIC METHODS FOR MISSILE CONFIGURATIONS        PAGE   3
                               ApollotestComp
                     STATIC AERODYNAMICS FOR BODY ALONE

       ******* FLIGHT CONDITIONS AND REFERENCE QUANTITIES *******
     MACH NO  =      10.00              REYNOLDS NO = 1.701E+06 /M
     ALTITUDE =    35000.0 M         DYNAMIC PRESSURE =  40269.83 N/M**2
     SIDESLIP =       0.00 DEG                   ROLL =      0.00 DEG
     REF AREA =     12.000 M**2         MOMENT CENTER =     1.100 M
     REF LENGTH =     3.91 M           LAT REF LENGTH =      3.91 M

                   ----- LONGITUDINAL -----     -- LATERAL DIRECTIONAL --
         ALPHA       CN         CM         CA         CY        CLN        CLL

        -49.00    -0.474     0.038     0.773     0.000     0.000     0.000
        -48.00    -0.464     0.038     0.799     0.000     0.000     0.000
        -47.00    -0.454     0.037     0.825     0.000     0.000     0.000
        -46.00    -0.443     0.037     0.852     0.000     0.000     0.000
        -45.00    -0.433     0.036     0.878     0.000     0.000     0.000
        -44.00    -0.422     0.036     0.905     0.000     0.000     0.000
        -43.00    -0.411     0.035     0.932     0.000     0.000     0.000
        -42.00    -0.400     0.034     0.958     0.000     0.000     0.000
        -41.00    -0.389     0.033     0.984     0.000     0.000     0.000
        -40.00    -0.378     0.032     1.011     0.000     0.000     0.000
        -39.00    -0.367     0.031     1.037     0.000     0.000     0.000
        -38.00    -0.356     0.030     1.063     0.000     0.000     0.000
        -37.00    -0.344     0.028     1.088     0.000     0.000     0.000
        -36.00    -0.333     0.027     1.114     0.000     0.000     0.000
        -35.00    -0.321     0.026     1.139     0.000     0.000     0.000
        -34.00    -0.310     0.024     1.164     0.000     0.000     0.000
        -33.00    -0.298     0.022     1.188     0.000     0.000     0.000
        -32.00    -0.287     0.021     1.212     0.000     0.000     0.000
```

```
-31.00    -0.276     0.019     1.236     0.000     0.000     0.000
-30.00    -0.264     0.017     1.259     0.000     0.000     0.000
-29.00    -0.253     0.015     1.282     0.000     0.000     0.000
-28.00    -0.241     0.013     1.304     0.000     0.000     0.000
-27.00    -0.230     0.011     1.326     0.000     0.000     0.000
-26.00    -0.219     0.009     1.347     0.000     0.000     0.000
-25.00    -0.208     0.007     1.368     0.000     0.000     0.000
-24.00    -0.197     0.005     1.388     0.000     0.000     0.000
-23.00    -0.186     0.002     1.407     0.000     0.000     0.000
-22.00    -0.175     0.000     1.426     0.000     0.000     0.000
-21.00    -0.165    -0.002     1.444     0.000     0.000     0.000
-20.00    -0.154    -0.005     1.462     0.000     0.000     0.000
-19.00    -0.144    -0.007     1.478     0.000     0.000     0.000
-18.00    -0.134    -0.010     1.494     0.000     0.000     0.000
-17.00    -0.124    -0.012     1.509     0.000     0.000     0.000
-16.00    -0.115    -0.015     1.524     0.000     0.000     0.000
-15.00    -0.105    -0.017     1.538     0.000     0.000     0.000
-14.00    -0.096    -0.020     1.551     0.000     0.000     0.000
-13.00    -0.087    -0.023     1.563     0.000     0.000     0.000
-12.00    -0.079    -0.025     1.574     0.000     0.000     0.000
-11.00    -0.070    -0.028     1.584     0.000     0.000     0.000
-10.00    -0.062    -0.031     1.594     0.000     0.000     0.000
 -9.00    -0.055    -0.033     1.602     0.000     0.000     0.000
 -8.00    -0.048    -0.036     1.610     0.000     0.000     0.000
 -7.00    -0.041    -0.039     1.617     0.000     0.000     0.000
 -6.00    -0.034    -0.042     1.623     0.000     0.000     0.000
 -5.00    -0.028    -0.044     1.628     0.000     0.000     0.000
 -4.00    -0.022    -0.047     1.632     0.000     0.000     0.000
 -3.00    -0.015    -0.050     1.635     0.000     0.000     0.000
 -2.00    -0.010    -0.052     1.638     0.000     0.000     0.000
 -1.00    -0.005    -0.055     1.639     0.000     0.000     0.000
  0.00     0.000    -0.057     1.640     0.000     0.000     0.000

 ALPHA       CL        CD      CL/CD     X-C.P.

-49.00     0.272     0.864     0.315    -0.081
-48.00     0.283     0.879     0.322    -0.082
-47.00     0.294     0.895     0.329    -0.082
-46.00     0.305     0.911     0.335    -0.083
-45.00     0.315     0.927     0.340    -0.084
-44.00     0.325     0.944     0.344    -0.084
-43.00     0.334     0.962     0.348    -0.085
-42.00     0.343     0.980     0.350    -0.085
-41.00     0.352     0.998     0.352    -0.085
-40.00     0.360     1.017     0.354    -0.085
-39.00     0.367     1.037     0.354    -0.084
-38.00     0.374     1.056     0.354    -0.083
-37.00     0.380     1.076     0.353    -0.083
-36.00     0.385     1.097     0.351    -0.081
-35.00     0.390     1.117     0.349    -0.080
-34.00     0.394     1.138     0.346    -0.078
-33.00     0.397     1.159     0.342    -0.075
-32.00     0.399     1.180     0.338    -0.072
-31.00     0.400     1.201     0.333    -0.069
-30.00     0.401     1.222     0.328    -0.065
-29.00     0.400     1.244     0.322    -0.060
```

```
        -28.00     0.399     1.265     0.316    -0.055
        -27.00     0.397     1.286     0.309    -0.049
        -26.00     0.394     1.307     0.301    -0.042
        -25.00     0.390     1.327     0.294    -0.034
        -24.00     0.385     1.348     0.285    -0.024
        -23.00     0.379     1.368     0.277    -0.013
        -22.00     0.372     1.388     0.268    -0.001
        -21.00     0.364     1.407     0.259     0.014
        -20.00     0.355     1.426     0.249     0.030
        -19.00     0.345     1.445     0.239     0.049
        -18.00     0.334     1.463     0.229     0.072
        -17.00     0.323     1.480     0.218     0.098
        -16.00     0.310     1.497     0.207     0.129
        -15.00     0.296     1.513     0.196     0.165
        -14.00     0.282     1.528     0.184     0.208
        -13.00     0.266     1.542     0.173     0.259
        -12.00     0.250     1.556     0.161     0.321
        -11.00     0.233     1.569     0.149     0.398
        -10.00     0.215     1.580     0.136     0.492
         -9.00     0.197     1.591     0.124     0.611
         -8.00     0.177     1.601     0.111     0.760
         -7.00     0.157     1.610     0.097     0.955
         -6.00     0.136     1.618     0.084     1.218
         -5.00     0.114     1.624     0.070     1.591
         -4.00     0.092     1.630     0.057     2.178
         -3.00     0.070     1.634     0.043     3.240
         -2.00     0.048     1.637     0.029     5.462
         -1.00     0.024     1.639     0.015    11.987
          0.00     0.000     1.640     0.000    -0.591

   X-C.P. MEAS. FROM MOMENT CENTER IN REF. LENGTHS, NEG. AFT OF MOMENT CENTER
1        ***** THE USAF AUTOMATED MISSILE DATCOM * REV 03/11 *****    CASE   1
              AERODYNAMIC METHODS FOR MISSILE CONFIGURATIONS          PAGE   4
                               ApollotestComp
                     STATIC AERODYNAMICS FOR BODY ALONE

       ******* FLIGHT CONDITIONS AND REFERENCE QUANTITIES *******
     MACH NO  =      10.00                REYNOLDS NO = 1.701E+06 /M
     ALTITUDE =    35000.0 M         DYNAMIC PRESSURE =  40269.83 N/M**2
     SIDESLIP =       0.00 DEG                   ROLL =      0.00 DEG
     REF AREA =     12.000 M**2         MOMENT CENTER =     1.100 M
     REF LENGTH =     3.91 M           LAT REF LENGTH =      3.91 M

                   ---------- DERIVATIVES (PER DEGREE) ----------
         ALPHA       CNA         CMA         CYB         CLNB        CLLB
        -49.00      0.0099      0.0006
        -48.00      0.0101      0.0006
        -47.00      0.0103      0.0005
        -46.00      0.0104      0.0004
        -45.00      0.0106      0.0003
        -44.00      0.0107      0.0002
        -43.00      0.0109      0.0001
        -42.00      0.0110      0.0000
        -41.00      0.0111     -0.0001
        -40.00      0.0112     -0.0002
        -39.00      0.0113     -0.0003
```

```
          -38.00       0.0113     -0.0003
          -37.00       0.0114     -0.0004
          -36.00       0.0114     -0.0005
          -35.00       0.0115     -0.0006
          -34.00       0.0115     -0.0007
          -33.00       0.0115     -0.0008
          -32.00       0.0115     -0.0009
          -31.00       0.0115     -0.0010
          -30.00       0.0114     -0.0011
          -29.00       0.0114     -0.0012
          -28.00       0.0113     -0.0012
          -27.00       0.0112     -0.0013
          -26.00       0.0111     -0.0014
          -25.00       0.0110     -0.0015
          -24.00       0.0109     -0.0016
          -23.00       0.0108     -0.0016
          -22.00       0.0106     -0.0017
          -21.00       0.0105     -0.0018
          -20.00       0.0103     -0.0018
          -19.00       0.0101     -0.0019
          -18.00       0.0099     -0.0020
          -17.00       0.0097     -0.0020
          -16.00       0.0095     -0.0021
          -15.00       0.0092     -0.0022
          -14.00       0.0090     -0.0022
          -13.00       0.0087     -0.0023
          -12.00       0.0085     -0.0023
          -11.00       0.0082     -0.0023
          -10.00       0.0079     -0.0024
           -9.00       0.0074     -0.0024
           -8.00       0.0070     -0.0025
           -7.00       0.0067     -0.0025
           -6.00       0.0064     -0.0025
           -5.00       0.0063     -0.0025
           -4.00       0.0063     -0.0025
           -3.00       0.0060     -0.0026
           -2.00       0.0054     -0.0026
           -1.00       0.0048     -0.0026
            0.00       0.0044     -0.0026

     BODY ALONE LINEAR DATA GENERATED FROM SECOND ORDER SHOCK EXPANSION METHOD

      *** END OF JOB ***
```

B

Upper Stage DATCOM for005.dat File

```
CASEID 2ndStageEntry
DIM M
DERIV DEG
$REFQ
XCG=3.9,
SREF=10.52,
LREF=10.7092,
LATREF=3.66,
RHR=400.0,
$END
$FLTCON
NALPHA=50.,
ALPHA=0.,1.,2.,3.,4.,5.,6.,7.,8.,9.,
ALPHA(11)=10.,11.,12.,13.,14.,15.,16.,17.,18.,19.,
ALPHA(21)=20.,21.,22.,23.,24.,25.,26.,27.,28.,29.,
ALPHA(31)=30.,31.,32.,33.,34.,35.,36.,37.,38.,39.,
ALPHA(41)=40.,41.,42.,43.,44.,45.,46.,47.,48.,49.,
BETA=0.,
NMACH=20.0,
MACH=0.8,0.9,1.0,1.1,1.2,1.3,1.5,2.,
MACH(9)=3.,4.,5.,6.,7.,8.,9.,10.,11.,12.,13.,14.,
ALT=10000.,10000.,10000.,10000.,10000.,10000.,
ALT(7)=10000.,10000.,10000.,10000.,10000.,
ALT(12)=10000.,10000.,10000.,10000.,10000.,
ALT(17)=10000.,10000.,10000.,10000.,
$END
$AXIBOD
NX=11.0,
X=0.0,0.0417204,0.0834407,0.166881,0.250322,0.333763,
X(7)=0.376262,0.418761,0.46126,0.503759,5.54,
R=0.0,0.616442,0.869782,1.22438,1.49258,1.71538,1.77842,
R(8)=1.80911,1.82501,1.83,1.83,
$END
SOSE
NO LAT
PLOT
PRINT GEOM BODY
SAVE

NEXT CASE
```

```
$FLTCON
NMACH=16.0,
MACH=15.,16.,17.,18.,19.,20.,21.,22.,23.,24.,25.
MACH(12)=26.,27.,28.,29.,30.,
ALT=10000.,10000.,10000.,10000.,10000.,10000.,
ALT(7)=10000.,10000.,10000.,10000.,10000.,
ALT(12)=10000.,10000.,10000.,10000.,10000.,
$END
SAVE

NEXT CASE
$FLTCON
NMACH=20.0,
MACH=0.8,0.9,1.0,1.1,1.2,1.3,1.5,2.,
MACH(9)=3.,4.,5.,6.,7.,8.,9.,10.,11.,12.,13.,14.,
ALT=15000.,15000.,15000.,15000.,15000.,15000.,
ALT(7)=15000.,15000.,15000.,15000.,15000.,
ALT(12)=15000.,15000.,15000.,15000.,15000.,
ALT(17)=15000.,15000.,15000.,15000.,
$END
SAVE

NEXT CASE
$FLTCON
NMACH=16.0,
MACH=15.,16.,17.,18.,19.,20.,21.,22.,23.,24.,25.
MACH(12)=26.,27.,28.,29.,30.,
ALT=15000.,15000.,15000.,15000.,15000.,15000.,
ALT(7)=15000.,15000.,15000.,15000.,15000.,
ALT(12)=15000.,15000.,15000.,15000.,15000.,
$END
SAVE

NEXT CASE
$FLTCON
NMACH=20.0,
MACH=0.8,0.9,1.0,1.1,1.2,1.3,1.5,2.,
MACH(9)=3.,4.,5.,6.,7.,8.,9.,10.,11.,12.,13.,14.,
ALT=20000.,20000.,20000.,20000.,20000.,20000.,
ALT(7)=20000.,20000.,20000.,20000.,20000.,
ALT(12)=20000.,20000.,20000.,20000.,20000.,
ALT(17)=20000.,20000.,20000.,20000.,
$END
SAVE
```

...and so on until 120 km altitude.

Aerodynamic forces are assumed negligible at higher altitudes.

C

Heat Shield Radius Effect on C_M

One aspect that significantly influences the aerodynamic moment coefficients of ballistic reentry vehicle such as the Apollo CM or the reusable upper stage is the shape of the heat shield. This comes as no surprise, since the heat shield is the main or even only surface facing the airflow. The Apollo CM and the Soyuz descent module both use hemispherical heat shields as opposed to the more stable blunted cone to make it easier to trim the vehicle at a non-zero angle of attack Button et al. (2009). However, it also makes the task more difficult to introduce a passive trim attitude for a given shift in the center of mass due to the strong stable moments.

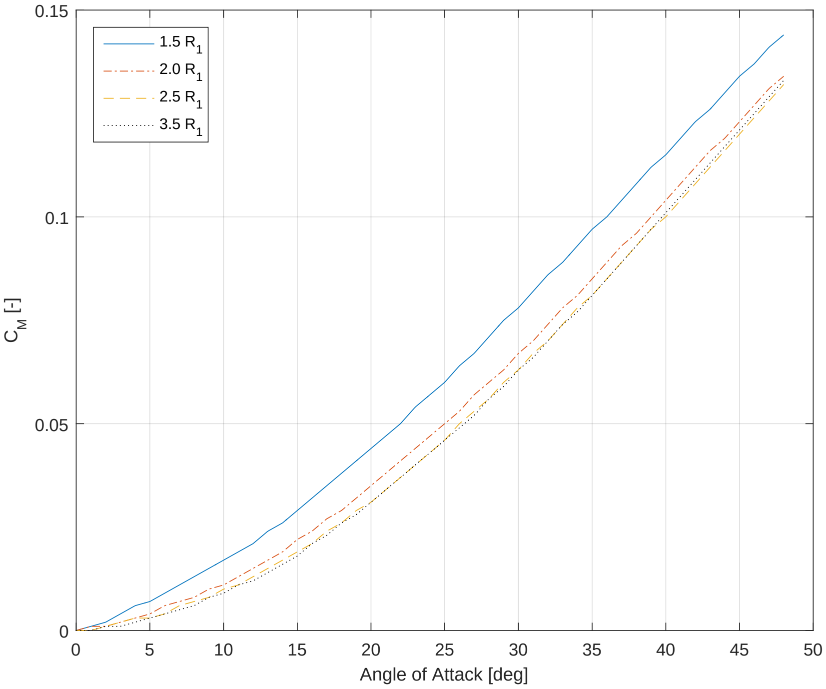

Figure C.1: Rendition of the Falcon 9 second stage after engine cutoff still attached to the payload.

A hemispherical heat shield is also used for the upper stage. To determine the effect of the radius of the hemispherical heat shield on the moment coefficient several radii are implemented for the upper stage in Missile DATCOM and plotted in Figure C.1 as a function of angle of attack.

A radius of 1.5, 2, 2.5, and 3.5 times the upper stage cylindrical radius is used to construct the heat shield shapes. The plot shows a trend towards increased stability with increased main heat shield radius. The curves show that the rounder the heat shield surface at the front of the upper stage the more unstable it becomes.

The rounded surface deflects more of the airflow towards the same side as the upper stage side wall, which adds to the instability just like the side walls do. A more flat frontal surface on the other hand deflects more of the flow towards the opposite direction at an angle of attack thereby stabilizing the vehicle. Hence to improve the stability of the upper stage the heat shield is made relatively flat without going into excess to not introduce sharp edges around the circumference and therefore possible hot spots Dirkx (2011).